INPUT-SHAPED MODEL REFERENCE CONTROL FOR FLEXIBLE SYSTEMS

A Dissertation
Presented to
The Academic Faculty

By

Daichi D. Fujioka

In Partial Fulfillment
of the Requirements for the Degree
Doctor of Philosophy in the
School of The George W. Woodruff School of Mechanical Engineering

Georgia Institute of Technology

August 2017

Copyright © Daichi D. Fujioka 2017

INPUT-SHAPED MODEL REFERENCE CONTROL FOR FLEXIBLE SYSTEMS

Approved by:

Dr. William Singhose, Advisor
School of Mechanical Engineering
Georgia Institute of Technology

Dr. Charles Ume
School of Mechanical Engineering
Georgia Institute of Technology

Dr. Jun Ueda
School of Mechanical Engineering
Georgia Institute of Technology

Dr. Joshua Vaughan
Department of Mechanical Engineering
University of Louisiana at Lafayette

Dr. Jonathan Rogers
School of Mechanical Engineering
Georgia Institute of Technology

Date Approved: June 01, 2016

Learning is the most luxurious hobby in the world.

- Daichi D. Fujioka

To my loving family,

who always had supported me,

during my most difficult times.

ACKNOWLEDGEMENTS

First, I want to thank my family for their continuous support and love during my study.

My special thanks goes to Dr. Ume, Dr. Ueda, Dr. Vaughan, and Dr. Rogers for being on my committee and providing assistance and insights for this research.

I also like to say thank you to all students who contributed in my work by collecting experimental data.

Lastly, I thank Dr. Singhose for being my advisor. This work would not have been possible without his noble academic guidance.

TABLE OF CONTENTS

LIST OF TABLES

LIST OF FIGURES

SUMMARY

Heavy-lifting machines, such as cranes and aerial lifts, are widely used to perform material handling in various applications. However, their operational efficiency and throughput are degraded by the inherent flexible dynamics of the systems. For example, cranes carrying a payload can experience large payload swings, and aerial lifts extending or rotating their arms can vibrate due to the flexibility in the arms and the joints. The oscillation problems are further complicated by complex nonlinear dynamics, time-varying parameters, and lack of full state information.

This thesis investigates a simple and robust control method that improves the operation of flexible systems, even in the absence of an accurate system model and sensing. The goal is achieved via the combination of input shaping and model reference control (MRC). The input-shaped model reference control (IS-MRC) design compensates for the weakness of input shaping with the MRC scheme, while input shaping improves the performance of MRC by modifying the reference command. The benefits of the proposed controller design include increased robustness against plant uncertainties and parameter estimation errors, while also achieving good vibration suppression and control effort reduction.

The IS-MRC design is first developed for controlling a crane with a single-pendulum payload. The state space representation and parameter values of the reference model and plant are developed. A Lyapunov control law with asymptotic stability and the corresponding input shaper design are derived. Numerical simulations reveal that IS-MRC contributes to reducing the control effort magnitude for large ranges of system parameter values. The robustness of IS-MRC to parameter estimation errors is analyzed. The performance of IS-MRC in state tracking, oscillation suppression, and control effort reduction is verified via experiments.

The IS-MRC design is further tested on a nonlinear double-pendulum payload. The double-pendulum dynamics are derived and the state space representation of the plant is

obtained. The possible ranges of oscillation modes are calculated, and multi-mode input shapers are designed to suppress the range oscillations. To address practical implementation issues, a linear single-pendulum is used as the reference model. A Lyapunov control law using only the first mode states of the plant is derived. The robustness of various IS-MRC designs are tested via numerical simulations and experiments. The robustness to the plant modeling error is analyzed by inducing error in the estimated plant natural frequency. The robust IS-MRC effectively suppresses the hook and payload oscillations. The trade-off to effective suppression, however, is a slower motion.

The thesis then extends the study to improve the performance of IS-MRC. An optimized input-shaped model reference control (OIS-MRC) scheme is developed to obtain the optimal combination of input shaping and model reference control. An optimization technique is used to concurrently design the controller parameters that realize the shortest time duration, while satisfying a set of design constraints. The controller performance is tested on a more complex plant; an uncertain, time-varying double-pendulum crane. The OIS-MRC demonstrates superior performances in all evaluated criteria, while maintaining the same level of large robustness as the initial IS-MRC design.

The effectiveness of OIS-MRC is also validated by conducting human operator testing. In the testing, the subjects drive a small-scale bridge crane and navigate a payload through an obstacle course. The course is designed to examine the proposed controller's handling of the parameter variations and rejection of external disturbances. In each trial, the course completion time and number of collisions with obstacles were recorded. Furthermore, the test subjects rated the controller's ease of use. The outcomes were analyzed and they validated the predicted improvements of OIS-MRC performance compared to the non-optimized IS-MRC design.

The findings in this thesis provide a significant tool for controlling complex machine systems with uncertain flexible dynamics. The proposed IS-MRC scheme is practical and compatible with physical machine applications as the theory can be easily extended to

different mechanical systems. The experimental results and operator testing data provide confidence for the study's accuracy and practicality.

CHAPTER 1
INTRODUCTION

1.1 Research Objectives and Methods

Heavy-lifting machines, such as cranes and aerial lifts, are commonly employed in material-handling and transporting applications. These machines have been used widely for logistics, manufacturing, general construction, and more. However, their performance and operation efficiency is degraded by the inherent flexible dynamics of the systems, such as payload swing and machine vibration. The complex nonlinear dynamics of the machines pose a great control challenge. The problem is further complicated when accurate representations of the systems and full system state measurements are not available. Poorly controlled flexible systems pose a great safety hazard to the surroundings and humans workers. In fact, the chances of accidents in such transporting machines can be increased by unintended flexible motion [1, 2, 3, 4, 5, 6, 7].

The objective of this thesis is to develop a simple and robust control method for operating such flexible systems in the absence of an accurate system model and sensing. In order to achieve this goal, a control method that combines input shaping and model reference control (MRC) is proposed. An input-shaped model reference control (IS-MRC) scheme is developed by implementing an input shaper in conjunction with a MRC algorithm in series. The controller is designed to improve the overall controller robustness to modeling error and uncertainty, while achieving good vibration suppression and control effort reduction. The proposed controller design is tested on planar cranes with a single- and double-pendulum payload in this work.

To investigate the IS-MRC design and its effectiveness, the research work is broken down into the following subtasks:

- Develop IS-MRC design
  - Develop LTI and nonlinear dynamics models of the single- and double-pendulum payloads
  - Derive control laws that guarantee stability
  - Design an input shaper for eliminating unwanted system oscillations
- Develop a method for constructing the optimized IS-MRC controller with design constraints
  - Obtain a realistic and appropriate cost function to optimize
  - Derive analytical expressions for the controller design constraints
- Create an experimental bridge crane test facility
  - Implement the IS-MRC control for a 2D workspace
  - Construct an evaluation course that tests human operator performance in the presence of uncertainty and disturbances
- Evaluate the performance of the proposed IS-MRC methods
  - Validate the performance of IS-MRC controller in state tracking, oscillation suppression, and control effort reduction
  - Analyze the controller robustness to parameter estimation errors, unmodeled system nonlinearities, neglected higher-order states, and varying plant parameters
  - Verify key theoretical predictions and phenomena of IS-MRC method using both nonlinear simulations and experimental tests
  - Conduct human operator studies on operational efficiency of cranes and perform statistical analysis on the data

1.2 Related Fields and Past Research

There had been several works successfully accomplishing reduced-swing control of cranes. Feedback control is a very popular control method that has been applied in various engineering applications. Conventional PD and PID controllers are used extensively in industry because of their simple implementation and effectiveness when the system operates near the linearized equilibrium point [8]. However, Souissi and Koivo proposed a two-tier controller for rotary cranes and proved that the PD controller was not highly effective at reducing payload oscillation [9].

Numerous researches have attempted to more effectively limit the crane payload oscillation by utilizing adaptive control [10, 11, 12, 13, 14], sliding mode [15, 16, 17, 18, 19, 20, 21], optimal control [22, 23, 24], energy-based control [25, 26], saturation-based control scheme [27, 28], fuzzy control [17, 29, 30, 31, 32, 33], and gain scheduling [34, 35]. Fang et al. developed energy-based control laws that increases the coupling between pendulum and gantry position in order to improve the transient response [36]. Park et al. designed anti-sway adaptive fuzzy sliding-mode trajectory tracking controller designed for 2-DOF cranes [37]. A controller that combined a feedforward control with a nonlinear PID based on a Lyapunov stability theorem achieved sufficient damping in payload swing by adapting the desired trolley trajectory [38]. Optimal control of a crane using a minimum transfer time was suggested by Auernig and Troger using Pontryagin maximum principle [39] and by Terashima et al. using an open-loop straight transfer transformation model with the Davidon-Fletcher-Powell numerical method [40]. Valera et al. proposed the combination of two neural networks, one for learning the nonlinear system behavior and another for calculating the control action, to achieve trajectory tracking and payload sway reduction [41].

Another well established control methodology for under-actuated mechanical systems is energy shaping. The control method achieves stabilization by shaping the potential en-

ergy [42, 43] or total energy (including the kinetic energy) [44] function of the system, while preserving its structure. The two main approaches of the method are controlled Lagrangian [45] and interconnection and damping assignment passivity based control (IDA-PBC) [46]. Ning et al. developed the energy shaping based output feedback control law using concept of virtual payloads [47].

Mehra et al. developed the nonlinear state feedback control law using potential energy shaping that obviates the need for solving the matching conditions [48]. This is advantageous because the conditions are usually defined in partial differential equations and can be very difficult to solve, especially with complex system dynamics. The robustness of the method is demonstrated with various model uncertainties such as initial swing angle, varying system parameters, rail friction, and input saturation. Although the proposed controller improved the time for swing elimination, the transient swing angles were found to be larger than other existing controllers, such as a nonlinear tracking controller [49] and an energy coupling-based output feedback controller [47].

1.2.1 Limitation of Feedback Control

To realize highly effective performance, a feedback controller generally demands accurate knowledge of the states of the payload. Although there has been success, there are several limitations that make implementation of feedback control difficult on actual cranes. One of the challenges is the hard nonlinearity of the cranes. Feedback control often assumes an ideal plant when designing the controller. However, actual cranes exhibit complex nonlinear system dynamics due to hard nonlinearities. Common hard nonlinear elements include rail friction [11, 50, 51], actuator saturation [27, 28, 47, 52], acceleration rate limiting [53, 54], dead-zone [55], backlash [56, 57], Coulomb friction [58], and coupling between the trolley and payload [47] have been studied extensively and described in detail.

Another drawback of feedback control is that there always exists errors in the measurements of the payload motion. Obtaining accurate measurements is difficult and costly to

achieve because of the physical limitations in the sensors. One of the methods that have been used with some success is machine vision. Machine vision systems utilize image sensors that work sufficiently well in fairly controlled environments where lighting conditions are consistent and background clutter is minimal [59, 60, 61, 62]. However, many cranes operate in more random and erratic environment, such as ports and construction sites. Even with an ideal environment, sensing the payload is not trivial. One common place to mount an image sensor/camera is overhead attached to the trolley. This configuration allows the hook to remain in the camera's field-of-view under most circumstances. However, the suspension cable and hook could block the camera's view and prevent it from obtaining accurate images of the payload.

Another sensing method promising some success is the use of inertial measurement units (IMU) containing accelerometers and gyroscopes [63, 64, 45, 65]. In [66], state measurements were obtained using two gyroscopes. The gyroscopic measurements are often coupled with observers that are used to smooth the resulting signals. The implementation of such observers introduces an additional complexity to the problem. Another common issue mainly in gyroscopes is a drift in time [67, 68]. For a standard crane application, this drawback could be reduced with a frequent time-basis calibration of the gyroscope.

Another issue in the feedback loop control is a time-delay. Actuators and sensors that are involved in feedback loop usually introduce such delays. Time-delay systems are also common in real processes and are challenging applications for many classical controllers. Thus, the presence of the delay phenomenon in the system and the controller can be potentially disastrous in terms of stability and oscillations [69].

Other modeling uncertainties and system parameter variations pose additional challenges to the control problem. In certain applications, cranes could operate under a wide range of loading characteristics and substantially varying system parameters such as the payload weights and cable lengths. Such operating conditions are common for industrial cranes [49]. Attaching a more complex payload, such as double-pendulum, also poses a

control challenge. In addition, external factors such as wind disturbances and poor sensing further complicates the problem. Taking those factors into consideration is important in the controller design. Otherwise, the controller could result in a degraded performance and/or produce an unstable response. For example, Omar and Neyfeh applied two full state feedback controllers in an attemp to reduce payload oscillation in a tower crane [70]. The controller effectiveness, however, decreased with changes in the system parameters because the feedback gains were explicitly designed only for the given parameter values.

1.2.2 Model Reference Control

A control method that is useful for handling an uncertain system is model reference control (MRC). MRC generates a control signal such that the plant states asymptotically track the states of a desirable reference model. When the reference model is linear, this approach modifies the plant behavior by attempting to artificially linearizing its system dynamics. MRC addresses a control problem by specifying the performance requirements in terms of a reference model and its desired response. These features of MRC make it an useful tool when designing a controller for highly complex systems that are time-varying [71, 72, 73], nonlinear [74, 75], or both [76]. The control method also has advantages in dealing with disturbances, uncertainties, and unmodeled dynamics. MRC had been implemented in various engineering applications, such as control of robots [77] and mechanical oscillators [78].

Many MRC controller designs have been studied by previous researchers. Ucar utilized MRC to solve the problem of controlling chaotic systems [79]. Zhao et al. successfully applied a MRC based on the Lyapunov stability theorem to control a hyper-chaotic system with both certain and uncertain parameters [80]. Also, using Lyapunov stability, Hongjie and Yuqiao developed a MRC scheme with the Cerebellar Model Articulation Controller neural network algorithm [81]. Basher investigated a linear MRC combined with a nonlinear control law on an uncertain plant with time-delayed inputs. Under certain assumptions

on the matrix functions and the controlling system, the controller was made insensitive to system parameter variations and guaranteed that all solutions are uniformly ultimately bounded [82, 83]. Santosh and Chidambaram designed a MRC scheme for an unstable second-order system with time-delay. The controller was robust to uncertainties in the model parameters such as time-delay, time constant, or process gain [84]. Belikov and Petlenkov proposed a feedback linearization algorithm for MRC of nonlinear MIMO systems identified by an Additive Nonlinear Autoregressive eXogenous (ANARX) model. A neural network with a specific restricted connectivity structure was utilized to construct the ANARX models. They demonstrated the effectiveness of the proposed controller in linearizing the ANARX or NN-based ANARX models via numerical simulations [85, 86].

MRC scheme had proven to be effective in many control problems; however, there are some difficulties associated with using it. The performance of MRC depends on the formulation of a reference model that properly represents the controlled plant [87, 88, 75]. In many cases, MRC techniques assume that a suitable reference model is always available for controller design. This assumption is not always realistic as actual systems can be difficult to model given nonlinearities and uncertainties. When an accurate reference model is not available, and the error becomes too large for MRC to handle, MRC degrades the state tracking performance and fails to supply sufficient controller force to dictate the system dynamics. This usually causes poor control performance and leads to exceeding the maximum control effort, thereby resulting actuator saturation/failure.

Another shortcoming of MRC is that certain combinations of performance objectives and a priori uncertainty lead to unsolvable MRC design problems, while other combinations lead to problems that can be solved only by careful choice of the reference model [89]. In addition, the lack of a systematic methodology for constructing the appropriate control law further complicates the controller design process.

This issue was considered in previous research by analyzing and increasing the robustness of MRC [90]. Sun et al. enhanced the system stability and robustness via a MRC

controller composed of a conventional model matching feedback and a linear model error compensator [91]. Pedret et al. developed a robust MRC structure based on a right coprime factorization of the plant along with an observer-based feedback control scheme combined with a prefilter controller [92]. He and Zhang developed a MRC algorithm that uses a support vector machine as a regression tool to learn the feed-forward controller from input and output data [93]. While the robustness of MRC for the state tracking performance has been studied extensively, much less emphasis has been placed on the issue of control effort saturation. Only a handful of feedback controllers considered a practical approach to input saturation [27, 28, 47].

1.2.3 Input Shaping

To decrease the system vibration, an intelligent reference signal generation technique called *input shaping* can be utilized to provide a simple and effective solution. Input shaping strategically modifies a command by convolving it with a sequence of impulses called an *input shaper*. The resulting shaped command induces very small residual vibration [94]. The concept was first introduced by Otto Smith as the Posicast controller, where a step input is broken into multiple steps, so as to eliminate residual vibrations of an under-damped system [95, 96]. However, Posicast control was sensitive to errors in model parameters such as the natural frequency and damping ratio.

Several techniques were proposed to design an input shaper that is robust to errors in the system parameters and minimizes the residual vibrations [97, 98, 99, 100, 101, 102]. A huge advantage of this technique is that it can function without any real-time measurements or estimated state feedback. The only information required to design an input shaper are the values of the natural frequencies and damping ratios of the undesired vibratory modes.

Input shaping has shown to effectively reduce system vibrations in several flexible machine applications, including gantry or bridge cranes [103, 104, 105, 106, 107], tower cranes [108, 109, 110], boom cranes [111, 112], robotic arms [113, 114, 115, 116, 117,

118, 119], spacecraft [120, 97, 121, 122, 123, 124, 125, 126], helicopters [127, 128], micro-milling machines [129], disk-drive manufacturing machines [130], silicone handling robots [131], magnetic tape data readers [132], microelectromechanical systems [133], telescopic handler [101], and coordinate measuring machines [134, 135]. Input shaping has been shown to reduce system vibration and improve the performance of time-delay systems with flexibility [136, 137]. Lawrence et al. considered input shaping from the perspective of backlash [57] and coulomb friction [58]. Danielson et al. extended the work by Lawrence to analyze rate limiting for a limited number of input shapers [54]. In addition, many human operator studies have shown that input shaping can greatly improve overall system performance [103, 106, 137].

However, input shaping also possesses some disadvantages. One of the primary weaknesses is that input shaping cannot effectively reject vibrations from external disturbances because it does not have any feedback loop in the control architecture. Another disadvantage is that a small time-delay occurs in the input command because of the convolution method used to obtain the shaped command. In addition, the effectiveness of input shaping can be degraded when the undesired vibratory mode is poorly estimated. This makes input shaping alone insufficient for effective and robust control of nonlinear cranes with uncertainties and disturbances.

The approach of combining input shaping and a feedback controller such as linear state feedback [138, 139], robust control [140, 141], and flexible system dynamics for the optimal performance [142] have been investigated. Kenison and Singhose developed an optimization routine to concurrently design an input shaper and PD feedback control parameters for a double integrator [143]. They considered various metrics such as percent overshoot, residual energy, and settling time in the optimization process. Similarly, Gopalakrishnan et al. studied the design of input shaping plus PD control for several second-order systems [144]. Banerjee et al. used a non-linear optimization routine to design both an input shaper and PID feedback controller for a flexible spacecraft [145]. Ottander and

Johnson combined input shaping with delayed feedback control of the payload swing angle to more accurately track a desired trajectory [62]. Bisgaard et al. used a state estimator to measure the natural frequency of the suspended load oscillation and adaptively updated an input shaper to prevent oscillation at the measured natural frequency [61].

In addition, input shaping can mitigate the weaknesses of general feedback control methods mentioned in the previous section. Input shaping can reduce the actuator nonlinearities by smoothing the command signal such that the signal is more easily followed by the actuator. Limiting the payload oscillation also helps to improve the state measurement accuracy because it facilitates the sensors to track the payload motion.

1.2.4 Input-Shaped Model Reference Control

MRC and input shaping can provide a good solution for the challenging problem of reducing vibration of nonlinear and/or uncertain systems. However, their weaknesses must be addressed because they could lead to degraded control performance. To supplement the shortcomings of input shaping and MRC, and to enhance the overall controller performance, a controller scheme combining input shaping and MRC is proposed. An input-shaped model reference control (IS-MRC) is developed by combining an input shaper with MRC algorithm in series. This structure has been previously studied by other researchers [146, 147, 148]. The controller has been used to improve the overall controller robustness to modeling error and uncertainty. The method has shown to be effective in reducing the residual vibrations and mitigating the effects of plant nonlinearities.

Yuan and Chang investigated the application of IS-MRC on a robotic manipulator [149] and a high-speed robot apparatus [150]. They presented the scheme of combining a type of input shaper, called a *Zero-Vibration* (ZV) shaper, with a MRC to reduce residual vibrations. The shaper design was based on a reference model with K_p gain feedback loop. The value of the gain was calculated to guarantee the controller stability. They derived an expression for the residual vibration, the envelope of the residual vibration, and the

conditions under which the residual vibration approaches zero. The robustness analysis of the controller via experiments justified the improved robustness of input shaping. The proposed IS-MRC effectively handled wide plant parameter variations, while eliminating residual vibrations. The work, however, was limited to only a plant with a simple transfer function. Chang et al. also applied the IS-MRC control scheme on a NEAT robot system with the presence of a dead-zone [151]. The velocity dead-zone was approximated as a nonlinear "soft" spring as part of the reference model. The uncertain plant was modeled with variable boundaries that cause unacceptable transient response or steady-state errors with conventional controllers.

Chatlatanagulchai and Kaveesoontornsanoh developed a feedback controller using an iterative learning control such that the closed-loop system was matched to the reference model [152]. The ZV shaper was then designed for the reference model vibration. However, the proposed control method was applicable only to systems with a repeated reference signal. Chatlatanagulchai et al. also combined a ZV shaper and MRC controller based on the quantitative feedback theory (QFT) [153]. The work, however, did not explore utilizing robust input shapers. The QFT based controller could be too conservative when all the possible plant uncertainties were covered solely by the MRC. The performance could be improved further when input shaping assumes a robust form and contributes to the overall controller robustness.

Yu and Chang compared the performance of IS-MRC on a two-mode system against a PI control and a traditional ZV shaper for two modes (ZV2M). The rise time and the response error were calculated for comparison. The proposed IS-MRC outperformed two other controller choices. Also, the proposed controller was shown to reduce the hysteresis effect [154]. Yu and Chang also applied the IS-MRC on a dual solenoid actuator. A balance control strategy unique to the solenoid system was developed, and the control scheme with an adjustable reference model via the K gain was presented. The controller accomplished a high precision positioning with reduced vibration motion [155].

Pai developed an IS-MRC using a sliding mode control law. The controller design utilized the sliding mode output feedback control (SMOFC) [99] and discrete-time neuro-sliding mode output feedback control (NSMOFC) [100]. This structure drove the plant to the desired states with characteristics of guaranteed stability and a chattering-free control signal. A major benefit of SMOFC is that the controller can be implemented even when full information on the states are not available, thus it is more compatible/easy to implement on real-world applications. The work, however, only considered the case where the physical plant and the reference model have linear, modal forms. This assumption was necessary for the error dynamics to satisfy the matching condition.

1.3 Thesis Contributions

This thesis advances knowledge in the field of system controls, in general, and the area of input shaping with feedback controller, in particular. A novelty in the proposed IS-MRC controller is an outstanding synergy between input shaping and MRC. Input shaping is well-integrated with MRC because its vibration reduction becomes highly effective because the MRC drives the plant states toward the dynamics of the reference model. Therefore, it drives the plant toward the dynamics that are used to design the input shaper. MRC also supplements the weakness of input shaping by providing state feedback that reject external disturbances.

Likewise, input shaping also compensates for the major drawback of MRC: a large control effort overshoot in the presence of large plant variation and/or nonlinearity. Because MRC attempts to force the plant behavior to track that of the reference model, its control effort can magnify significantly and exceed the allowable actuator limit. Input shaping can prevent control effort magnification by 1) filtering the command to make it more smooth, and 2) reducing the system vibration so its complex dynamic behavior is near the equilibrium point. Hence, it limits the influence of nonlinearities. In [156, 157], Dong et al. illustrated that input shaping can effectively reduce the maximum controller effort. A simi-

lar benefit can be expected when implemented in conjunction with MRC [158]. Combining these two simple control methods can enhance the overall controller performance and offer an effective solution to challenging control problems.

Although past studies demonstrated the controller application, their analysis on the controller's design and performance were often limited to the stability of the controller and verification of the design requirements. In many cases, the controller stability was guaranteed only for certain conditions or range of gain values. The asymptotic stability, if achieved, was proved but only through a highly complex process. In this thesis, a novel control law based on a Lyapunov method is obtained through a simpler derivation process, while assuring asymptotic stability of the controller base.

This research also extends the knowledge by focusing on how input shaping compliments MRC. To be specific, the work examines the control effort magnitudes as a function of modeling errors. Previous research made almost no detailed discussions on the control effort, except that it had either a "reasonable" magnitude or bounded within a certain level. The control effort overshoot in MRC at the presence of high system variation/uncertainty is a critical issue. Input shaping can help prevent this problem by smoothing the command and reducing the overshoot magnitude. However, detailed analysis on this effect has not been previously presented.

Many of the previous works also assumed that a suitable representation of the actual plant was available for the controller and thus only implemented the simplest form of an input shaper. This assumption is inappropriate for challenging control problems involving nonlinear systems that are difficult to model. The control problem is further complicated when the system parameters are uncertain and/or the full system states are not available via sensors. In the absence of accurate plant knowledge, MRC not only suffers from increased state tracking error, but also excessively large control effort [159, 160, 161].

Previous IS-MRC controllers were usually designed by obtaining the input shaper and MRC architecture separately. For example, when developing an IS-MRC for a variable

plant, the controller was obtained by combining a robust input shaper and a MRC with a reasonably damped reference model. This, however, could create an over-conservative controller because the controller robustness is realized by both the input shaper and MRC. Hence, this could lead to a IS-MRC design that functions far from the optimized performance. Some past works attempted to improve the combination of input shaper and MRC by manually adjusting poles in the varying reference model by a parameter K [155] and tweaking K_p and K_i gains in the feedback loop [154]. However, the shaper design remained unchanged in these works. Also, they only considered a few aspects of performance, such as settling time, to discuss the optimal functionality. This raises a question whether the resultant IS-MRC is truly optimal.

To fully understand and exploit this promising control architecture, further investigation of IS-MRC robustness is required. Many IS-MRC architectures demonstrated they were robust against plant variations. However, other factors such as the modeling errors and plant nonlinearities were also known to influence the IS-MRC performance. Their correlation to the performance, such as state tracking and vibration reduction, needs to be studied to validate the robustness of IS-MRC design. Finally, a more thorough understanding of IS-MRC and its utility for cranes can be gained by conducting experiments and human operator studies.

In summary, significant contributions of this thesis include the following:

- The simulation model of IS-MRC to control a nonlinear single-pendulum payload
- The simulation model of IS-MRC with linear single-pendulum reference model to control a nonlinear LTV double-pendulum payload
- Development of the optimized IS-MRC controller design
- Evaluation of the robustness of various IS-MRC control methods in terms of state tracking, oscillation reduction, and control effort reduction
- Implementation of IS-MRC control on a small-scale bridge crane for 2D workspace

- Human operator testing of the IS-MRC controller for validating the controller effectiveness
- Experimental verification of key IS-MRC attributes

1.4 Dissertation Overview

In Chapter 2, background information of the mechanical systems considered in this thesis is presented. These systems include cranes with a single- and double-pendulum payload. Then, Chapter 3 reviews traditional input shaping techniques. Chapter 4 introduces the MRC control scheme. The controller design and the derivation of Lyapunov control law are explained. Chapter 5 presents the proposed IS-MRC design. The process of designing the controller is presented. This chapter also examines the performance of IS-MRC controller on a single-pendulum payload. In Chapter 6, the work is extended to the double-pendulum payload with larger modeling uncertainty. The IS-MRC design and the control law is adapted to control a higher-order system with incomplete state feedback.

Chapter 7 explains the derivation procedure of the optimized IS-MRC controller design. The analytical expressions of the design constraints are presented. The chapter also evaluates the performance of the optimized IS-MRC against traditional IS-MRC designs. Chapter 8 verifies disturbance rejection of the proposed IS-MRC designs. Different types of disturbances are inflicted on various IS-MRC designs and the rejecting performances are compared. In Chapter 9, human operator testing is conducted on a obstacle course that simulates practical crane tasks and workspace environment. The statistical analysis of the data validates a significant performance improvement of the proposed control method. Chapter 10 contains concluding remarks from the analysis performed, and suggests some possible future works in this area.

CHAPTER 2
OVERHEAD BRIDGE CRANES

CHAPTER SUMMARY:

This chapter provides background information necessary to properly understand the mechanical systems used as test vehicles throughout this thesis. In Section 2.1, the dynamics of a crane with a single-pendulum payload are discussed. Section 2.2 presents the system dynamics of a double-pendulum payload. The nonlinear equations of motion and state space representations of the systems are thoroughly explained.

Cranes are widely utilized for various heavy-object transportation applications at construction sites, warehouses, shipyards, factories, and nuclear plants. However, the flexible suspension cables can induce large payload swing when subjected to motion of the overhead trolley. The inherent flexibility in crane dynamics is problematic for the crane's productivity. Furthermore, safety is degraded when a suspended load exhibits excessive payload swing that can result in obstacle collisions.

Flexible dynamics can be problematic for cranes because the induced oscillatory system response makes fast transfer and accurate positioning of the payload difficult. In cases where the swing amplitude becomes large, a severe time-delay may occur as the operator needs to wait until the swing amplitude settles to a low level before depositing the load. Furthermore, swinging payloads are difficult to move through cluttered work environments and they apply time-varying loads to the crane structure. These can result in serious damage to the load and crane, or safety hazards to the people within the workspace.

The payload dynamics possess nonlinearities that complicate the process when large swing angles arise. Nonlinearities also originate from the rotational swing motion of the payload in the form of centripetal and Coriolis accelerations. In addition to the pendulum

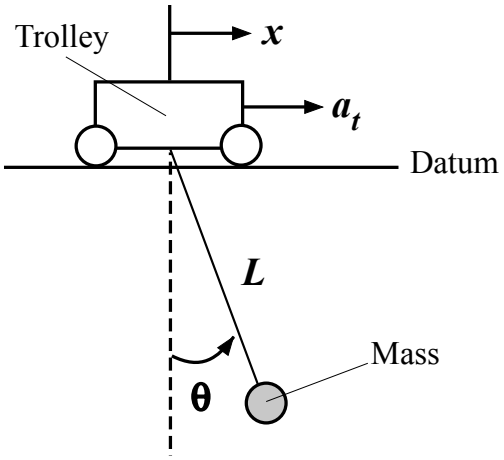

Figure 2.1: Model of a single-pendulum crane

dynamics, further machine flexibility could arise from drive components such as actuators and gears. Hard nonlinearities like deadzone at the actuator input and backlash in the gear teeth induce time-delay to the system and cause residual vibration [162]. In this chapter, the flexible dynamics of planar cranes with a single- and double-pendulum payload are examined to increase the understanding of their dynamics behavior.

2.1 Single-Pendulum Payload

Figure 2.1 shows a model of a planar crane. The directly-controlled overhead trolley is moved via an acceleration input command a_t. The horizontal position of the trolley is indicated by distance x. The point-mass payload m is suspended via a massless, incompressible cable of length L. The swing angle of the payload measured with respect to the vertical axis of the trolley is represented by θ.

The nonlinear equation of motion of the single-pendulum crane model in terms of the generalized coordinate θ is:

$$\ddot{L}\sin\theta - L\dot{\theta}^2\sin\theta + L\ddot{\theta}\cos\theta + 2\dot{L}\dot{\theta}\cos\theta + g\sin\theta = -a_t\cos\theta \tag{2.1}$$

where, g is the acceleration due to gravity. The centrifugal acceleration $\dot{\theta}^2$ due to payload swing is small compared to g, and thus is neglected. Hard nonlinearities, such as the

Coulombian friction of trolley movement and the motor drive dynamics and components [163], are also neglected for simplicity.

The simplified dynamic equation of motion of the crane is obtained by considering the system to be a second-order, under-damped system. Assuming small swing angles, and a fixed cable length L, the linearized differential equation of motion becomes:

$$\ddot{\theta}(t) = -2\zeta\omega_n\dot{\theta} - \omega_n^2\theta - \frac{a_t}{L} \tag{2.2}$$

where, ω_n and ζ are the natural frequency and effective damping ratio of the system. The natural frequency is related to the suspension cable length by $\omega_n = \sqrt{g/L}$.

Although the equation of motion is based on an acceleration input, it is convenient to derive the governing equation in terms of the velocity input because a number of real crane applications often utilize velocity commands [104, 106, 158, 159, 160, 161]. To obtain a state space representation of the system using a velocity input, the expression in (2.2) is integrated and then multiplied by $-L$. Then, by assuming that the cable length is fixed, a state space representation can be obtained by defining the second state x_2 as the horizontal swing distance of the payload $-\theta L$, and the first state x_1 as the integral of x_2. The state equation of the system becomes:

$$\begin{bmatrix} \dot{x_1} \\ \dot{x_2} \end{bmatrix} = \begin{bmatrix} 0 & 1 \\ -\omega_n^2 & -2\zeta\omega_n \end{bmatrix} \begin{bmatrix} x_1 \\ x_2 \end{bmatrix} + \begin{bmatrix} 0 \\ 1 \end{bmatrix} v_t(t) \tag{2.3}$$

and the output equation becomes:

$$\theta(t) = \begin{bmatrix} 0 & \frac{-\omega_n^2}{g} \end{bmatrix} \begin{bmatrix} x_1 \\ x_2 \end{bmatrix} \tag{2.4}$$

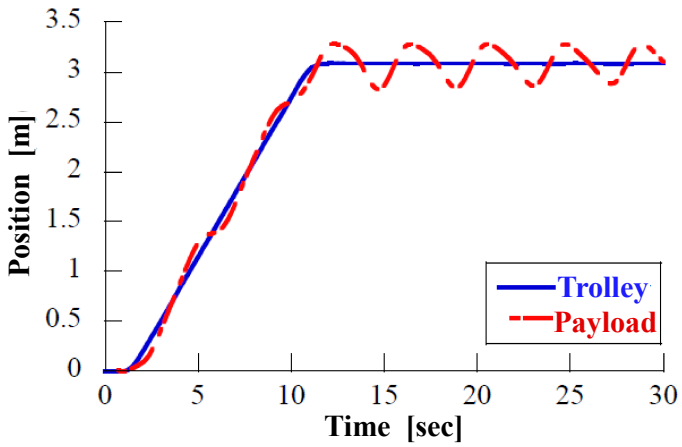

Figure 2.2: Trolley and payload responses of a single-pendulum crane [164]

The crane dynamics in transfer function form are:

$$\frac{\theta(s)}{V_t(s)} = \frac{\left(\frac{-\omega_n^2}{g}\right) s}{s^2 + 2\zeta\omega_n s + \omega_n^2} \tag{2.5}$$

An experimental payload response from a point-to-point motion of a physical bridge crane with a single-pendulum payload is shown in Figure 2.2. The payload oscillates around the trolley location both during and after the motion. Because of the near-zero damping of the crane, the oscillation persists for a long time unless stopped via external forces.

2.2 Double-Pendulum Payload

In some crane applications, adding an extra load to a hook via a rigging cable produces a double-pendulum payload system. Double-pendulum payloads constitute a critical subset of crane applications that arise in many material-handling processes. Double-pendulum payloads make the dynamics of cranes much more complex because they add an additional flexible mode and produce a two-mode oscillatory system.

A double-pendulum crane is shown in Figure 2.3. The trolley moves with an acceleration command input a_t, and its horizontal position is indicated by x. The hook m_1 is a

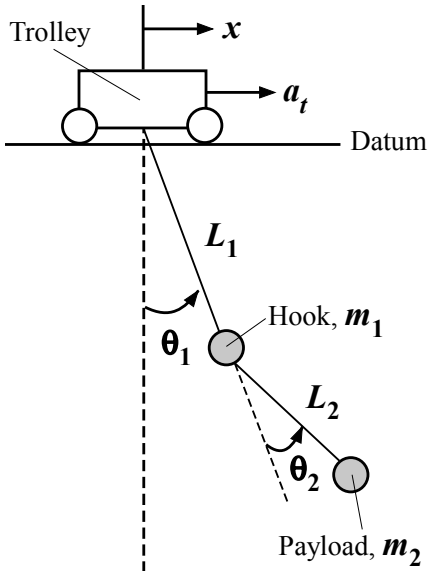

Figure 2.3: Model of a double-pendulum crane

point-mass suspended from the trolley via a massless hoist cable of length L_1. The payload m_2 is a point-mass attached to the hook via a massless rigging of a fixed length L_2. The swing angle of the hook is measured with respect to the position of the trolley, and is represented by θ_1. The swing angle of the payload θ_2 is measured with respect to the swing of the hook. Damping of the hook and payload swing is neglected ($\zeta = 0$).

The nonlinear equations of motion of the double-pendulum crane in terms of θ_1 and θ_2 are:

$$\begin{aligned}
&(m_1 + m_2)\left[L_1\ddot{\theta}_1 + g\sin(\theta_1) + 2\dot{L}_1\dot{\theta}_1\right] + \\
&m_2 L_2\left[\left(\ddot{\theta}_1 + \ddot{\theta}_2\right)\cos(-\theta_2) + \left(\dot{\theta}_1 + \dot{\theta}_2\right)^2\sin(-\theta_2)\right] \\
&= a_t(m_1 + m_2)\cos(\theta_1)
\end{aligned} \tag{2.6}$$

$$\begin{aligned}
&L_2\left(\ddot{\theta}_1 + \ddot{\theta}_2\right) + \ddot{L}_1\sin(-\theta_2) + g\sin(\theta_1 + \theta_2) - \\
&L_1\left[\dot{\theta}_1^2\sin(-\theta_2) - \ddot{\theta}_1\cos(-\theta_2)\right] + 2\dot{L}_1\dot{\theta}_1\cos(-\theta_2) \\
&= a_t\cos(\theta_1 + \theta_2)
\end{aligned} \tag{2.7}$$

Assuming small swing angles and constant cable length ($\dot{L}_1 = \ddot{L}_1 = 0$), the linearized differential equations of motion are:

$$\begin{aligned} \ddot{\theta}_1(t) &= -\left(\frac{g}{L_1}\right)\theta_1 + \left(\frac{gR_M}{L_1}\right)\theta_2 - \frac{a_t(t)}{L_1} \\ \ddot{\theta}_2(t) &= \left(\frac{g}{L_1}\right)\theta_1 - \Gamma\theta_2 + \frac{a_t(t)}{L_1} \end{aligned} \tag{2.8}$$

where,

$$\Gamma = \left(\frac{gR_M}{L_1} + \frac{gR_M}{L_2} + \frac{g}{L_2}\right) \tag{2.9}$$

where, R_M is the mass ratio of the payload to the hook.

To obtain the state space representation with the velocity input, the expressions in (2.8) are integrated and then multiplied by $-L_1$. Next, it is defined the state x_2 as the horizontal swing distance of the hook $-\theta_1 L_1$ and the state x_1 as the integral of x_2. Similarly, it is defined the state x_4 as $-\theta_2 L_1$ and the state x_3 as the integral of x_4. Then, the state equation becomes:

$$\begin{bmatrix} \dot{x_1} \\ \dot{x_2} \\ \dot{x_3} \\ \dot{x_4} \end{bmatrix} = \begin{bmatrix} 0 & 1 & 0 & 0 \\ -\frac{g}{L_1} & 0 & \frac{gR_M}{L_1} & 0 \\ 0 & 0 & 0 & 1 \\ \frac{g}{L_1} & 0 & -\Gamma & 0 \end{bmatrix} \begin{bmatrix} x_1 \\ x_2 \\ x_3 \\ x_4 \end{bmatrix} + \begin{bmatrix} 0 \\ 1 \\ 0 \\ -1 \end{bmatrix} v_t(t) \tag{2.10}$$

and the output equation is:

$$\vec{y} = \begin{bmatrix} x_1 & x_2 & x_3 & x_4 \end{bmatrix}^{\mathrm{T}} \tag{2.11}$$

An experimental payload response from a point-to-point motion of a double-pendulum crane is shown in Figure 2.4. Similar to the single-pendulum case in Figure 2.2, the payload oscillates around the trolley location and persists for a long time because of a low damping. The response exhibits two-mode oscillations where the frequencies and amplitudes depend on the double-pendulum configuration. This makes precise control of the payload difficult and decreases the operation efficiency and safety.

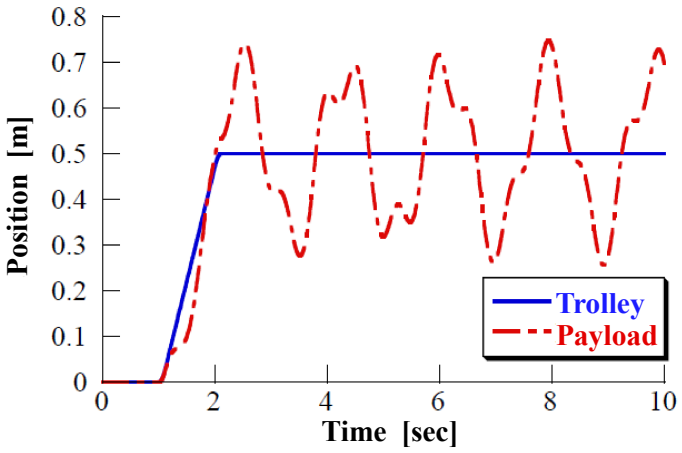

Figure 2.4: Trolley and payload responses of a double-pendulum crane [164]

CHAPTER 3
INPUT SHAPING

CHAPTER SUMMARY:

This chapter presents background information on input shaping method that serve as important basis for the work completed in this thesis. Section 3.1 provides detailed explanation of the concept and theory on input shaping. The designs of previous input shapers are presented. In Section 3.2, the energy-reduction characteristics of input shaping are presented.

A raw reference command generally induces a vibratory dynamic response when it is sent to a flexible system. For example, to improve the productivity and safety of crane operations, the payload swing needs to be limited at a low amplitude which allows the operator to transfer a payload in a fast and safe manner. Input shaping suppresses the command-induced vibration by convolving the command signal with a sequence of impulses called an *input shaper* [94, 95, 96]. The shaper is designed with the impulses of appropriate amplitudes and timings so that the vibration resulting from all of the impulses sums to be small or zero. The input shaper can be convolved with any arbitrary command function, and maintain the vibration-cancellation properties.

Figure 3.1 shows the input-shaped command obtained by convolving a reference step command with a two specially-timed positive impulses input shaper. The shaper contains two impulses with different magnitudes, A_1 and A_2, separated by a time difference ΔT. The resulting shaped command is composed of two step inputs, in which the second step is shifted by ΔT and the final signal amplitude equals to that of the original step command.

Figure 3.2 illustrates the concept of input shaping with a system response resulted from a two-impulse shaper. The vibratory responses due to the first impulse and the second

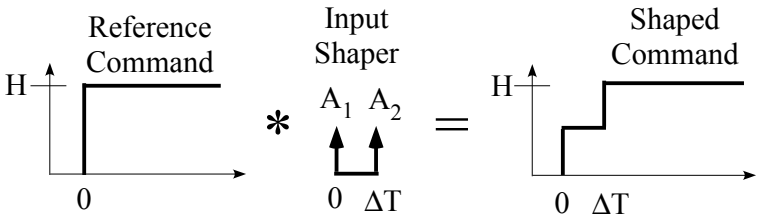

Figure 3.1: Step command convolved by a ZV shaper

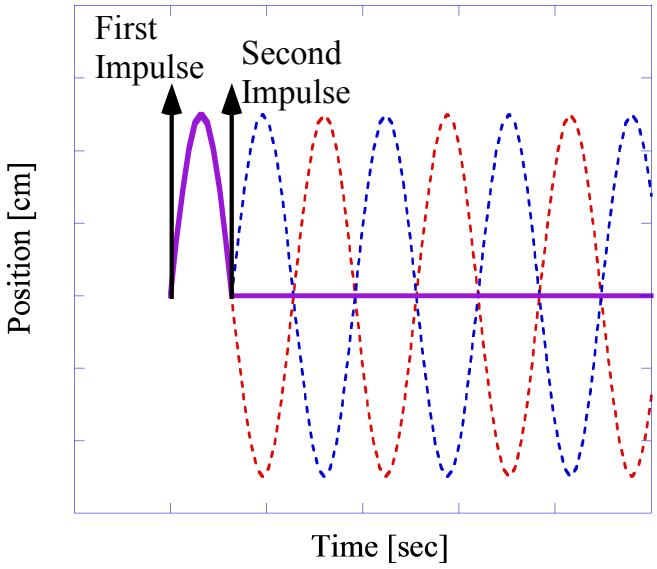

Figure 3.2: Dynamic vibration eliminated by a ZV shaper

impulse are plotted in dashed lines, and the total response of the system after the complete shaped command is plotted in a solid line. When the first impulse is applied to a flexible system it induces a vibratory response. A similar response would result when the second impulse is applied at the specific timing later. When the two responses combine linearly by superposition, the vibration due to the first impulse is canceled by the vibration due to the second impulse. As a result, the sum of these two responses eliminates the vibration in the system response. However, the downside is that the command rise time is increased by the duration of the impulse sequence.

3.1 Theoretical Background

To design an input shaper, the impulse amplitudes and time locations need to be determined while satisfying certain design constraints. The main design constraint is a vibration amplitude limit. To form a non-dimensional vibration amplitude, the vibration amplitude of an under-damped, second-order system from a sequence of *n* impulses is divided by the amplitude of residual vibration from a single impulse of unity magnitude at time zero. The resulting expression, called the percentage residual vibration (*PRV*), gives the ratio of vibration with input shaping to that without input shaping [94]:

$$PRV = V(\omega, \zeta) = e^{-\zeta\omega t_n}\sqrt{[C(\omega,\zeta)]^2 + [S(\omega,\zeta)]^2} \tag{3.1}$$

where,

$$C(\omega,\zeta) = \sum_{i=1}^{n} A_i e^{\zeta\omega t_i} \cos\left(\omega t_i \sqrt{1-\zeta^2}\right) \tag{3.2}$$

$$S(\omega,\zeta) = \sum_{i=1}^{n} A_i e^{\zeta\omega t_i} \sin\left(\omega t_i \sqrt{1-\zeta^2}\right) \tag{3.3}$$

In the expression above, ω and ζ are the natural frequency and damping ratio of the undesired vibratory mode, and A_i and t_i are the i^{th}-impulse amplitude and time, respectively.

There have been many types of input shapers developed. The simplest form of a positive-magnitude impulse input shaper is called a *Zero-Vibration* (ZV) shaper. ZV shaper is obtained by setting the PRV in (3.1) equal to 0, or aiming for a perfect elimination of vibration. The closed-form expression of the shaper is given by [95]:

$$ZV = \begin{bmatrix} A_i \\ t_i \end{bmatrix} = \begin{bmatrix} \frac{1}{1+K} & \frac{K}{1+K} \\ 0 & 0.5T_d \end{bmatrix} \tag{3.4}$$

where, T_d is the damped period and the parameter K is calculated as:

$$K = e^{\frac{-\zeta\pi}{\sqrt{1-\zeta^2}}} \tag{3.5}$$

Note that the impulse amplitudes and timings are functions of the system's natural frequency and damping ratio.

The ZV shaper design only contains two impulses, having a relatively shorter time delay of $t_2 = 0.5T_d$, which makes it one of the faster shapers. The shaper, however, has to be designed precisely for exact vibration cancellation because it is susceptible to target frequency estimation error. When designed with an inaccurate frequency, the vibration reduction effectiveness degrades significantly.

To resolve this issue, more robust input shaper designs were developed. The earliest form of robust input shaping was achieved by setting the derivative of the residual vibration equation (3.1) with respect to the frequency equal to zero:

$$\frac{\mathrm{d}}{\mathrm{d}\omega}\left(e^{-\zeta\omega t_n}\sqrt{\left[C\left(\omega,\zeta\right)\right]^2+\left[S\left(\omega,\zeta\right)\right]^2}\right)=0 \tag{3.6}$$

The resulting shaper is called a *Zero Vibration and Derivative* (ZVD) shaper. The closed-form expression of the shaper design is given by [94]:

$$ZVD = \begin{bmatrix} A_i \\ t_i \end{bmatrix} = \begin{bmatrix} \frac{1}{1+2K+K^2} & \frac{2K}{1+2K+K^2} & \frac{K^2}{1+2K+K^2} \\ 0 & 0.5T_d & T_d \end{bmatrix} \tag{3.7}$$

Note that the duration of the ZVD shaper is $t_3 = T_d$, which is twice that of the ZV Shaper.

The zero derivative constraint increases the shaper's robustness to estimation error in the targeted frequency. This constraint can be imposed repeatedly by taking additional higher-order derivatives with respect to frequency. The next derivative-method shaper is

called a ZVDD shaper, and is described by [94]:

$$ZVDD = \begin{bmatrix} A_i \\ t_i \end{bmatrix} = \begin{bmatrix} \frac{1}{1+3K+3K^2+K^3} & \frac{3K}{1+3K+3K^2+K^3} & \frac{3K^2}{1+3K+3K^2+K^3} & \frac{K^3}{1+3K+3K^2+K^3} \\ 0 & 0.5T_d & T_d & 1.5T_d \end{bmatrix} \tag{3.8}$$

As shown, input shapers can have two or more impulses. The general form of the transfer function for a input shaper with *n* impulses is:

$$\mathbb{G}_{IS} = A_1 e^{-t_1 s} + A_2 e^{-t_2 s} + \cdots + A_n e^{-t_n s} \tag{3.9}$$

The first impulse time t_1 can set to zero without a loss of generality. The impulse amplitudes A_ns and time locations t_ns are obtained using the estimated natural frequencies and damping ratios of the undesired flexible modes.

The price for the additional robustness provided by the derivative constraint is an increased shaper duration by one-half period of the natural frequency, $t_4 = 1.5T_d$. This means that input shapers can be made robust to error at the cost of slower rise time. The details on design constraints and derivation processes for ZV, ZVD, and ZVDD shapers can be found in [94]. In addition, it is possible to obtain input shapers that are more robust to errors and variations in the parameters [98].

3.2 Energy Reduction Effect

One of the benefits of input shaping is the command smoothing effect. By filtering the input command via the convolution method, input shaping modifies the command into a signal that is more easily tracked by the actuator. This also means the reduction in the maximum control effort, and thus, the energy usage by the actuator [156, 157]. Note that if input shapers containing negatively-valued impulses are used, then the shaped reference commands can be more difficult to track by actuator [130].

Figure 3.3 shows step velocity command of magnitude *H* convolved with a n-impulse

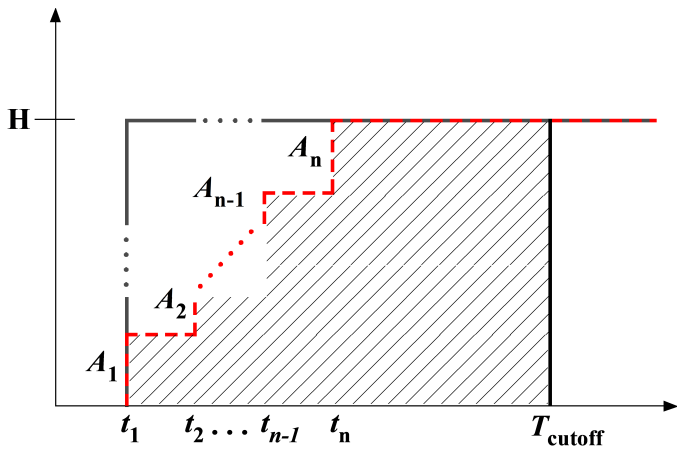

Figure 3.3: Step velocity command modified by an input shaper

shaper containing only positive impulses. The solid and dashed line profiles are the raw and shaped velocity commands respectively. The time t_1 represents the starting moment of the command, and T_{cutoff} is an arbitrary timing after reaching the final velocity magnitude. The shaded area between t_1 and T_{cutoff} represents the total distance traveled by the shaped command. The plot shows that the distance traveled by the raw command, or the area under the profile, is more than that of the shaped command. This is because the shaped command takes a longer time to increase its magnitude due to the partial time-delays induced by the convolution.

As the result, the average velocity of the shaped command u_{ave} becomes less than the raw command u. The normalized average velocity of the shaped command $\bar{u}_{ave}$ by the magnitude of the step input can be calculated as:

$$\begin{aligned} \bar{u}_{ave} &= \frac{1}{H} u_{ave} = \frac{1}{H}\left[\frac{D_{total}-D_{miss}}{T_{cutoff}-t_1}\right] \\ &= \frac{1}{H}\left[\frac{HT_{cutoff}-\sum_{i=1}^{n-1}\sum_{j=1}^{n-i} HA_{i+j}(t_{i+1}-t_i)}{T_{cutoff}-t_1}\right] \end{aligned} \tag{3.10}$$

where, D_{total} is the total distance traveled by the raw command and D_{miss} is the distance not traveled by the shaped command.

The term $\bar{u}_{ave}$ can be compared to the normalized raw command $\bar{u}$:

$$\bar{u}_{ave} = c \cdot \bar{u} = c \cdot \frac{u}{H} \tag{3.11}$$

where, $c \leqslant 1$ is the ratio relating the input-shaped velocity magnitude to that of the average velocity.

The energy generated by the velocity command can be characterized by using the definition of kinetic energy:

$$E \sim \bar{u}_{ave}^2 \sim c^2 \cdot \bar{u}^2 \sim \gamma \cdot \bar{u}^2 \tag{3.12}$$

where, $\gamma = c^2 \leqslant 1$ is the representative energy reduction index by an input shaper. The low magnitude of γ suggests a large energy reduction via input shaping.

Figure 3.4 shows the energy reduction characteristics of different input shapers during the acceleration phase. The index γ of ZV, ZVD, and ZVDD shapers for $\zeta = 0$, 0.35, and 0.70 are calculated and plotted against the shaper duration normalized by the longest damped period used in the calculation. The reduction index γ results in less than 1 for all input shapers and shows that actuator energy is reduced. The plot shows that the ZVDD shaper returns the lowest γ values followed by the ZVD and ZV shapers in all damping cases. This is because, as shown in (3.4-3.8), the ZVDD shapers result in the longest shaper duration. Thus, the ZVDD shaper increases the command's velocity magnitude slower than ZVD and ZV shapers, resulting in a lower average velocity and actuator energy usage.

Another key point from Figure 3.4 is that the γ value increases with an increase in the damping ratio for all shapers. At high damping, input shapers barely reduce energy usage. This is because of the K parameter shown in (3.5). A higher damping ratio ζ results in a lower value of K, which makes the first shaper impulse more dominant than other succeeding impulses. As ζ approaches 1, K gets close to 0 and essentially turns the shaper into a single-impulse shaper, which makes no significant changes to the original command and thus does not significantly reduce energy consumption. In addition, the vibration reduction

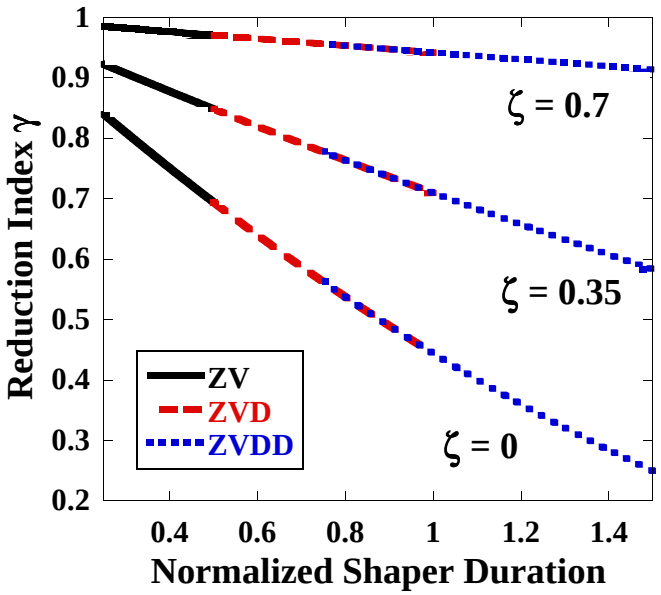

Figure 3.4: Energy reduction index γ against the shaper durations at the acceleration

benefit of input shaping also becomes less significant with higher damping.

CHAPTER 4
MODEL REFERENCE CONTROL

CHAPTER SUMMARY:

This chapter explains the type of model reference control utilized in the combined IS-MRC controller. In Section 4.1, the structure of model reference control is described. The derivation of the Lyapunov control law is presented in Section 4.2. The control law is designed to be asymptotically stable. Section 4.3 demonstrates typical MRC responses using numerical simulation. The payload responses and control signals are analyzed.

Nonlinear characteristics in the payload dynamics can make the formulation of an accurate system model difficult. This leads to the challenge of developing a robust controller design. The performance of a controller can be degraded by system parameter variations arising from parameter estimation uncertainties and un-modeled plant nonlinearities. Thus, it is essential to design a control method that can perform properly without precise knowledge of the plant dynamics. A solution to such control problem is model reference control (MRC), an adaptive control strategy that is useful when controlling complex systems.

4.1 MRC Structure

Figure 4.1 shows the block diagram of MRC with a velocity reference command signal. The controller consists of three main blocks; a reference model, a plant, and a control law. A command signal v is sent to the reference model to calculate the desired states $\mathbf{x_d}$. The signal v is also sent to the control law block, which also takes in $\mathbf{x_d}$ and the plant states $\mathbf{x}$, to formulate a control signal u that controls the actual plant.

The state space representation is used to describe both the reference model and plant.

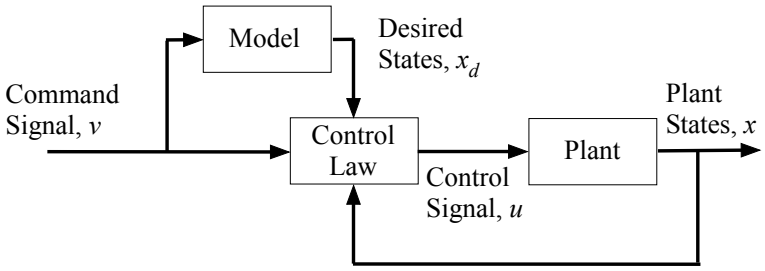

Figure 4.1: Model reference control block diagram

The state equation of the reference model of MRC is defined as:

$$\dot{\mathbf{x_d}} = \mathbf{A_m x_d} + \mathbf{B_m} v_t \tag{4.1}$$

where, $\mathbf{A_m}$ and $\mathbf{B_m}$ are the state equation matrices of the reference model. Similarly, the state equation of the plant is:

$$\dot{\mathbf{x}} = \mathbf{A_p x} + \mathbf{B_p} u \tag{4.2}$$

where, $\mathbf{A_p}$ and $\mathbf{B_p}$ are the state equation matrices describing the plant dynamics.

The following assumptions are made for simplification. First, the state vector $\mathbf{x}$ is available online and can be obtained via sensor measurements or a state observer [165]. Secondly, the plant parameters are also available or can be reasonably estimated. This assumption is justifiable because many practical systems are modeled as linear time-varying systems [73], or the physical nonlinear plant parameters can be reasonably estimated [75].

4.2 Lyapunov Control Law

The original approach to developing the control law is called the MIT rule. The MIT rule had been implemented on actual systems [166], and also been analyzed for systems of different order and compared with conventional techniques [167, 168, 169]. However, the drawback of the MIT rule is that there is no guarantee of stability in the resulting closed loop system. To overcome this issue, the control law using the concept of Lyapunov's

theory was derived.

4.2.1 Direct Method of Lyapunov

Lyapunov's direct method has proven to be a useful tool for nonlinear system controller design and stability analysis. The method is a mathematical interpretation of a physical system whose total energy is dissipating. In such cases, the system states will ultimately reach an equilibrium point. The theorem is referred to as the direct method of Lyapunov (also called the second method of Lyapunov) because there is no need to solve the differential equations of motion to determine the stability of the system.

The Lyapunov stability theorem states: Let $\mathbf{x} = 0$ be an equilibrium point for a dynamic system described by:

$$\dot{\mathbf{x}} = f(\mathbf{x}) \tag{4.3}$$

where $f(\mathbf{x}) : D \rightarrow \mathbf{R}^n$ is locally Lipschitz continuous with respect to $\mathbf{x}$ and $D \subset \mathbf{R}^n$ is a domain containing the origin. Let the scalar function $V(\mathbf{x}) : D \rightarrow \mathbf{R}$ be a Lyapunov function (continuously differentiable, positive definite) in D, where $\dot{V}(\mathbf{x})$ is negative semi-definite in the region $D : \dot{V}(\mathbf{x}) \leq 0$. Then, $\mathbf{x} = 0$ is an asymptotically stable equilibrium point if $\dot{V}(\mathbf{x})$ is negative definite.

In this work, the crane system function $f(\mathbf{x}, u, t)$ is assumed to have an unique solution within the region D for given initial condition $\mathbf{x}_0 = \mathbf{x}(0)$, or f is locally Lipschitz on $(\mathbf{x}, u, t)$ and $f(\mathbf{0}, 0, 0) = 0$. It is intuitive that a crane has a locally stable equilibrium point when the payload is hanging straight down, and an unstable equilibrium point when it is pointing straight up. If the crane has damping, then the stable equilibrium point is asymptotically stable.

The Lyapunov theory can ensure that a closed loop system is asymptotically stable. The concept had been used to develop controllers for linear motor drives [170] and improve the performance of a shunt active power filter [171, 172]. Also, it had been shown that the

control law obtained from Lyapunov theory outperforms that of the MIT rule in the sense that the controller is simpler, allows more freedom in choosing arbitrary parameter/gain values, and has smaller overshoot and settling time [173].

4.2.2 Control Law Derivation

The second method of Lyapunov is applied to formulate the explicit control law that generates the control signal u such that the actual plant states follow the dynamic behavior of the reference model. The error between the desired model state vector, $\mathbf{x_d}$, and the plant states, $\mathbf{x}$, is defined as:

$$\mathbf{e} = \begin{bmatrix} e_1 \\ e_2 \end{bmatrix} = \mathbf{x_d} - \mathbf{x} = \begin{bmatrix} x_{d,1} - x_1 \\ x_{d,2} - x_2 \end{bmatrix} \tag{4.4}$$

The objective is to design the control law u for the plant such that the error between the plant states and desired model states asymptotically converges to zero:

$$\lim_{t \to \infty} \|\mathbf{e}(t)\| = 0 \tag{4.5}$$

In other words, $\mathbf{x}$ should be driven to follow the desired reference states $\mathbf{x_d} \in \mathbf{R}^n$ with a guarantee of closed-loop asymptotical stability.

Substituting the expressions from (4.1) and (4.2) into the time derivative of the error signal yields:

$$\dot{\mathbf{e}} = \dot{\mathbf{x_d}} - \dot{\mathbf{x}} = (\mathbf{A_m x_d} + \mathbf{B_m} v_t) - (\mathbf{A_p x} + \mathbf{B_p} u) \tag{4.6}$$

where, $\mathbf{A_m} \in \mathbf{R}^{n \times n}$ and $\mathbf{B_m} \in \mathbf{R}^n$. The eigenvalues of the reference model state matrix $\mathbf{A_m}$ are assumed to have negative real parts. This assumption is critical as instability can occur if the model and its parameters are chosen inappropriately.

Assume that the error between the states of the controlled plant and the reference model has the form of (4.3), and satisfies the conditions of Theorem 4.2.1. Then, define a Lya-

punov function of the error to be a radially unbounded positive definite function:

$$V(\mathbf{e}) = \mathbf{e}^T\mathbf{P}\mathbf{e} \tag{4.7}$$

Taking the time derivative and assuming that the plant states asymptotically tracks the model states (i.e. $\mathbf{x_d} \simeq \mathbf{x}$), the expression gives:

$$\begin{aligned} \dot{V}(\mathbf{e}) &= \dot{\mathbf{e}}^T\mathbf{P}\mathbf{e} + \mathbf{e}^T\mathbf{P}\dot{\mathbf{e}} \\ &= \mathbf{e}^T(\mathbf{A_m}^T\mathbf{P} + \mathbf{P}\mathbf{A_m})\mathbf{e} + 2M \end{aligned} \tag{4.8}$$

where,

$$M = \mathbf{e}^T\mathbf{P}[(\mathbf{A_m} - \mathbf{A_p})\mathbf{x} - \mathbf{B_p}u + \mathbf{B_m}v_t] \leqslant -\lambda \tag{4.9}$$

In order to make the derivative of the Lyapunov function $\dot{V}(\mathbf{e})$ always negative to ensure the asymptotical stability of the controller, two conditions have to be satisfied. First, the matrix $\mathbf{P}$ must be selected according to the theorem: The LTI reference model $\dot{\mathbf{x_d}} = \mathbf{A_m}\mathbf{x_d} + \mathbf{B_m}v$ is asymptotically stable if and only if there exists a unique symmetric positive definite matrix $\mathbf{P}$ for any real, symmetric, positive-definite matrix $\mathbf{Q}$ (i.e. $\mathbf{Q} = \mathbf{I}$) satisfying:

$$\mathbf{A_m}^T\mathbf{P} + \mathbf{P}\mathbf{A_m} = -\mathbf{Q} \tag{4.10}$$

Secondly, the scalar quantity M must be set to a non-positive value (i.e. $M \leq -\lambda$) by forming an appropriate expression of u. By taking the expression for M in (4.9) and solving for the control signal u yields:

$$u = \frac{\mathbf{e}^T\mathbf{P}\mathbf{A_m}\mathbf{x} - \mathbf{e}^T\mathbf{P}\mathbf{A_p}\mathbf{x} + \mathbf{e}^T\mathbf{P}\mathbf{B_m}v + \lambda}{\mathbf{e}^T\mathbf{P}\mathbf{B_p}} \tag{4.11}$$

The control law expression for u takes into account both the parameter modeling errors

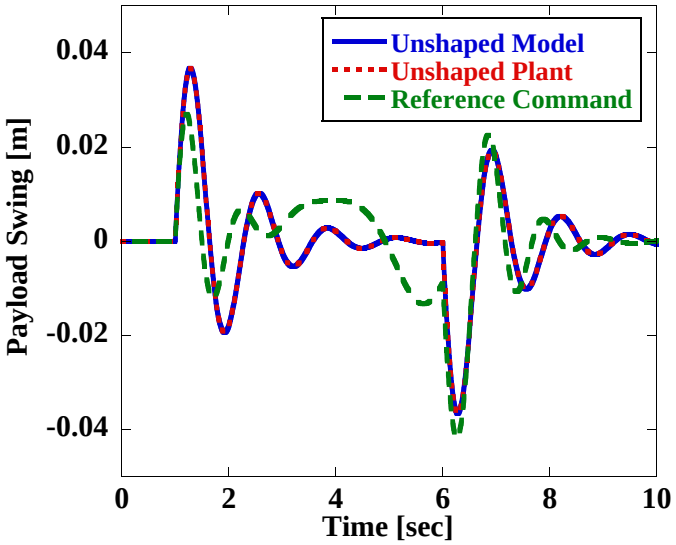

Figure 4.2: Responses from plant, MRC reference model and controlled plant

and the state tracking errors. The u signal can be influenced significantly by the parameter estimation error between the reference model and the actual plant, which leads to a higher control effort and possibly actuator saturation.

4.3 Numerical Simulation

A numerical simulation was used to develop fundamental understanding of the performance characteristics of the MRC controller. The simulation was formulated to demonstrate crane control. The state tracking and control signal of the MRC controller were the primary outputs of interest.

The state tracking performance was demonstrated by running the simulation with the parameter variance between the reference model and plant set to 30%. Figure 4.2 shows the payload swing amplitude resulting from a trapezoidal velocity reference command turned on at $t = 1$ sec and turned off at $t = 6$ sec. The lines represent the state responses from the MRC reference model and plant, and the state response of the plant that would occur when the reference command was supplied directly. The plant response via the reference command differs significantly from the desired response of the reference model due to the parameter variance. By using the MRC controller, the desired model response is tracked

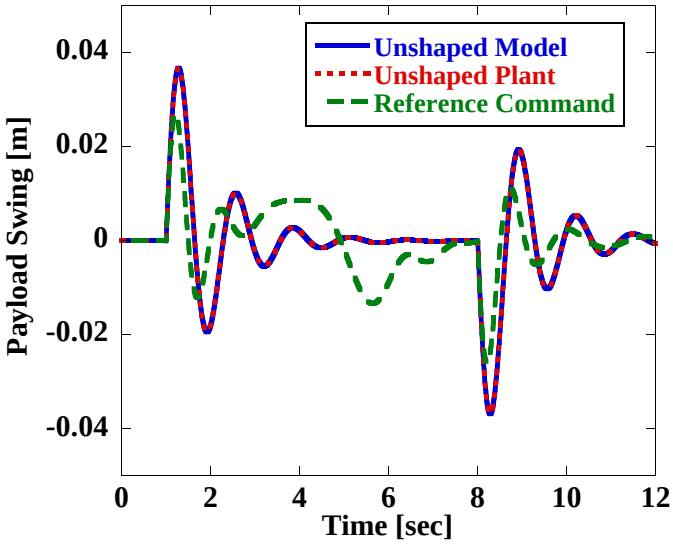

Figure 4.3: Responses at different stop time of $t = 8$ sec

nearly perfectly by the plant response (the order of the tracking error is $\sim 10^{-8}$m at the highest).

The same simulation case was tested with a different stop timing. Figure 4.3 shows the swing distances of payload with a trapezoidal velocity reference command that has different OFF command timing at $t = 8$ sec. Similar to Figure 4.2, the plant response via a reference command differs significantly from the reference model response due to the 30% parameter variance. The MRC controller successfully modifies the plant response to track the desired model response almost perfectly.

The control effort of the system under different parameter variances was analyzed. Figure 4.4 shows the trapezoidal velocity input signals generated by the MRC controller with different parameter variances in the plant. The lines represent the variances of 0.1%, 15%, and 30% respectively. The velocity inputs fluctuate because the parameter variations are introduced in a form of a sinusoidal function. The signals with the larger parameter variance has larger signal overshoot, indicating that more control effort is necessary to drive the plant to the same desired states. This agrees with the control law derived in (4.11), which implies that a larger error between the model and the plant results in a larger control effort. Also, the larger variance results in a signal with more amplitude variation. This is

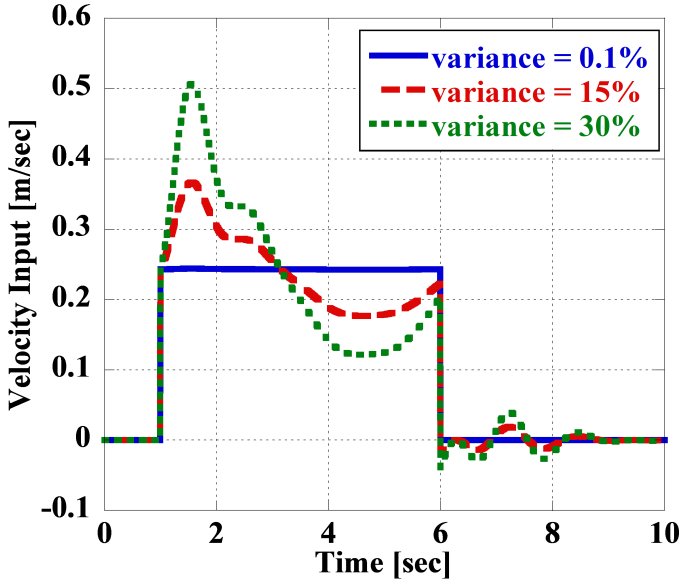

Figure 4.4: Control signals resulting from different parameter variances

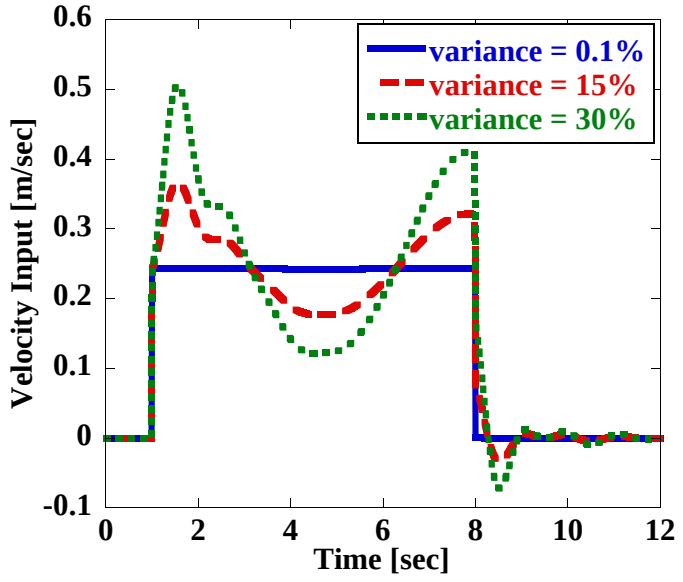

Figure 4.5: Control signals ending at $t = 8$ sec

undesirable for the actuator life-expectancy and energy consumption.

Figure 4.5 shows the results from the case with the OFF command timing at $t = 8$ sec. The figure shows very similar characteristics as Figure 4.4. The major difference can be observed between $t = 6$ sec and $t = 8$ sec due to the continued application of a non-zero reference velocity.

4.4 Summary

In this chapter, a model reference control scheme that forms a basis for this research was explained. The state space representations of the reference model and plant were presented. The theory of the direct method of Lyapunov was explained. The Lyapunov theory was then used to obtain the expression for the MRC control law that ensures that the resulting controller is asymptotically stable.

The performance of the MRC controller with the Lyapunov control law was demonstrated via numerical simulations. The state tracking and control effort of the MRC controller were observed for a crane with parameter variances. The state of the reference model was almost perfectly tracked by the plant state despite 30% parameter variance. However, the parameter variances caused significant impact on the control effort magnitude. Larger control effort was required to modify the plant dynamics with large parameter variance.

CHAPTER 5

INPUT-SHAPED MODEL REFERENCE CONTROL

CHAPTER SUMMARY:

This chapter explains the proposed control method of input-shaped model reference control. The IS-MRC design is developed and tested on a crane with a single-pendulum payload. Section 5.1 explains the structure of the IS-MRC scheme. The controller design is illustrated with the derivation of the Lyapunov control law and a Zero-Vibration input shaper. In Section 5.2, the performance of the proposed IS-MRC design is examined by numerical simulations and verified by physical experiments. The linearizing effect, state tracking, oscillation suppression, and control effort reduction of the control scheme are analyzed as a function of modeling errors.

In Chapter 4, MRC controller was shown to be effective in driving a poorly modeled plant in a desired manner. The method, however, raises the possibility of exceeding the maximum controller effort. In order to realize both excellent tracking performance and feasible control effort, a control method that combines input shaping and MRC, called input-shaped model reference control (IS-MRC), is proposed. The IS-MRC method is designed to improve the overall controller robustness, while reducing the residual vibrations and mitigating the effects of plant nonlinearities. In this chapter, the controller design is explained by determining the reference model and plant parameters, deriving the control signal expression, and designing an input shaper. The IS-MRC design is tested on the single-pendulum crane that was described in Section 2.1. The controller is analyzed in terms of state tracking, oscillation reduction, and control effort reduction performance as a function of modeling errors.

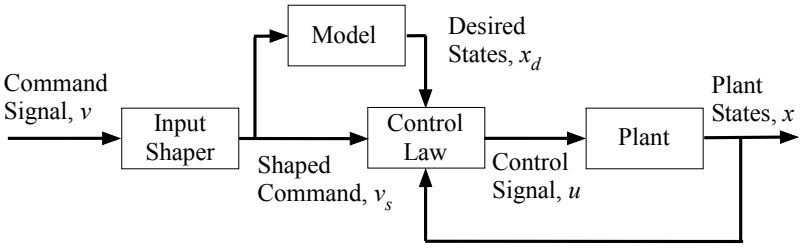

Figure 5.1: Input-shaped model reference control block diagram

5.1 IS-MRC Controller Design

The block diagram of IS-MRC is presented in Figure 5.1. The controller is constructed by connecting an input shaper and MRC in series. A velocity command input v is first sent through the input shaper to obtain a shaped velocity command v_s. The shaped command is then sent to the MRC scheme described in Figure 4.1. The desired system states $\mathbf{x_d}$ become vibration-free because the input shaper is designed to eliminate the vibration mode in the reference model. The rate of change in the control signal u would be restricted via an acceleration limit of the actuator.

5.1.1 Reference Model and Plant

The reference model used in MRC can be a linear or nonlinear system. In this work, the reference model is selected to be a linearized single-pendulum crane. This one-mode model is utilized because it is easy to implement and a single-pendulum is a very good representation of an actual crane when it does not carry a payload, or when the payload behaves as a lumped mass attached to the hook.

The state equation of the single-pendulum reference model is:

$$\begin{aligned} \dot{\mathbf{x_d}} &= \mathbf{A_m x_d} + \mathbf{B_m} v_t \\ = \begin{bmatrix} \dot{x_{d,1}} \\ \dot{x_{d,2}} \end{bmatrix} &= \begin{bmatrix} 0 & 1 \\ -\omega_m^2 & -2\zeta_m\omega_m \end{bmatrix} \begin{bmatrix} x_{d,1} \\ x_{d,2} \end{bmatrix} + \begin{bmatrix} 0 \\ 1 \end{bmatrix} v_t \end{aligned} \tag{5.1}$$

where, $\mathbf{A_m}$ and $\mathbf{B_m}$ are the state equation matrices, and ω_m and ζ_m are the natural frequency and the damping ratio of the reference model.

Similarly, the state equation of the crane plant is:

$$\begin{aligned} \dot{\mathbf{x}} &= \mathbf{A_p}\mathbf{x} + \mathbf{B_p}u \\ &= \begin{bmatrix} \dot{x_1} \\ \dot{x_2} \end{bmatrix} = \begin{bmatrix} 0 & 1 \\ -\omega_n^2 & -2\zeta\omega_n \end{bmatrix} \begin{bmatrix} x_1 \\ x_2 \end{bmatrix} + \begin{bmatrix} 0 \\ 1 \end{bmatrix} u \end{aligned} \tag{5.2}$$

where, $\mathbf{A_p}$ and $\mathbf{B_p}$ are the state equation matrices of the plant, and ω_n and ζ are the natural frequency and the damping ratio of the plant.

5.1.2 Shaper Design

In this work, a ZV shaper discussed in Section 3.1 is utilized to reduce the payload swing θ because the single-pendulum payload crane only has one mode of oscillation. The ZV shaper is combined with a MRC, and the proposed controller design is called *Zero-Vibration Model Reference Control* (ZV-MRC) [174].

The ZV shaper is designed to obtain vibration-free states in the reference model. Thus, the modeling parameters needed to calculate the ZV shaper are the natural frequency ω_m and the damping ratio ζ_m of the reference model. They are applied to the ZV shaper design in (3.4) to obtain the numerical values of the impulses' amplitude and timing.

$$\text{ZV Shaper} = f\left(\omega_m, \zeta_m\right) \tag{5.3}$$

5.1.3 Control Law

When applying the control law derived in (4.11) to the single-pendulum crane, the expressions in (4.4), (5.1), and (5.2) are utilized. The arbitrary scalar constant λ is assigned as $\lambda = (e_1 P_{1,2} + e_2 P_{2,2})^2$, where $P_{1,2}$ and $P_{2,2}$ are the entries in the $\mathbf{P}$ matrix. Then, the

control signal u becomes:

$$u = (-\omega_m^2 + \omega_n^2)x_1 + (-2\zeta_m\omega_m + 2\zeta\omega_n)x_2 + v_t + \Lambda \tag{5.4}$$

where,

$$\Lambda = \begin{cases} 0.05|v_{max}| & \text{if} \quad e_1P_{1,2} + e_2P_{2,2} > 0.05|v_{max}| \\ e_1P_{1,2} + e_2P_{2,2} & \text{if} \quad -0.05|v_{max}| \leqslant e_1P_{1,2} + e_2P_{2,2} \leqslant 0.05|v_{max}| \\ -0.05|v_{max}| & \text{if} \quad e_1P_{1,2} + e_2P_{2,2} < -0.05|v_{max}| \end{cases} \tag{5.5}$$

The saturation condition of $\pm 0.05|v_{max}|$ is enforced on the Λ term. This is based on the observation that chattering is mainly caused by small tracking errors that contain mostly noise and computation round-off errors. Because the term $(e_1P_{1,2}+e_2P_{2,2})$ could be volatile and result in chattering of the control signal, a cutoff range of 5% of the maximum velocity magnitude $|v_{max}|$ of the reference command is set to limit the chattering. Also, the saturation condition prevents unexpected control effort overshoot due to measurement errors.

The expression in (5.4) satisfies the condition $M < 0$, and thus guarantees the asymptotic stability of the controller. The expression for u takes into account both the parameter modeling errors and the state tracking errors. The u signal can be influenced significantly by the parameter estimation error between the reference model and the actual plant, which leads to a higher control effort and actuator saturation. Because of the squared term, the error in the natural frequency is expected to exhibit more effects than the error in damping ratio.

5.2 Performance Verification

Numerical simulations and experimental data were used to examine the proposed ZV-MRC controller. The effectiveness and robustness of ZV-MRC were examined for its state tracking, oscillation suppression, and control effort reduction performances.

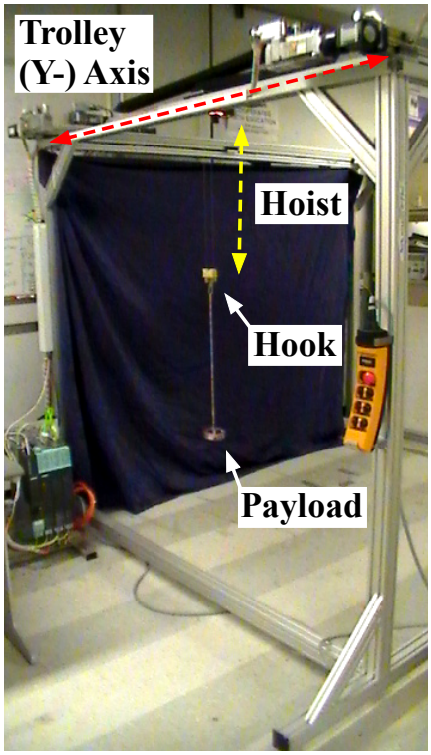

Figure 5.2: Small-scale bridge crane experimental setup

5.2.1 Small-Scale Bridge Crane

The small-scale bridge crane shown in Figure 5.2 was used to conduct experiments. The overhead trolley can be translated along the axis via a velocity command, and the suspension cable can be hoisted to the desired length. In this work, the cable carries only a hook mass that creates a single-pendulum payload crane. A machine vision system measures the position of the hook via a downward-pointing camera attached on the trolley. Some key parameters of the bridge crane are listed in Table 5.1. Experiments were conducted with the trolley and payload initially at rest. Then, they trolley was accelerated to a constant velocity. Data was recorded until the trolley was stopped at the edge of the crane workspace.

Table 5.1: Small-scale bridge crane parameters

v_{max}	0.20 m/sec
a	1.00 m/sec^2
m	0.69 kg
$\dot{L}$	0.16 m/sec

5.2.2 Performance Indices

Kozak et al. reviewed and interpreted a number of performance measures for input shaping and residual vibration of flexible systems [175]. In this analysis, performance indices were defined to quantify and compare the ZV-MRC performance to that of regular MRC. The state tracking index ε is:

$$\varepsilon = \frac{\int \left(x_2 - x_{d,2}\right)^2 dt}{\int \left(x_2 - x_{d,2}\right)^2 dt_{MRC,sim}} \tag{5.6}$$

The integral squared error measure between the desired and actual payload swing is normalized via the measure from the simulated MRC case. The performance of the MRC, without input shaping, is treated as the datum to compare the IS-MRC performance. The index measures how closely the plant tracks the states defined by the reference model. Lower values indicate better tracking performance.

Monitoring of the control effort for energy usage and actuator saturation is an important consideration. The control effort index μ that measures the energy usage is:

$$\mu = \frac{\int u^2 dt}{\int v_{ref}^2 dt} \tag{5.7}$$

The index μ shows a representative value of the kinetic energy in the trolley. The integral square of the control signal u is normalized via the value using the raw reference command v_{ref} (which is the same as v_t in (5.4)).

The maximum value of the control signal $u(t)$ is also of interest. It is normalized via

the maximum value of the reference command v_{max}:

$$U_{max} = \frac{Max(\ u(t)\ )}{v_{max}} \tag{5.8}$$

In both control effort indices, values of less than 1.0 are desired because they indicate less control effort requirements than with the baseline reference command. However, there is a trade-off for having a low μ value. A low μ value generally means a slower average velocity and leads to a longer move time. Thus, it may be favorable to have the μ value close to 1.0 in order to maintain about the same level of the kinetic energy in the trolley.

5.2.3 Linearizing effect

Input shaping improves the robustness of MRC by limiting the payload oscillations and minimizing the complex behavior of the reference model and the plant. This is equivalent to limiting the dynamics of the crane so that it remains near its equilibrium point. This linearization effect of input shaping is very beneficial for IS-MRC in terms of reducing the control effort.

To study this effect, the nonlinear crane given in (2.1) was tested in simulation and the control effort was observed for ZV-MRC and MRC cases. In this simulation, the degree of the system nonlinearity is varied by an index η that modifies the nonlinear element terms as:

$$\sin(\theta) \rightarrow \eta \cdot \sin(\theta) + (1 - \eta)\,\theta \tag{5.9}$$

$$\cos(\theta) \rightarrow \eta \cdot \cos(\theta) + (1 - \eta) \tag{5.10}$$

$$\dot{\theta} \rightarrow \eta \cdot \dot{\theta} \tag{5.11}$$

where, $\eta = 0$ represents a linearized system and $\eta = 1$ represents full nonlinearity of the

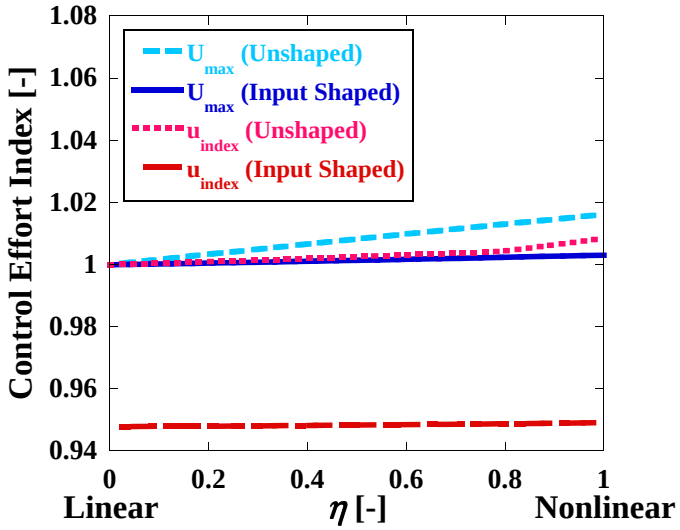

Figure 5.3: Control effort of ZV-MRC and MRC against η

system.

By assuming that the pendulum length, L, remains fixed ($\dot{L} = \ddot{L} = 0$) and substituting the expressions in (5.9)−(5.11), the nonlinear equation of motion becomes:

$$\ddot{\theta}(t) = \frac{-g + L\left(\eta \cdot \dot{\theta}\right)^2}{L\left[\eta \cdot \cos(\theta) + (1-\eta)\right]}\left[\eta \cdot \sin\theta + (1-\eta)\,\theta\right] - \frac{a_t}{L} \tag{5.12}$$

Note that this equation becomes the same as the plant model in (5.2) when the plant is assumed to be linear ($\eta = 0$) and has zero damping ($\zeta = 0$).

Simulations were conducted by using the nonlinear equation of motion in (5.12) as the plant. The reference model assumed the form described by (5.1). The crane parameters listed in Table 5.1, and $\omega_m = \omega_n = 5.0$ rad/sec and $\zeta_m = 0$ were utilized for the single-pendulum models. Figure 5.3 shows the indices of the maximum control effort U_{max} and energy usage $u_{index} = \mu$ for MRC with and without input shaping; ZV-MRC and MRC respectively. The η was varied to see how the nonlinear element in the plant influences the control effort.

The figure shows that both U_{max} and u_{index} for ZV-MRC are reduced compared to MRC, especially in the energy usage. The control effort indices increase as the system

approaches full nonlinearity and exhibits more complex dynamics. ZV-MRC effectively minimizes this phenomena and maintains the flat level of U_{max} and u_{index}, while the indices in MRC continue to increase as η approaches 1. The simulation reveals that by applying input shaping to MRC, the nonlinear dynamics of the crane can be minimized and the system behaves more linearly.

5.2.4 State tracking and control effort

The state tracking performance and control effort reduction provided by ZV-MRC in the presence of plant parameter variations were investigated. Simulations were conducted for a point-to-point motion of the crane trolley, starting at $t = 1$ sec and stopping at $t = 6$ sec. The reference model was assigned the parameters of $\omega_m = 5.0$ rad/sec and $\zeta_m = 0.2$. A time-varying plant with various error values was simulated for ZV-MRC and MRC. The plant parameters $\omega_n(t)$ and $\zeta(t)$ were set to time-varying variables:

$$\begin{aligned} \omega_n(t) &= \omega_m[1 + \alpha sin(t)] \\ \zeta(t) &= \zeta_m[1 + \alpha sin(t)] \end{aligned} \tag{5.13}$$

The values of ω_m and ζ_m are taken from the reference model. The parameter variance percentage α specifies the magnitude of the parameter variation.

First, the plant states tracking performance of ZV-MRC was investigated using a high parameter variation of $\alpha = 30\%$. Figure 5.4 shows the horizontal swing distance of the payload with an unshaped (MRC) and input-shaped (ZV-MRC) step velocity command. The payload responses of both the time-varying plant and the reference model are plotted. In all cases, the desired model states are tracked nearly perfectly by the plant states, even with the high value of α (the order of the tracking error was $\sim 10^{-8}$ at the highest). The key difference in the ZV-MRC case is that the oscillation is greatly reduced by input shaping. These results indicate that MRC, when combined with an input shaper, can perform effectively without sacrificing state tracking accuracy. In addition, the controller provides near

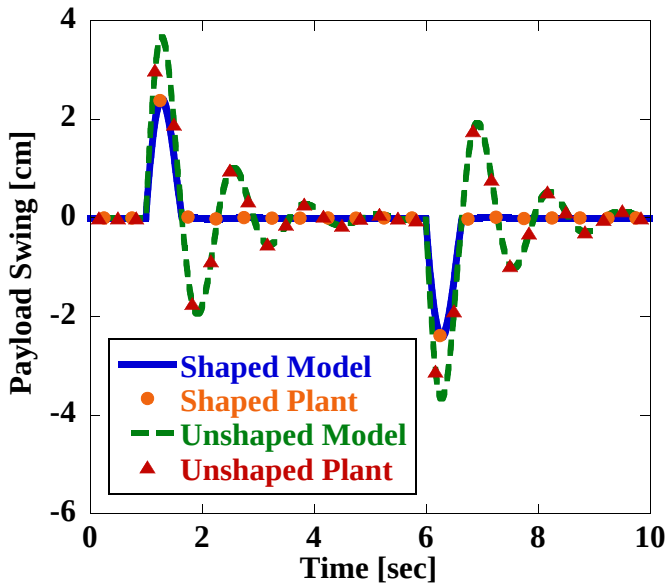

Figure 5.4: Reference model and plant payload swings in ZV-MRC and MRC

exact oscillation cancellation from the ZV shaper, even in the presence of large parameter variations in $\omega_n(t)$ and $\zeta(t)$. This result is achieved by strengthening the shaper's robustness via MRC, which forces the time-varying plant to follow the desired non-oscillatory states computed by the reference model.

Next, the control effort of the system under different parameter variances was analyzed. Figure 5.5 shows the MRC control signal u sent to the plant for parameter variances of 0.1%, 15%, and 30%. The control signal with the larger parameter variance has larger signal overshoot because more control effort is necessary to drive the plant to the same desired states. This agrees with the control law derived in (5.4) that a larger error between the model and the plant results in a larger control effort. Also, the larger variance results in a control signal with larger amplitude fluctuation, which is undesirable for reasons of actuator life-expectancy and energy consumption.

The effects of applying input shaping to the control effort was analyzed by running the same simulations with a ZV-MRC algorithm. Figure 5.6 shows the input-shaped control signals of ZV-MRC with different plant parameter variances of 0.1%, 15%, and 30%. Again, the command signal with a larger parameter variance results in a larger command

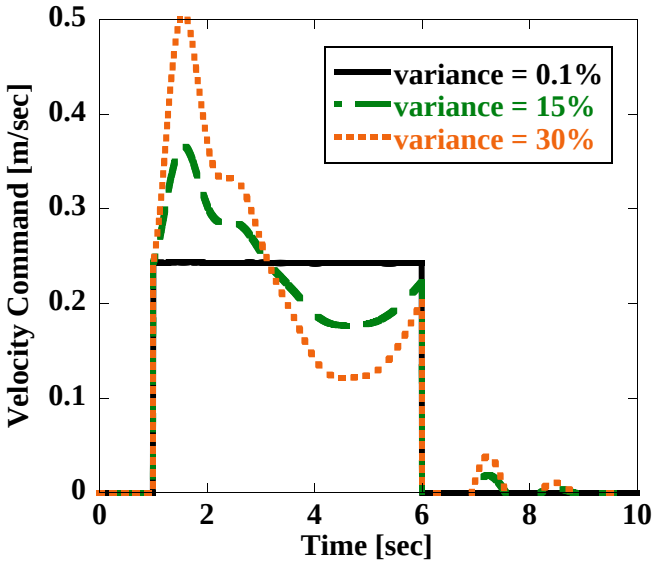

Figure 5.5: Control effort of MRC at difference parameter variances

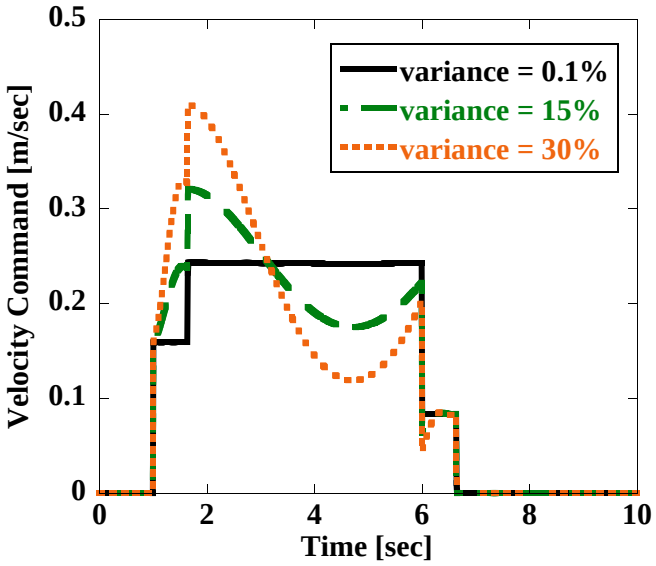

Figure 5.6: Control effort of ZV-MRC at difference parameter variances

amplitude. However, when compared to Figure 5.5, the maximum control effort magnitude has been decreased by the input shaper (by 19.0% for the $\alpha = 30\%$ case). In addition, the command signal fluctuation is reduced and results in a smoother profile. This is because the ZV shaper limited the payload oscillation, and thus, eliminated the need to cancel oscillation via the MRC algorithm.

To explore the effects of the parameter variances further, simulations with different combinations of α variances were performed. Figure 5.7 shows the maximum control effort index U_{max} of MRC as a function of different parameter variance α in ω_n and ζ. The α value ranges from 0.1% to 30%. The figure indicates that increasing the variance results in higher values of the control effort, which is expected from the nature of MRC. Larger force is necessary to drive the plant when there is a larger error between the actual plant and the reference model. The effect is more evident in the parameter variance in ω_n due to the square terms in the control law in (5.4). This suggests that obtaining a closer estimation of ω_n is more critical than obtaining a good estimate of ζ to limit the control effort increase. Also, note that the maximum control effort index always resulted in $U_{max} = 1.0$ or higher. This indicates that MRC needs to supply a control signal that is larger than the input velocity command in order to drive the time-varying plant with parameter variations.

The same simulation study was conducted for ZV-MRC. The results in Figure 5.8 show U_{max} for ZV-MRC plotted against different value of α in ω_n and ζ. The plot displays very similar trends to Figure 5.7. The maximum control effort increases from $U_{max} = 1.0$ as the parameter variances increase. The effect is more evident in the variance of ω_n. The plot also clearly illustrates the effect of applying the ZV shaper. Compared to MRC, the control effort of ZV-MRC is reduced for all combinations of ω_n and ζ variances. This shows that input shaping can help mitigate the excessive control effort due to plant parameter variations.

The effect of different natural frequency and damping ratio values on the maximum

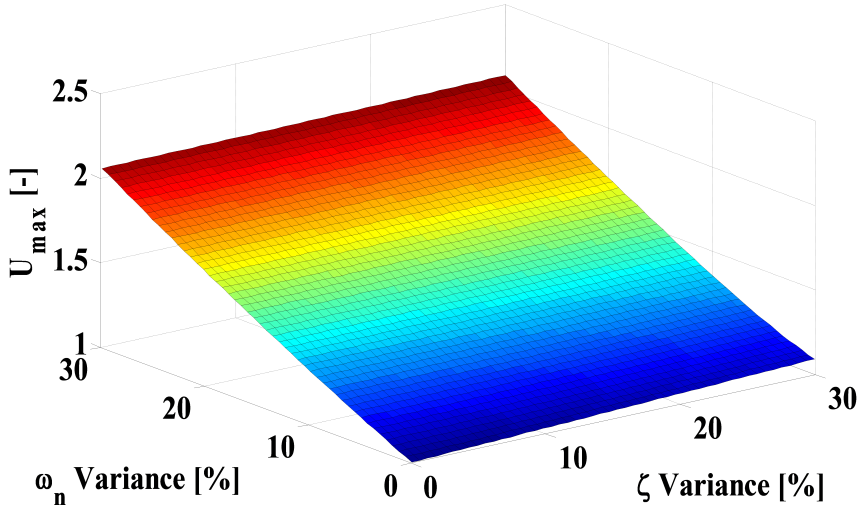

Figure 5.7: U_{max} of MRC as a function of the parameter variance α

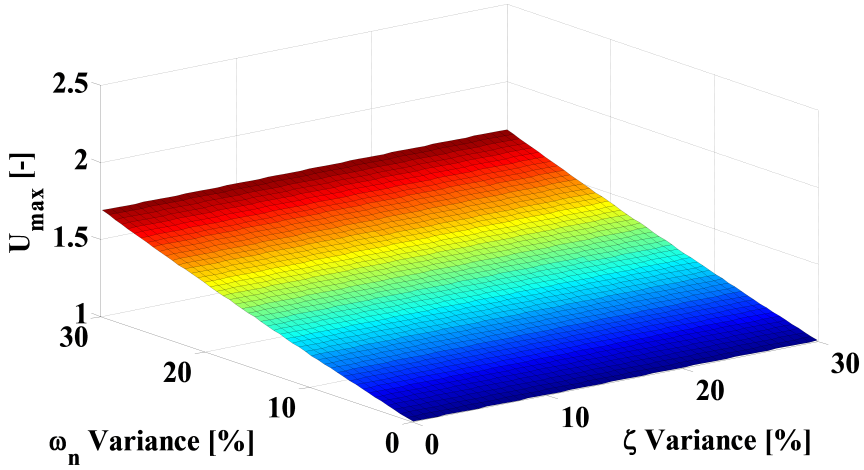

Figure 5.8: U_{max} of ZV-MRC as a function of the parameter variance α

control effort was also analyzed. Figure 5.9 shows the maximum control effort index U_{max} for MRC with different combinations of the system parameters ω_m and ζ_m. The value of ω_m ranges between $1.0 \sim 10.0$ rad/sec and ζ_m ranges between $0.0 \sim 0.4$. The parameter variance was fixed at $\alpha = 30\%$. The plot indicates that there is a slight increase in U_{max} while increasing the value of ζ_m. The value of U_{max} increases more significantly as the value of ω_m increases, especially in the range between $\omega_m = 1.0 \sim 3.0$ rad/sec. The lowest control effort value is observed at $U_{max} = 1.376$. The worst control effort case occurs when the system has a high natural frequency and a low damping ratio.

The control effort reduction of ZV-MRC was also studied for different system param-

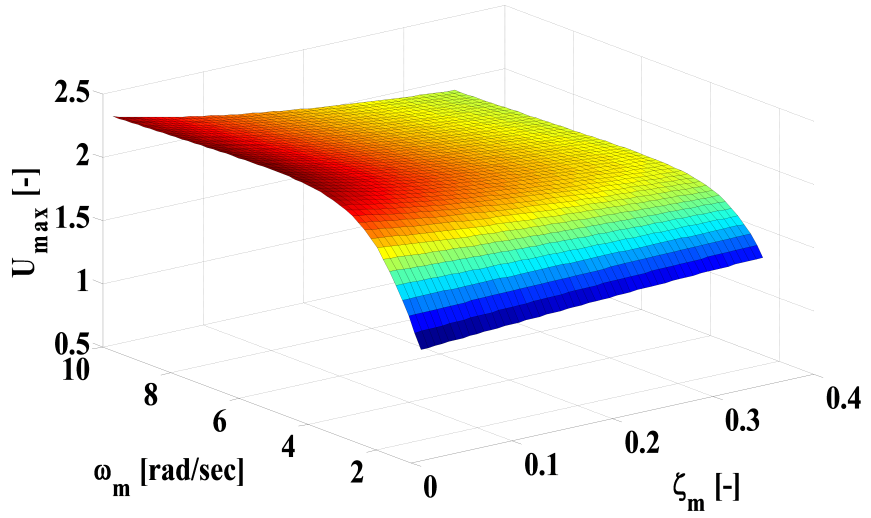

Figure 5.9: U_{max} of MRC as a function of the system parameters [$\alpha = 30\%$]

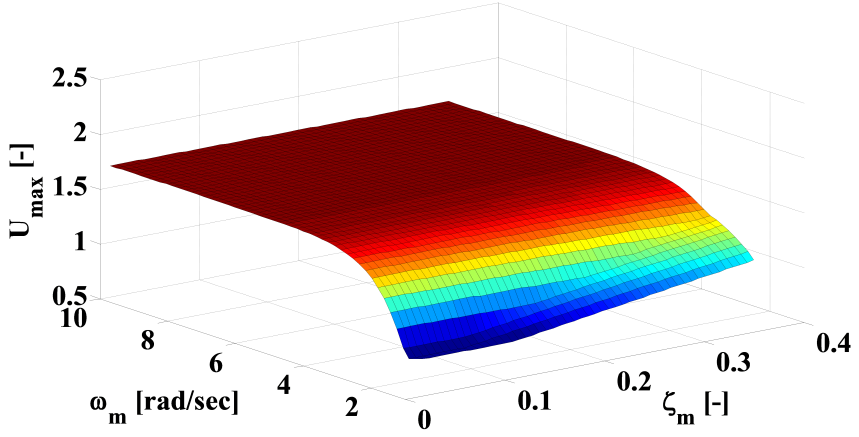

Figure 5.10: U_{max} of ZV-MRC as a function of the system parameters [$\alpha = 30\%$]

eters cases. The surface plot in Figure 5.10 shows U_{max} for ZV-MRC obtained from the same simulation scenarios as Figure 5.9. The plots display similar general characteristics, but clearly indicate some important differences due to the ZV shaper. First, the overall magnitude of U_{max} is reduced for all ranges of ω_m and ζ_m. The most notable reduction occurs at the high-frequency, low-damping region where the peak was observed in Figure 5.9. Also, the maximum control effort magnitudes level off when the natural frequency is over $\omega_m = 3.0$ rad/sec.

The control effort reduction becomes less effective when the damping ratio is increased at low natural frequencies (i.e. $\zeta_m \geqslant 0.1$). This can be explained by the ZV shaper formula

in (3.4). Higher damping ratios result in lower values of K, as shown in (3.5). This modifies the magnitudes of the ZV shaper impulses such that the magnitude of the first impulse is increased, while the second impulse is decreased. When ζ_m becomes high enough, the first impulse essentially behaves as a single impulse. Convolving a single-impulse shaper with a reference command produces no modification to the signal. As a result, the ZV shaper for high damping produces a convolved signal that is very similar to the unshaped input case. This leads to almost no reduction in the control effort overshoot. This phenomenon is observed in the low-frequency, high-damping region only because this is where the damping ratio becomes a more dominant factor in the shaper design.

Another interesting observation occurs at the low-damping, low-frequency region (i.e. $\zeta_m < 0.15$, $\omega_m < 1.5$ rad/sec). In this region, the maximum control effort is less than the magnitude of the reference command supplied, or $U_{max} < 1.0$. This indicates that less control effort magnitude is needed to control the time-varying plant using ZV-MRC. At a certain combination of the system parameters ZV-MRC has the potential to lower the necessary control effort below the reference, and thus, reduce the total energy usage. The downside, however, would be a longer ramp-up time and slower trolley speed.

5.2.5 Robustness to error

The robustness of ZV-MRC to the parameter estimation error was investigated by running simulations and experiments. Modeling errors in the natural frequency and damping ratio were introduced, and the ZV-MRC and MRC controllers were evaluated for their state tracking, oscillation suppression, and control effort reduction performances. The reference model and plant were assumed to have the form defined in (5.1) and (5.2), respectively.

First, the robustness to the parameter estimation error in ω_m was analyzed. The parameters of the plant were set to $\omega_n = 3.62$ rad/sec ($L = 0.75$ m) and $\zeta = 0$. The damping in the reference model was set to $\zeta_m = 0.15$. The natural frequency of the reference model was varied $-10\% \sim +30\%$ from the nominal value ω_n ($\omega_m = 0.9\omega_n \sim 1.3\omega_n$).

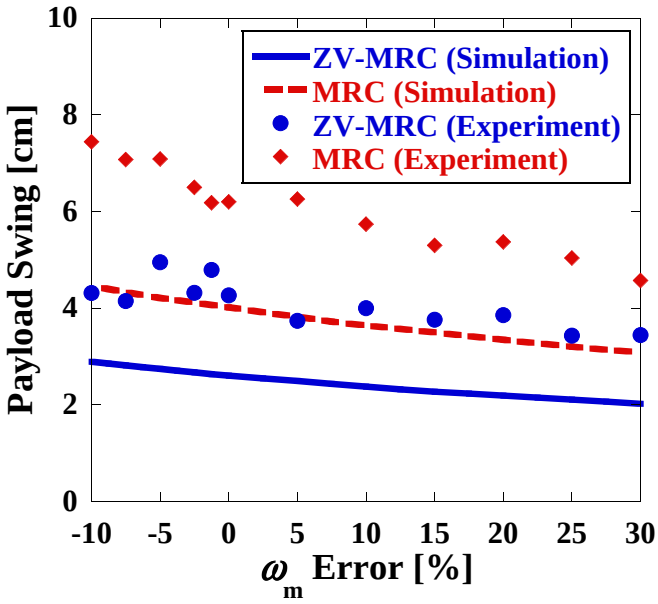

Figure 5.11: Maximum swing amplitude of ZV-MRC and MRC vs ω_m estimation error

Figure 5.11 shows the maximum swing distance of the payload, and Figure 5.12 shows the maximum residual swing of the payload. The experimental data have similar trends as the simulation results. In the figure, the swing amplitude is the highest when ω_n is under-estimated and decreases as the estimation error shifts to the over-estimation range. Also, ZV-MRC results in much lower maximum swing amplitudes than MRC for all tested cases. This is because ZV-MRC increases the speed in two steps as was shown in Figure 5.6, while the MRC ramps up immediately and induces a large oscillation. The residual swings are near zero for both controllers because MRC itself has the oscillation reduction/damping capability from non-zero ζ_m, and thus, the swings die out with time.

The state tracking performances of ZV-MRC and MRC versus ω_m estimation error are shown in Figure 5.13. The values of ε calculated from the simulation and experiment are plotted using the left and right axis, respectively. The scale of the simulation results and experimental data are found to be significantly different. This is because there are several unmodeled factors, such as the hard nonlinearities and sensor accuracy, that would negatively influence the experimental data. The simulation and experimental data, however, exhibits a similar general trend. The tracking index ε is higher when ω_n is under-estimated

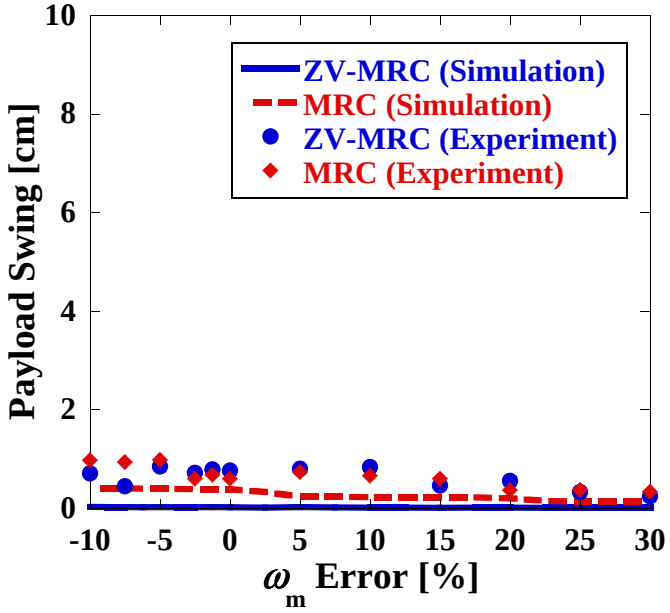

Figure 5.12: Residual swing amplitude of ZV-MRC and MRC vs ω_m estimation error

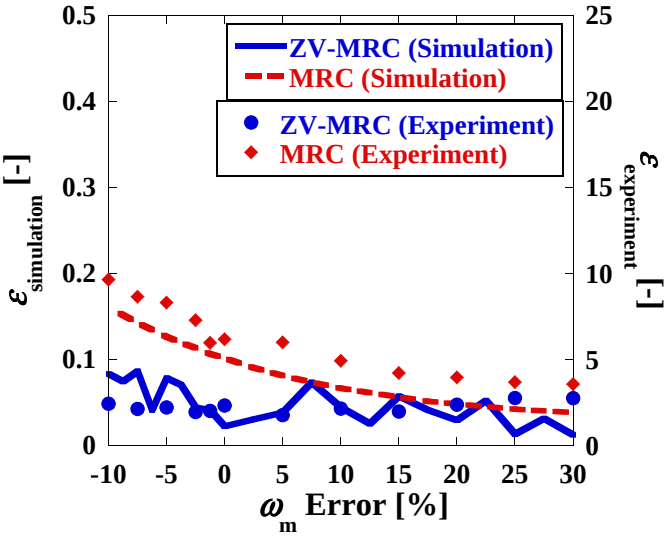

Figure 5.13: State tracking ε of ZV-MRC and MRC vs ω_m estimation error

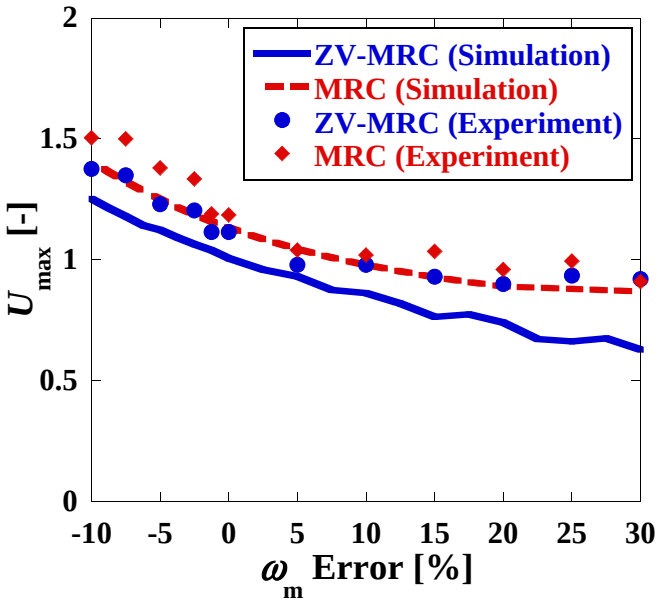

Figure 5.14: Maximum control effort U_{max} of ZV-MRC and MRC vs ω_m estimation error

and becomes lower when it is over-estimated. The trend was also observed in the maximum swing amplitude plot in Figure 5.11. The plots show a correlation because large payload swings make accurate state tracking more difficult. The ε value of ZV-MRC results in lower values than MRC because the ZV shaper limited the payload oscillation and facilitated the state tracking task.

Figure 5.14 shows the maximum control effort index U_{max} versus the ω_m estimation error, and Figure 5.15 shows the energy usage index μ versus the error. The plots show the index values for ZV-MRC and MRC obtained by running the simulations and experiments. The figures show good agreement between the simulation and experiment data. For both U_{max} and μ, the index results in a high value when ω_m is under-estimated and a low value when over-estimated.

The effect of implementing ZV-MRC is more evident in the U_{max} plot. The U_{max} values of the ZV-MRC are found to be lower than the MRC for the entire ω_m variation range. This demonstrates that the ZV shaper effectively reduces the control effort overshoot in MRC caused by the modeling error. Also, when ω_m is over-estimated, the index value becomes less than 1. This indicates that the maximum control effort resulting from ZV-MRC control

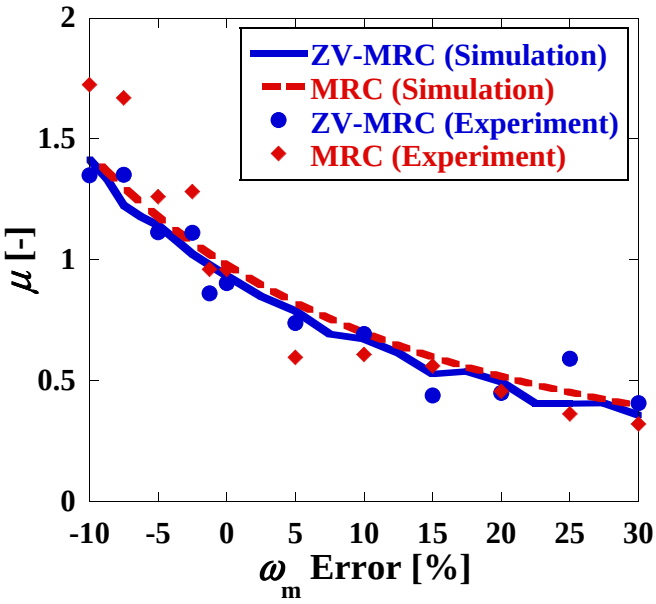

Figure 5.15: Control energy μ of ZV-MRC and MRC vs ω_m estimation error

can be lower than the magnitude of the velocity command input. In such cases, the issue of actuator saturation is resolved.

The over-estimation of ω_m, however, raises the issue of slower trolley speed. The energy index μ in Figure 5.15 gradually decreases in value and becomes less than 1 as it enters to the over-estimation range. When it reaches $+30\%$, the μ is reduced to as low as 0.5. This means that only about a half of the energy is supplied to the trolley. As a result, the trolley speed would be greatly reduced and the time required for the same trolley motion would be increased.

Also, μ does not show any clear signs of a reduction effect from applying ZV-MRC. The plot of ZV-MRC is only slightly below the MRC plot in Figure 5.15. The main reason for this is because the index was calculated by using the control effort data obtained from the entire simulation/experiment period, which consists of a short acceleration time and a much longer coasting time. The energy reduction effect of input shaping is only apparent during the acceleration phase. Thus, the reduction effect diminishes as μ includes more data from the long coasting time.

Next, the robustness to modeling differences in ζ_m was analyzed. The parameters of the

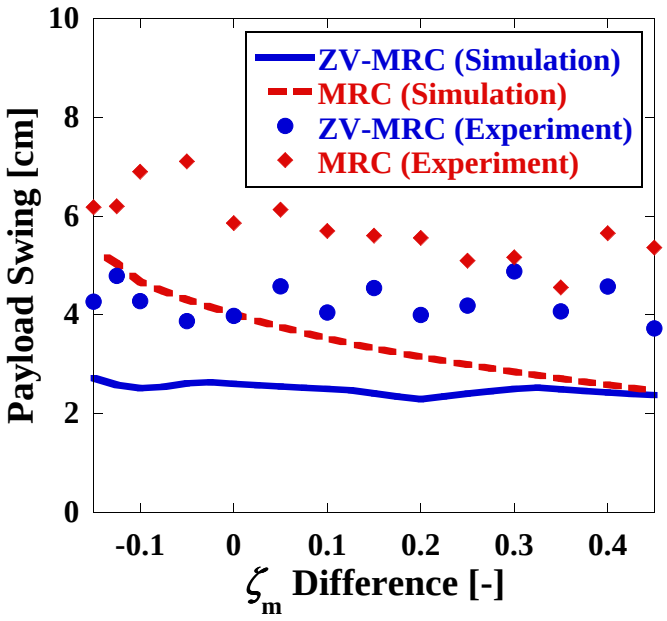

Figure 5.16: Maximum swing amplitude of ZV-MRC and MRC vs the difference in ζ_m

plant were set to $\omega_n = 3.62$ rad/sec and $\zeta = 0.15$ in the control law. The natural frequency in the reference model was set equal to that of the plant, $\omega_m = \omega_n = 3.62$ rad/sec. The damping ratio in the reference model was varied between $\zeta_m = 0 \sim 0.6$ (thus, the ζ_m difference of $-1.5 \sim +4.5$ from the plant value). Simulations were performed for the ZV-MRC and MRC controllers, and the results were validated by experimental data.

Figure 5.16 shows the maximum swing distance of the payload versus the ζ_m modeling difference. The experimental data show similar trends and generally agree with the simulation results. The maximum payload swing of MRC is influenced greatly by damping and is decreased as the value of ζ_m is increased. The maximum swing of ZV-MRC, on the other hand, remains relatively flat at the lower level for the entire range of the ζ_m difference. The ZV shaper effectively limits the payload oscillation and helps to increase the robustness of MRC.

Figure 5.17 shows residual payload swing versus the ζ_m modeling difference. The residual swing is also reduced to near zero level, except for the MRC simulation cases where ζ_m is under-estimated. In MRC, the only factor that contributes to the oscillation reduction is the damping. Thus, when the damping ratio is set low or near zero, MRC alone

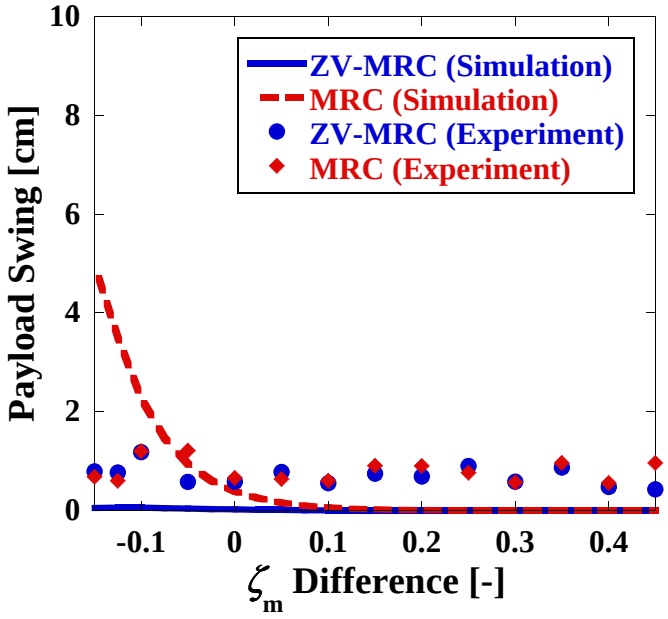

Figure 5.17: Residual swing amplitude of ZV-MRC and MRC vs the difference in ζ_m

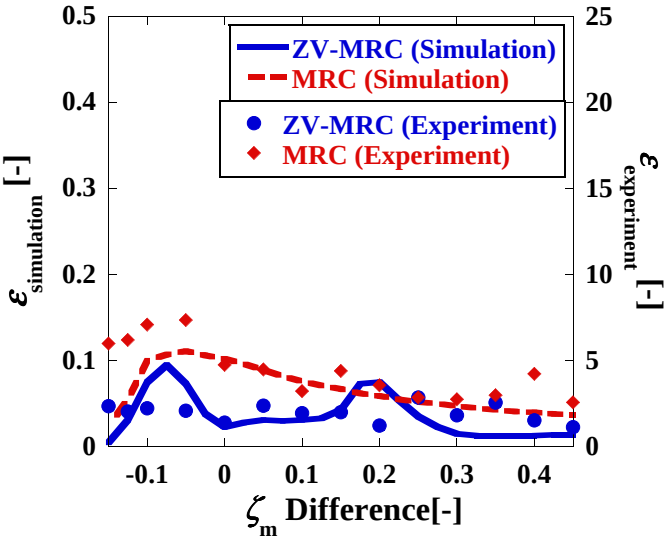

Figure 5.18: State tracking ε of ZV-MRC and MRC vs the difference in ζ_m

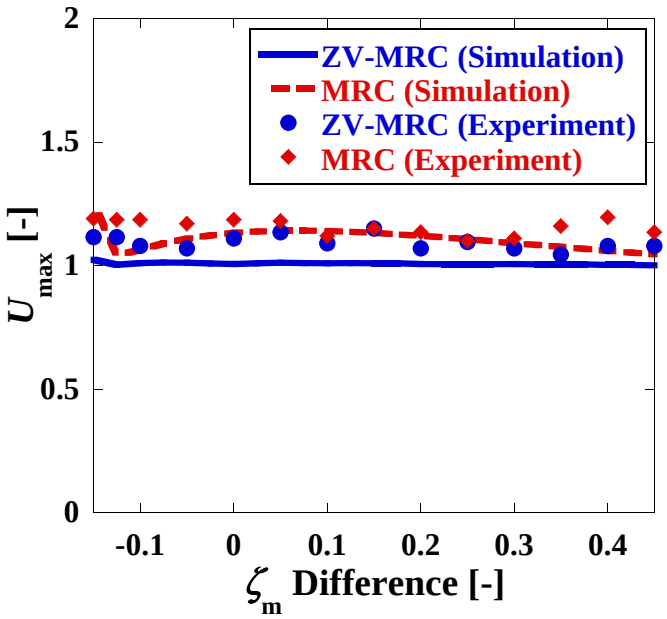

Figure 5.19: Maximum control effort U_{max} of ZV-MRC and MRC vs the difference in ζ_m

cannot reduce the payload oscillation effectively. Unlike the simulation, the experimental data of MRC shows low residual oscillation at very low values of ζ_m because there are number of factors that act as effective damping in the real crane.

The state tracking ε of ZV-MRC and MRC as a function of ζ_m modeling difference is shown in Figure 5.18. The simulation results and experimental data are plotted with the left and right axis, respectively. Again, the scale of the simulation results and experimental data are significantly different because there are several factors reducing the accuracy of the experimental data. Despite the difference in the magnitude, the simulation and experimental data exhibits a similar general trend. Similar to Figure 5.13, the ε value of MRC is higher when ζ_m is under-estimated and lower when it is over-estimated. This, again, is due to the large payload swings at a low damping that make accurate tracking difficult. The ε value of ZV-MRC remains at a low, flat level for the entire range of the ζ_m difference. The ZV-MRC effectively limits the payload oscillation and allows more accurate state tracking than MRC, even with the difference in ζ_m modeling.

Figure 5.19 shows the maximum control effort index U_{max} versus the modeling difference in ζ_m, and Figure 5.20 shows the energy usage index μ versus the modeling difference.

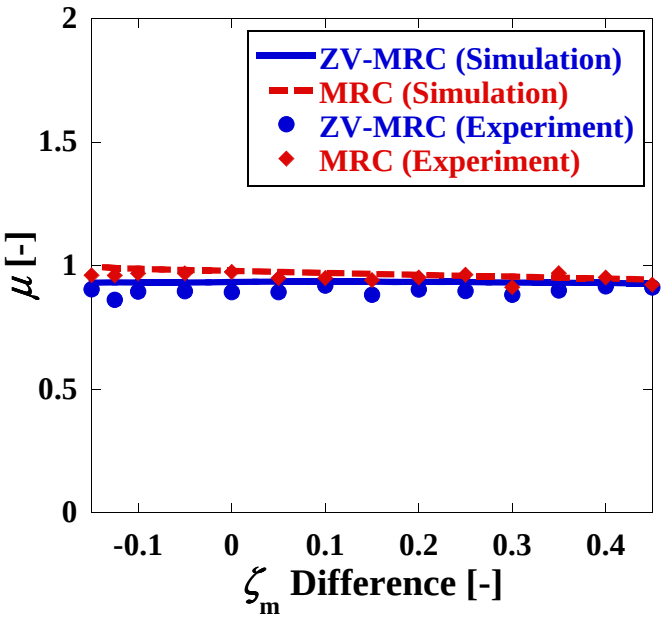

Figure 5.20: Control energy μ of ZV-MRC and MRC vs the difference in ζ_m

The plots show the index values for ZV-MRC and MRC obtained by running the simulations and performing experiments. The figures show a good agreement between the simulation and experiment data. Although the ZV-MRC demonstrated a small improvement, the plot lines remained nearly flat; the ZV-MRC maintained the U_{max} magnitudes around 1 and the μ values slightly under 1 for a wide range of ζ_m. The difference in ζ_m had only a minor influence on the control effort compared to the ω_m, as shown in Figure 5.9 and Figure 5.10. The ZV-MRC further minimized the variation in U_{max} and μ by integrating the ZV shaper. Therefore, when designing a MRC controller, it is more important to obtain an accurate value of the crane's natural frequency than the damping of the payload swing.

5.3 Summary

In this chapter, the proposed control method of input-shaped model reference control was explained. The ZV-MRC controller design that combines a ZV shaper and model reference control was investigated on a crane with a single-pendulum payload. The ZV-MRC design was explored by determining the reference model and plant parameters, deriving the

expression of Lyapunov control law, and obtaining a Zero-Vibration input shaper design.

The control signal expression suggested that a larger error between the model and the plant results in a larger control signal overshoot because more control effort is necessary to drive the plant to the same desired states. The effect was more evident in the parameter variance in ω_n due to the squared terms in the control law.

The proposed ZV-MRC performance was analyzed using numerical simulations of a planar crane and experiments on a small-scale bridge crane. The performance indices were defined to quantify and compare the effectiveness of ZV-MRC and MRC in state tracking, oscillation suppression, and control effort reduction.

The ZV-MRC design was found to be robust to modeling errors in both ω_n and ζ. It outperformed the MRC in all aspects of functionality without sacrificing state tracking accuracy. The ZV-MRC controller resulted in much lower maximum swing amplitudes than MRC and provided near exact oscillation cancellation. The ε values were also lowered because the ZV shaper limited the payload oscillation and facilitated the state tracking task.

It was found that input shaping can help mitigate the excessive control effort by limiting the payload oscillation. The ZV-MRC linearized the plant dynamics and reduced the control effort of MRC even when the parameters had large estimation errors and value variations. The ZV shaper effectively reduced the U_{max} values in MRC caused by ω_n and ζ variances, without sacrificing the oscillation suppression and state tracking capabilities. In some cases, the index value became less than 1.0 and prevented the possibility of actuator saturation. In addition, the control signal fluctuation was reduced and resulted in a smoother profile.

However, the ZV-MRC design also had some drawbacks. The control effort reduction performance became less effective when ζ_m was set high. The trolley speed was also decreased, and caused a delay in ramp-up time and motion completion. Also, the trolley energy input μ might not be reduced significantly for some application by applying ZV-MRC. This is because input shaping reduces the input energy only during the acceleration

phase. These issues will be addressed later in the thesis when designing an optimized input-shaping model reference controller.

CHAPTER 6

IS-MRC ON A DOUBLE-PENDULUM PAYLOAD

CHAPTER SUMMARY:

This chapter will explain the IS-MRC design for a crane with a double-pendulum payload. Section 6.1 presents the IS-MRC controller designed for a double-pendulum crane. The reference model and estimated plant are designed and utilized to obtain the control signal expression. The oscillation frequency ranges are calculated and used to obtain multi-mode input shaper designs. In Section 6.2, the performances of the proposed IS-MRC designs are evaluated by numerical simulations and verified by experiments. The state tracking, oscillation suppression, and control effort reduction performances against plant estimation errors are analyzed.

The IS-MRC design has shown effective in controlling a crane with a single-pendulum payload with large parameter variations in Chapter 5. However, the representative plants were assumed to have full description on the plant dynamics. In addition, a linearized time-invariant model was utilized to represent the actual plant. These assumptions are not always true as actual nonlinear systems can be difficult to model and/or uncertain. Other non-parametric uncertainties, such as measurement noise, disturbances, computation round-off errors, and sampling delays also negatively impact the IS-MRC's performance. Another major factor when controlling flexible systems is the so-called spill over effect. This is the impact of uncertain and unmodeled dynamics, such as Coulomb friction and centrifugal acceleration, which may pose a major challenge on the stability. The absence of accurate plant representation could lead to performance degradation, instability, and sudden failure of the system. Therefore, the robustness of IS-MRC needs to be enforced to handle these unpredictable uncertainties.

In this chapter, the work is extended to controlling an uncertain, nonlinear crane with a double-pendulum payload. Double-pendulum payloads constitute a critical subset of crane applications. In the crane control, certain types of payload and rigging can induce double-pendulum effects that increase the complexity of the control problem by producing a two-mode oscillatory system. In addition, obtaining accurate real-time measurement of a second payload mass is extremely difficult by sensors.

The IS-MRC aims to solve this control problem by further increasing the controller's robustness to plant parameter variations and handle larger system uncertainty. To be specific, a nonlinear double-pendulum crane (4^{th}-order system) will be driven via a IS-MRC using a linear single-pendulum reference model (2^{nd}-order system) and a robust input shaper that suppresses the payload oscillations and linearizes the system dynamics. This chapter discusses various IS-MRC designs for a double-pendulum crane described in Section 2.2 and analyzes them for state tracking, oscillation reduction, and control effort reduction performances against plant estimation errors.

6.1 IS-MRC Design for Double-Pendulum Crane

In this work, the uncertain plant considered is a nonlinear double-pendulum crane; however, a linearized single-pendulum crane is used as a reference model in the MRC scheme. The reason for utilizing the one-mode reference model is because 1) it is easier to implement, and 2) accurate real-time measurement of the second mode of a real crane is extremely difficult. Furthermore, a single-pendulum is a very good representation of a crane when it does not carry a payload.

6.1.1 Reference Model and Plant

The reference model is a linearized single-pendulum payload that has the same state space representation from (5.1). The state equation matrices are defined as $\mathbf{A_{SP}}$ and $\mathbf{B_{SP}}$, with the natural frequency ω_m and damping ratio ζ_m. These model parameters can be specified

based on the design requirements.

The nonlinear equations of motion in (2.6) and (2.7) are utilized to simulate the actual double-pendulum plant dynamics. However, the nonlinear expressions are ill-suited for the derivation method of the control law. Thus, a simplified linear model of the estimated plant is formulated.

The linearized state equation of a double-pendulum payload in (2.10) is used to represent the estimated plant model that is necessary for the control law. In order to implement MRC, the actual plant state vector that is feedbacked to the control law block need to have the same form as the reference model state vector. To be specific, $\mathbf{x}$ and $\mathbf{x_d}$ must have the same number of rows and describe the similar physical definition of the system. Double-pendulum crane is a two-mode system that has four associated states (two states for the hook and payload respectively). However, because only the states x_1 and x_2 associated with the first mode of the double-pendulum crane are available, the corresponding segment of (2.10) is utilized. Also, because the actual plant parameters and dynamics are uncertain, the median value of the possible hoisting range $L_{1,med}$ is chosen as the representative value of the unknown cable length:

$$\begin{aligned} \dot{\mathbf{x}} &= \mathbf{A_{DP}}\mathbf{x} + \mathbf{B_{DP}}u \\ = \begin{bmatrix} \dot{x_1} \\ \dot{x_2} \\ - \\ - \end{bmatrix} &= \begin{bmatrix} 0 & 1 & - & - \\ -\frac{g}{L_{1,med}} & 0 & - & - \\ - & - & - & - \\ - & - & - & - \end{bmatrix} \begin{bmatrix} x_1 \\ x_2 \\ - \\ - \end{bmatrix} + \begin{bmatrix} 0 \\ 1 \\ - \\ - \end{bmatrix} u \end{aligned} \tag{6.1}$$

where, $\mathbf{A_{DP}}$ and $\mathbf{B_{DP}}$ are the estimated state equation matrices of the plant. The natural frequency of the estimated plant is $\omega_n = \sqrt{g/L_{1,med}}$.

6.1.2 Control Law

The second method of Lyapunov is applied to formulate the control law that generates the control signal u. Given the system order difference between the single-pendulum reference model and the double-pendulum plant, only the first-mode states of the plant, x_1 and x_2, are used for the control law. This makes the time derivative of the error signal as:

$$\dot{\mathbf{e}} = \dot{\mathbf{x_d}} - \dot{\mathbf{x}} = (\mathbf{A_{SP}x_d} + \mathbf{B_{SP}}v) - (\mathbf{A_{DP}x} + \mathbf{B_{DP}}u) \tag{6.2}$$

Following similar derivation steps discussed in the single-pendulum crane case in Chapter 5, the control law expression yields:

$$u = \frac{\mathbf{e}^T\mathbf{PA_{SP}x} - \mathbf{e}^T\mathbf{PA_{DP}x} + \mathbf{e}^T\mathbf{PB_{SP}}v + \lambda}{\mathbf{e}^T\mathbf{PB_{DP}}} \tag{6.3}$$

The equations from (5.1), (6.1), and (6.2) are substituted. The arbitrary scalar constant λ is again set to $\lambda = (e_1P_{1,2} + e_2P_{2,2})^2$ to make IS-MRC controller asymptotically stable. Then, the control signal u becomes:

$$u = (-\omega_m^2 + g/L_{1,med})x_1 + (-2\zeta_m\omega_m)x_2 + v + \Lambda \tag{6.4}$$

where, Λ term is defined in (5.5).

Similar to (5.4), the expression for u takes into account both the parameter modeling errors and the state tracking errors. The plant parameter estimation of $L_{1,med}$ becomes more significant as it is the only plant parameter directly contributing to the control signal. In addition, it influences the error in the natural frequency that is expected to exhibit more effects than the damping ratio because of the squared term.

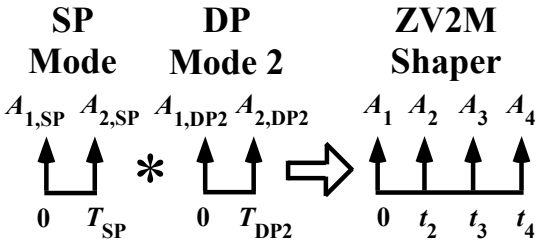

Figure 6.1: ZV2M shaper design by convolving two ZV shapers

6.1.3 Multi-Mode Input Shaper Designs

The ZV shaper from Section 3.1 is only designed to eliminate a single mode of vibration. When the shaper is applied to a multiple DOF system oscillating with multiple modes, its vibration reduction effectiveness can be degraded significantly. To address this issue, shaper designs targeting multiple modes of oscillation were developed. In this work, a *Two-Mode Zero-Vibration* (ZV2M) shaper, a *Three-Mode Zero-Vibration* (ZV3M) shaper, and a *Two-Mode Specified Insensitivity* (SI2M) shaper are applied to suppress the oscillations of the double-pendulum crane. Because they are combined with the MRC scheme, the proposed controller designs are referred as ZV-MRC, ZV2M-MRC, ZV3M-MRC, and SI2M-MRC respectively [176].

A ZV2M and ZV3M shapers are obtained by convolving separate ZV shapers, one for each target mode, into one single shaper. Figure 6.1 shows the conceptual illustration of the design process of a ZV2M shaper and Figure 6.2 shows the process of a ZV3M shaper. In this work, the ZV2M shaper is designed to eliminate the vibratory mode in the single-pendulum reference model and the second vibratory mode in the double-pendulum plant. The ZV3M is designed for the vibratory mode in the single-pendulum reference model, plus both the first and second vibratory modes in the double-pendulum plant.

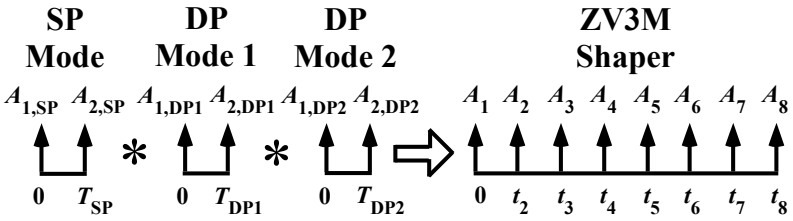

Figure 6.2: ZV3M shaper design by convolving three ZV shapers

The ZV2M and ZV3M shapers are:

$$\begin{bmatrix} A_i & t_i \end{bmatrix}_{ZV2M} = \begin{bmatrix} A_{1,SP} \times A_{1,DP2} & 0 \\ A_{1,SP} \times A_{2,DP2} & T_{DP2} \\ A_{2,SP} \times A_{1,DP2} & T_{SP} \\ A_{2,SP} \times A_{2,DP2} & T_{SP} + T_{DP2} \end{bmatrix} \tag{6.5}$$

$$\begin{bmatrix} A_i & t_i \end{bmatrix}_{ZV3M} = \begin{bmatrix} A_{1,SP} \times A_{1,DP1} \times A_{1,DP2} & 0 \\ A_{1,SP} \times A_{1,DP1} \times A_{2,DP2} & T_{DP2} \\ A_{1,SP} \times A_{2,DP1} \times A_{1,DP2} & T_{DP1} \\ A_{2,SP} \times A_{1,DP1} \times A_{1,DP2} & T_{SP} \\ A_{1,SP} \times A_{2,DP1} \times A_{2,DP2} & T_{DP1} + T_{DP2} \\ A_{2,SP} \times A_{1,DP1} \times A_{2,DP2} & T_{SP} + T_{DP2} \\ A_{2,SP} \times A_{2,DP1} \times A_{1,DP2} & T_{SP} + T_{DP1} \\ A_{2,SP} \times A_{2,DP1} \times A_{2,DP2} & T_{SP} + T_{DP1} + T_{DP2} \end{bmatrix} \tag{6.6}$$

where, $A_{i,mode}$ and T_{mode} correspond to the amplitudes and the timing of the ZV shapers designed for the respective modes. More details on design constraints and derivation process can be found for ZV2M in [177] and ZV3M in [178].

A SI2M shaper is the most insensitive to parameter uncertainty and variation, and is obtained through an optimization. In order to determine the SI2M shaper, a set of constraint equations must be formulated and satisfied. The first design constraint is a residual vibration amplitude limit. The maximum residual vibration amplitude after applying input shaping needs to be limited under the tolerable level. The *PRV* expression in (3.1) is used to limit the vibration of both frequency modes (ω_1 and ω_2) in the double-pendulum crane. The residual vibration at each frequency is set below a tolerable level V_{tol}:

$$V\left(\omega_1, \zeta_1\right) \leqslant V_{tol} \ , \quad V\left(\omega_2, \zeta_2\right) \leqslant V_{tol} \tag{6.7}$$

To ensure the oscillations remain small over a range of frequencies, the vibration suppression constraint above is enforced at several points near the target frequencies. This approach specifies the frequency range over which the vibration is suppressed (i.e. frequency range for both the first and second modes of double-pendulum crane).

Constraints must also be enforced on the shaper's impulse amplitudes. In this work, only positive-impulse shapers are considered and thus the impulse amplitudes are constrained to be positive:

$$A_i > 0 \ , \quad for \ \ i = 1, \cdots, n \tag{6.8}$$

where, n is the total number of impulses in the shaper.

The shaped reference command must reach the desired final state. So, the impulse amplitudes are constrained to sum to one:

$$\sum_{i=1}^{n} A_i = 1 \tag{6.9}$$

Due to the transcendental nature of the residual oscillation equations, there are an infinite number of solutions. To select the optimal solution which has the shortest rise time

Table 6.1: Small-scale bridge crane full specifications

v_{max}	0.20 m/sec		m_1	0.69 kg
a	1.00 m/sec^2		$(m_1 + m_2)_{max}$	5.00 kg
$\dot{L}_1$	0.16 m/sec		$(L_1 + L_2)_{max}$	1.50 m

and shaper duration, the time location of the final shaper impulse is minimized:

$$\min(t_n) \tag{6.10}$$

The SI2M shaper for this paper was obtained using the *fmincon* function of the MATLAB optimization toolbox. The full details on design constraints and derivation process for SI2M shaping is addressed in [105].

6.1.4 Natural Frequency Analysis

Input shapers are designed by specifying the vibration frequencies to suppress. Hence, the hook and the payload oscillation modes are analyzed to determine the appropriate frequency ranges that the shapers must suppress.

The natural frequency analysis was conducted for the small-scale bridge crane shown in Figure 5.2. To form a double-pendulum payload, the cable carries a hook mass and a payload connected via a rigging cable. The additional specifications of the crane were listed in Table 6.1. Because the real-time measurement of the payload states is very challenging, the experimental data of the payload swing were obtained by image processing of video clips taken from outside the crane apparatus. Figure 6.3 shows an example of the video image. The colored markers attached to the trolley, hook, and payload are tracked to obtain the position data.

The oscillation frequencies of a double-pendulum depend on the suspension and rigging cable lengths, and the hook and payload masses. Because the frequency range of the system can vary widely, it is important to determine what frequencies cause the problematic

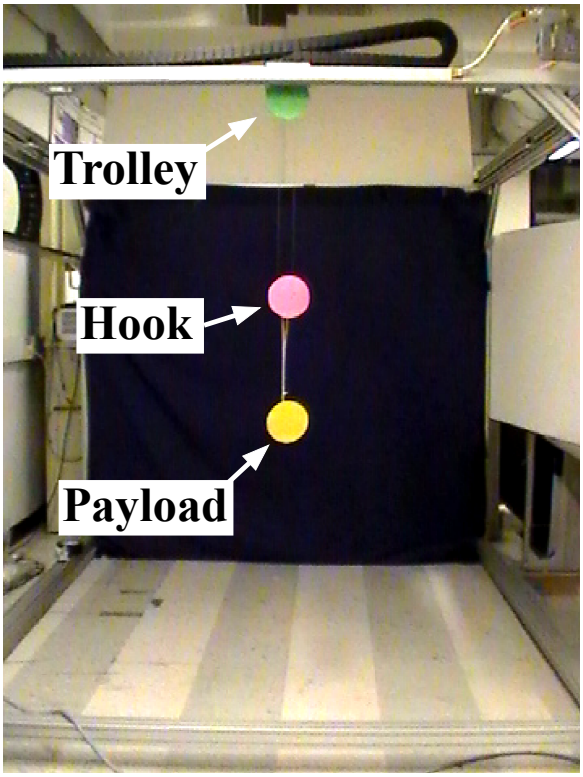

Figure 6.3: Double-pendulum crane with markers for image processing

oscillations that need to be suppressed. Assuming small swing angles and a constant hoist cable length ($\dot{L}_1 = \ddot{L}_1 = 0$), the linearized natural frequencies of the double-pendulum crane are [179]:

$$\begin{aligned} \omega_{1,2} &= \sqrt{\frac{g}{2}}\sqrt{(1+R_M)\left(\frac{1}{L_1}+\frac{1}{L_2}\right) \mp \beta} \\ \beta &= \sqrt{(1+R_M)^2\left(\frac{1}{L_1}+\frac{1}{L_2}\right)^2 - 4\left(\frac{1+R_M}{L_1 L_2}\right)} \end{aligned} \tag{6.11}$$

To determine the actual frequency value ranges, the geometric constraints and parameters of the experimental bridge crane apparatus were utilized. Figure 6.4 shows the first-mode frequency ω_1 as a function of the mass ratio $R_M = m_2/m_1$ and the cable length ratio $R_L = L_2/L_1$. The frequency decreases with an increase in R_L because a higher value of the ratio means a longer L_2, thus the second-mode oscillation becomes more significant. Similarly, the frequency also decreases with an increase in R_M. The value of ω_1 ranges

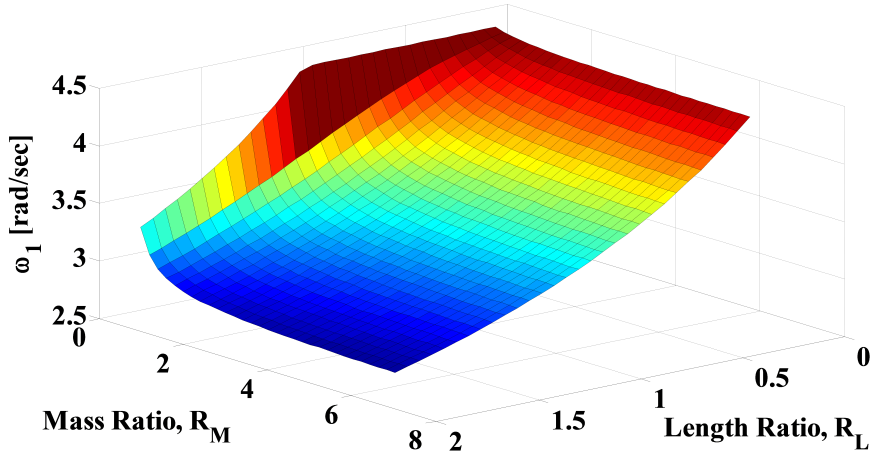

Figure 6.4: ω_1 as a function of mass ratio and length ratio

between the minimum of 2.61 rad/sec, and the maximum of 4.32 rad/sec. The maximum frequency mode roughly corresponds to the no payload $R_M = m_2 = 0$ case where the double-pendulum crane essentially acts as a single-pendulum. The range gives an overall variation of $\pm 24.7\%$ about the median value of 3.47 rad/sec.

The oscillation amplitude of the second mode compared to the first mode can be very small, or even negligible, at certain parameter settings. To obtain the practical range of ω_2 that needs to be suppressed, the relative swing contribution of the two modes is examined by breaking the overall dynamic response into ω_1 and ω_2 components. The linearized horizontal swing of the payload to an impulse can be approximated as [105]:

$$x(t) = C_1 \sin(\omega_1 t + \psi_1) + C_2 \sin(\omega_2 t + \psi_2) \tag{6.12}$$

where,

$$\begin{aligned} C_1 &= \frac{\omega_1 L_1 \left(1 + \omega_2^2 \alpha (L_1 + L_2)\right)}{k} \\ C_2 &= \frac{-\omega_2 L_1 \left(1 + \omega_1^2 \alpha (L_1 + L_2)\right)}{k} \\ \alpha &= \frac{-g\left(1 + R_M\right)}{\omega_1^2 \omega_2^2 L_1 L_2}, \qquad k = \beta L_1 g \end{aligned} \tag{6.13}$$

Here, the coefficients C_1 and C_2 represent the contributions of each mode to the overall

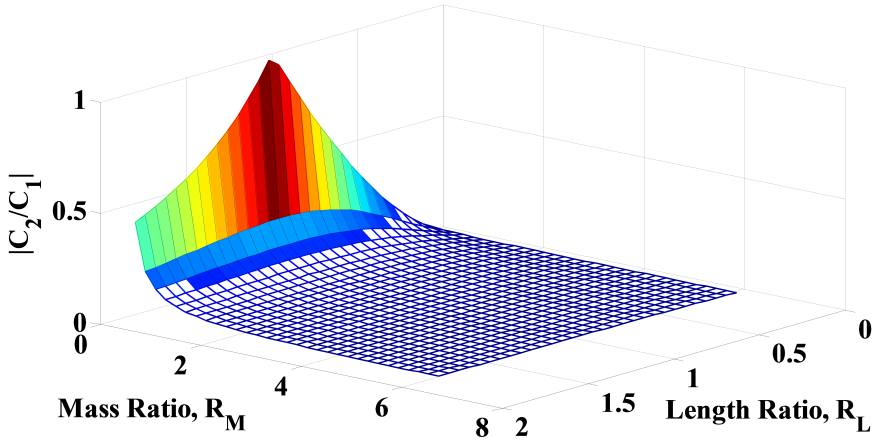

Figure 6.5: Amplitude ratio as a function of mass ratio and length ratio

payload oscillation.

The ranges of R_M and R_L when the second-mode oscillation C_2 becomes significant compared to the first-mode oscillation C_1 are found by calculating the ratio C_2/C_1. Figure 6.5 shows this ratio as a function of R_M and R_L. The plot indicates that the amplitude ratio decreases as R_M becomes larger. This is because at larger R_M the payload oscillates at higher frequencies, which means the swing amplitude becomes smaller. The maximum is observed when $R_M = 0$ and $R_L = 1.0$. By cutting off regions where the plot results in $C_2/C_1 \geqslant 10\%$, the parameter ranges of $0 \leqslant R_M \leqslant 0.69$ and $0.23 \leqslant R_L \leqslant 1.84$ are obtained. The significant region of $C_2/C_1 \geqslant 10\%$ and cutoff region are represented as solid and mesh surfaces respectively on Figure 6.5.

Figure 6.6 shows the second-mode frequency ω_2 as a function of R_M and R_L utilizing the same parameter settings as in Figure 6.4. The significant region and cutoff region that correspond to the C_2/C_1 ratio are represented as solid and mesh surfaces respectively. The frequency increases with a decrease in R_L and an increase in R_M. Using the above R_M and R_L ranges found from the C_2/C_1 ratio analysis, the frequency range that produces problematic second-mode oscillation is found to be 4.32 rad/sec $\leqslant \omega_2 \leqslant 8.98$ rad/sec. This is a $\pm 35.0\%$ variation about the median value of 6.65 rad/sec.

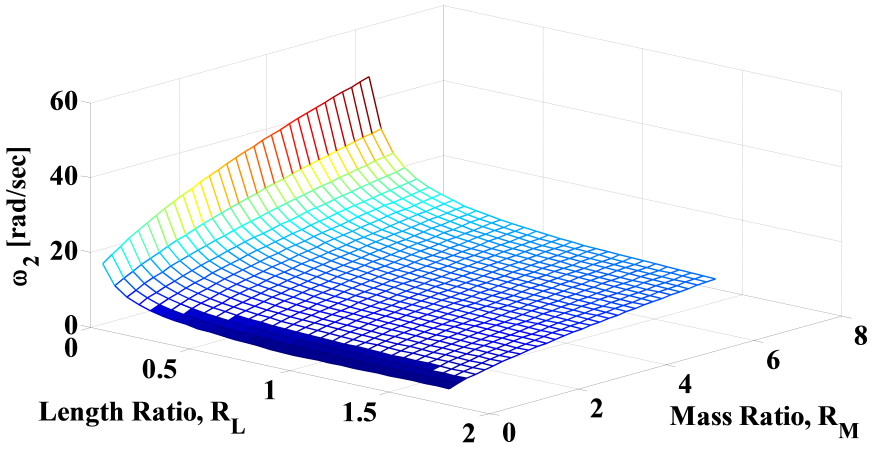

Figure 6.6: ω_2 as a function of mass ratio and length ratio

6.1.5 Parameter Assignment

The IS-MRC controllers were designed by assigning the parameter values to the reference model and the estimated plant model, as well as specifying the target frequency of the input shaper. In this section, the parameters $L_{1,med}$, ω_m, ζ_m, and target frequencies of ZV, ZV2M, ZV3M, and SI2M shapers are determined.

First, the cable length of the estimated plant described in (6.1) was assigned. Because the actual nonlinear plant remains uncertain, a representative value that best estimates the plant's general state must be selected. The median value of the possible hoisting range $L_{1,med} = 0.75$ m ($\omega_n = 3.62$ rad/sec) was chosen based on the geometric constraints in Table 6.1.

The reference model parameters ω_m and ζ_m were assigned based on the estimated plant model. Because the actual plant frequencies remain unknown during the controller design process, the value of ω_m is selected based on the possible ω_1 range found in Section 6.1.4. To minimize the control effort magnification resulting from the modeling error, ω_m needs to be close to the actual ω_1 value. Thus, the damped natural frequency of the reference model was set to the median of the possible ω_1 range, $\omega_{d,m} = 3.47$ rad/sec. Then, ω_m is found by $\omega_{d,m} = \omega_m\sqrt{1-\zeta_m^2}$.

The ζ_m value is determined from the desired percentage overshoot:

$$Mp = exp\left(-\zeta_m \pi / \sqrt{1-\zeta_m^2}\right) \tag{6.14}$$

Limited oscillation in the reference response is necessary in order to reduce the complexity of the state dynamics, which also helps reduce the MRC control effort. In this study, $Mp = 30\%$ ($\zeta_m = 0.36$) was selected to avoid actuator saturation in the experimental setup.

Based on the design parameters assigned above, the MRC control matrices $\mathbf{A_{SP}}$, $\mathbf{P}$, and $\mathbf{A_{DP}}$ were determined:

$$\mathbf{A_{SP}} = \begin{bmatrix} 0 & 1 \\ -13.79 & -2.66 \end{bmatrix} \qquad \mathbf{P} = \begin{bmatrix} 2.878 & 0.036 \\ 0.036 & 0.202 \end{bmatrix} \tag{6.15}$$

$$\mathbf{A_{DP}} = \begin{bmatrix} 0 & 1 \\ -13.08 & 0 \end{bmatrix} \tag{6.16}$$

The values of the different input shaper designs discussed in Section 6.1.3 were obtained by specifying the target frequencies. Table 6.2 summarizes the design parameters utilized in each input shaper. The ZV shaper only limited the oscillation predicted from the single-pendulum reference model described by ω_m and ζ_m. The ZV2M shaper handled both the reference model mode plus the second-mode oscillation in the uncertain double-pendulum plant. The median value of the possible ω_2 range $\omega_{2,med} = 6.65$ rad/sec was used as the representative value. The ZV3M shaper reinforced the ZV2M shaper by including $\omega_{1,med}$. The SI2M shaper was designed to suppress each frequency range, $\omega_{1,rng}$ and $\omega_{2,rng}$, discussed in Section 6.1.4 to below the tolerable vibration level of 5%. In all shaper designs, the damping ratios in the double-pendulum crane were assumed zero. The numerical values of times t_i and the amplitudes A_i of the shapers are presented in Table 6.3.

The theoretical effectiveness of input shapers are analyzed by plotting their expected

Table 6.2: Design parameters of the input shapers

Shaper	Target ω			Target ζ		
ZV	ω_m			ζ_m		
ZV2M	ω_m	$\omega_{2,med}$		ζ_m	0	
ZV3M	ω_m	$\omega_{2,med}$	$\omega_{1,med}$	ζ_m	0	0
SI2M		$\omega_{2,rng}$	$\omega_{1,rng}$		0	0

Table 6.3: Impulse amplitudes and timings of the input shapers

ZV						
t_i [ms]	0	906				
A_i [%]	77	23				
ZV2M						
t_i [ms]	0	472	906	1378		
A_i [%]	38	38	12	12		
ZV3M						
t_i [ms]	0	472	906	1378	18125	2284
A_i [%]	19	19	25	25	6	6
SI2M						
t_i [ms]	0	519	1038	1558	2078	2598
A_i [%]	9	17	24	24	17	9

vibration reduction percentage against the oscillation frequency. Figure 6.7 shows the sensitivity curves of the input shapers designed for this work. The curves illustrate the shapers' robustness to the estimation error in the natural frequency of the system [94]. The horizontal axis shows the natural frequency in rad/sec and the vertical axis shows the PRV. The ZV shaper only eliminates the oscillation at ω_m and ζ_m. Thus, as the actual frequencies deviate from the target frequency, the system vibration increases rapidly [95]. The ZV2M shaper improves the oscillation reduction by including $\omega_{2,med}$, but cannot suppress the system vibration effectively as the natural frequency deviates significantly from the designed frequency values. The ZV3M and SI2M shapers have larger robustness to natural frequency errors. Both shapers limit the vibration under the tolerable level for the $\omega_{1,rng}$ and $\omega_{2,rng}$ ranges specified for the double-pendulum plant. However, the sensitivity curves indicate that the SI2M slightly outperforms the ZV3M in the oscillations at the higher frequency.

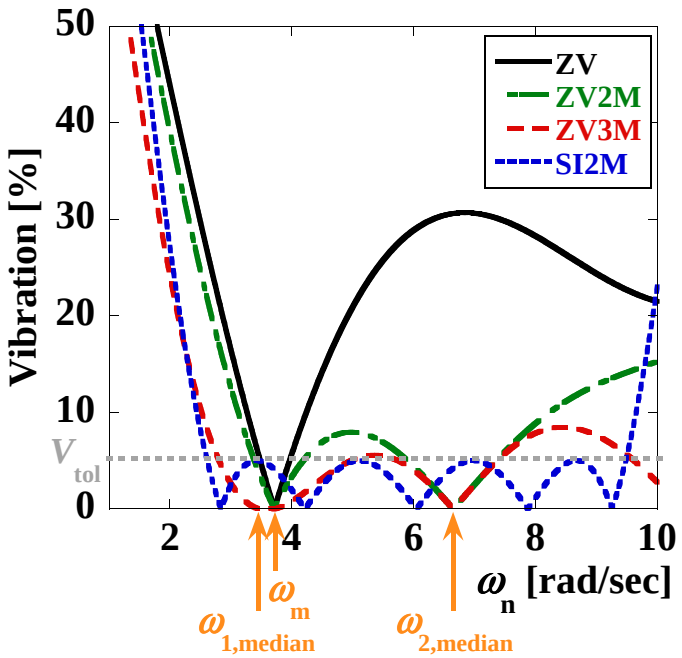

Figure 6.7: Sensitivity curves of the input shapers

6.2 Performance Verification

Numerical simulations and experimental data are used to compare and analyze the various IS-MRC controller designs. The ZV-MRC, ZV2M-MRC, ZV3M-MRC, and SI2M-MRC derived are compared in terms of state tracking, oscillation suppression, and control effort reduction performances. The controllers' robustness to the estimation error between the plant representation and the actual plant is investigated.

6.2.1 Performance Indices

In addition to the indices ε, μ, and $_{max}$ introduced in Section 5.2.2, new performance indices were defined to quantify and compare the IS-MRC controllers' performances. The hook and the payload oscillation reduction are very important factors for consideration. The maximum swing amplitudes of the hook $\Delta_{1,max}$ and payload $\Theta_{2,max}$ are:

$$\Delta_{1,max} = \frac{Max\left(\,|L_1\theta_1(t)|\,\right)}{Max\left(\,|L_1\theta_1(t)|\,\right)_{MRC,sim}} \tag{6.17}$$

$$\Theta_{2,max} = \frac{Max\,(\,|\theta_2(t)|\,)}{Max\,(\,|\theta_2(t)|\,)_{MRC,sim}} \tag{6.18}$$

The measures are normalized by the values obtained from the corresponding MRC simulation case without input shaping. In both indices, smaller values indicate smaller swing amplitudes, thus indicating better oscillation reduction.

The hook oscillation reduction is also monitored in terms of the residual swing observed at the end of the trolley motion. The residual swing amplitude of the hook $\Delta_{1,res}$ is:

$$\Delta_{1,res} = \frac{Res\,(\,|L\theta_1(t)|\,)}{Res\,(\,|L\theta_1(t)|\,)_{MRC,sim}} \tag{6.19}$$

The maximum oscillation amplitude from last 10 % of the $\theta_1(t)$ data is utilized. Similarly, this measure is normalized by the value obtained from the simulated MRC without input shaping case. A smaller value of the index indicates better oscillation reduction. Also, note that the residual swing of the payload $\Theta_{2,res}$ was omitted because 1) its influence was indirectly observable in $\Delta_{1,res}$, 2) the measurement was in degree and very small which made the experimental data susceptible to noise and uncertainty.

6.2.2 Oscillation reduction

The benefits of the IS-MRC controllers were first analyzed using the hook and payload oscillation reduction. The payload $m_2 = 0.89$ kg and the rigging $L_2 = 0.41$ m were attached to form the double-pendulum. The trolley was initially at rest and then accelerated to a constant velocity. The data from the experiments were recorded until the trolley reached the edge of the crane workspace.

Figure 6.8 shows the hook swing responses for the various IS-MRC controllers obtained from the experiment. The trials were conducted for the case when the estimated plant frequency ω_n is equal to the first-mode oscillation of the actual double-pendulum crane, thus no estimation error was introduced. As shown by the plot, both the ZV3M-MRC and

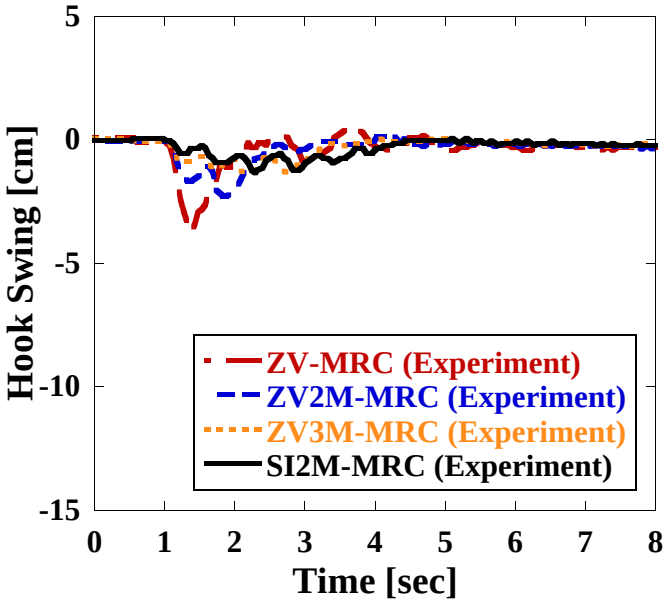

Figure 6.8: Experimental hook swing response of IS-MRC with no error in ω_n

SI2M-MRC demonstrated superior oscillation suppression with peak-to-peak amplitude values of 1.40 cm, followed by the ZV2M-MRC and ZV-MRC which had peak-to-peak values of 2.40 cm and 4.50 cm respectively. The ZV-MRC exhibited the largest transient swing amplitude and was found to be the least effective. All controller designs, however, successfully reduced the residual hook swing toward the end of the trials. This result reflects the discussion from Section 6.1.5 where the ZV shaper was expected to perform the least effective because it only suppresses the vibration mode in the reference model. Also, the ZV3M-MRC and SI2M-MRC resulted in the longest transient period due to the longer shaper durations, as documented in Table 6.3.

To verify the IS-MRC's robustness to the parameter estimation error in the uncertain plant, trials with the same settings as above were conducted while inducing -30% error in the ω_n estimation. The error was introduced by adjusting the hoisting cable length L_1. Figure 6.9 shows the high-error hook swings resulting from experiments. Similar to the previous no-error case, the SI2M-MRC demonstrated superior oscillation suppression with a peak-to-peak amplitude value of 2.10 cm. The ZV3M-MRC was also effective at reducing the majority of the hook swing and had a peak-to-peak value of 2.40 cm, which is slightly

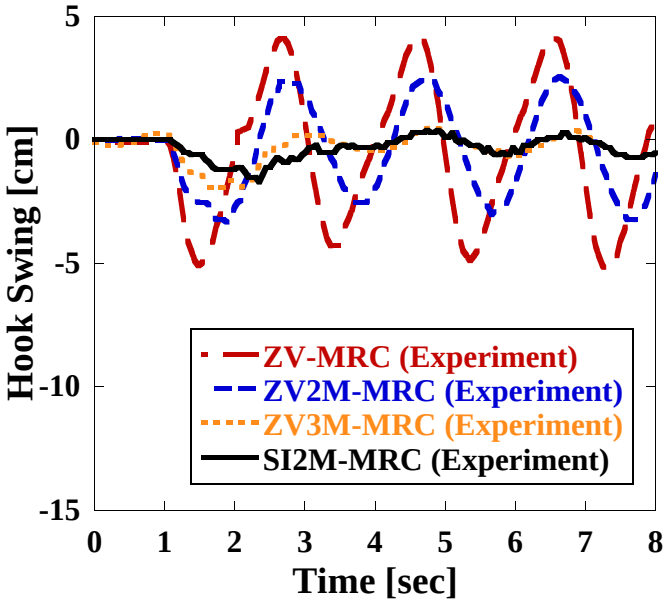

Figure 6.9: Experimental hook swing response of IS-MRC with -30% error in ω_n

larger than the SI2M-MRC. The ZV2M-MRC showed a moderate reduction in the swing amplitude and resulted in a peak-to-peak value of 6.10 cm. The ZV-MRC, however, was not robust enough to handle the large parameter estimation error and failed to eliminate the hook oscillations (the oscillation showed a peak-to-peak value of 9.50 cm). This result, again, agrees with the discussion of the input shapers in Section 6.1.5 where the SI2M was designed to be the most robust to the possible modeling errors.

The payload swing responses from the same trials were also observed. Figure 6.10 shows the experimental payload responses with no estimation error in ω_n. Similarly, Figure 6.11 shows the experimental payload responses with a high estimation error of -30% in ω_n. The payload swing in degrees was measured with respect to the hook position.

The figures show that introduction of the parameter estimation error degrades the performance of the IS-MRC, except for SI2M-MRC. The SI2M-MRC limited the payload swings most effectively and measured peak-to-peak amplitude values of 0.64^o and 1.30^o for the no-error and high-error cases respectively. The ZV3M-MRC and ZV2M-MRC also reduced a large portion of the swing. The ZV3M-MRC had peak-to-peak values of 0.91^o for the no-error case and 1.71^o for the high-error case respectively. The ZV2M-MRC per-

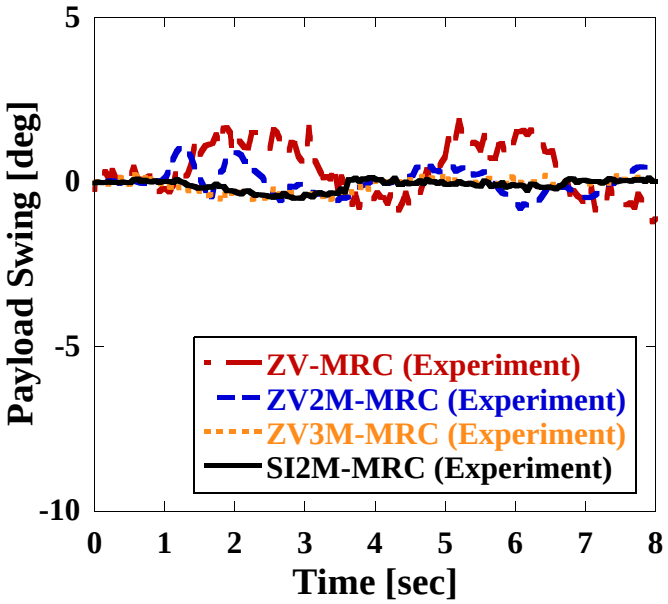

Figure 6.10: Experimental payload swing response of IS-MRC with no error in ω_n

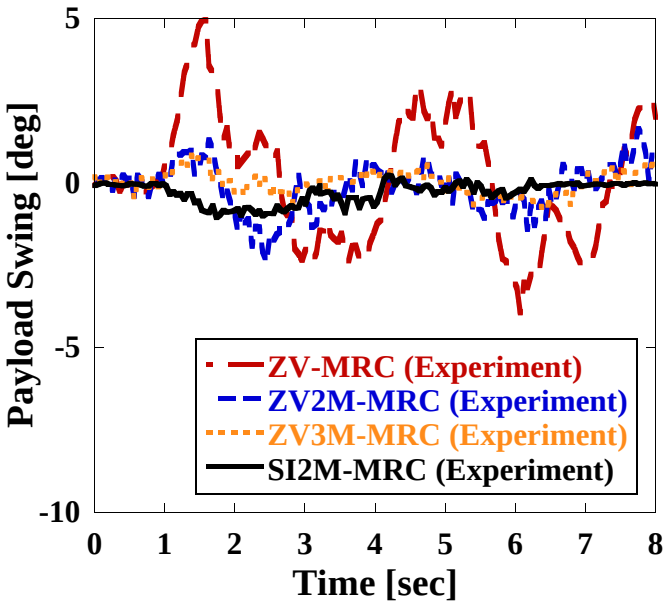

Figure 6.11: Experimental payload swing response of IS-MRC with -30% error in ω_n

formed less effective than the ZV3M-MRC, but achieved peak-to-peak values of 1.91^o for the no-error case and 4.03^o for the high-error case. However, the ZV-MRC resulted in poor performance in the payload swing reduction and took a longer time for the residual oscillation to die out. The ZV-MRC measured peak-to-peak values of 3.09^o and 8.90^o for the no-error and high-error cases respectively

The poor performance of ZV-MRC was expected because, as shown on Table 6.2, the controller neglected the second-mode oscillation of the double-pendulum. Other IS-MRC controllers performed well because their shaper designs attempted to reduce the payload swing as well. The SI2M-MRC demonstrated the highest robustness because the SI2M shaper was designed to suppress the range of frequencies that cause the problematic oscillation. The experimental data of the payload swings were found to be much noisier than the hook swing data. This is because the visual images taken contained a variety of uncertainties that hindered the accuracy of the payload data. The method also had difficulty in distinguishing small changes in the images and failed to fully capture the dynamic behavior of the payload. However, the method succeeded in measuring the payload swing amplitude.

6.2.3 Control Effort Reduction

The corresponding velocity command signals generated in the trial cases in Section 6.2.2 were recorded for the control effort reduction performance. Figure 6.12 shows the experimental u signal with no estimation error in ω_n. As indicated on Table 6.3, the velocity command profile generated by the SI2M-MRC showed the longest shaper duration, followed by the ZV3M-MRC, Zv2M-MRC, then ZV-MRC. The SI2M-MRC signal was very smooth and closely tracks the theoretical velocity profile of the SI2M shaper. The ZV-MRC signal, on the other hand, exhibited some fluctuations before reaching the final coasting magnitude. The fluctuation occurred because the ZV shaper design could not suppress the double-pendulum swings effectively, thus the control effort from the MRC adaptation was required.

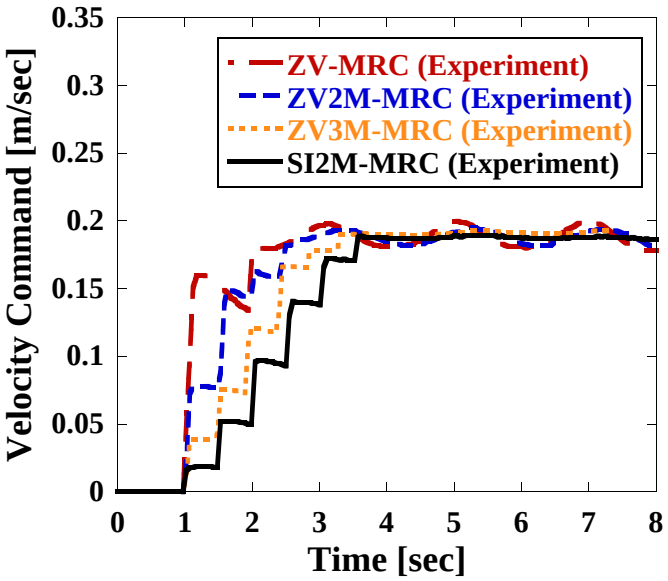

Figure 6.12: Experimental control signal of IS-MRC with no error in ω_n

Figure 6.13 shows the experimental u command with high estimation error of -30% in ω_n. Significant fluctuations in the signals were observed due to the ω_n estimation error. The SI2M-MRC signal showed the least fluctuation, and the signal generated by the ZV-MRC exhibited the largest alteration in the signal amplitude. In general, such high volatility in the command signal is undesired because it increases the actuator load and shortens its life span. The result illustrates that robust IS-MRC designs, such as the SI2M-MRC and ZV3M-MRC, can handle large parameter estimation errors in the plant, while minimizing the cost of increased actuator effort.

6.2.4 Performance comparison analysis

The performances of the IS-MRC designs were examined by attaching different rigging and payloads. The two settings of the rigging cable and payload were: case #1) [$L_2 = 0.41$ m; $m_2 = 0.23$ kg] and case #2) [$L_2 = 0.64$ m; $m_2 = 0.89$ kg]. The trials were conducted using the accelerating motion of the trolley moving at constant velocity until stopped at the edge of the crane workspace. The performances of different IS-MRC methods were compared by both simulation and experimental data.

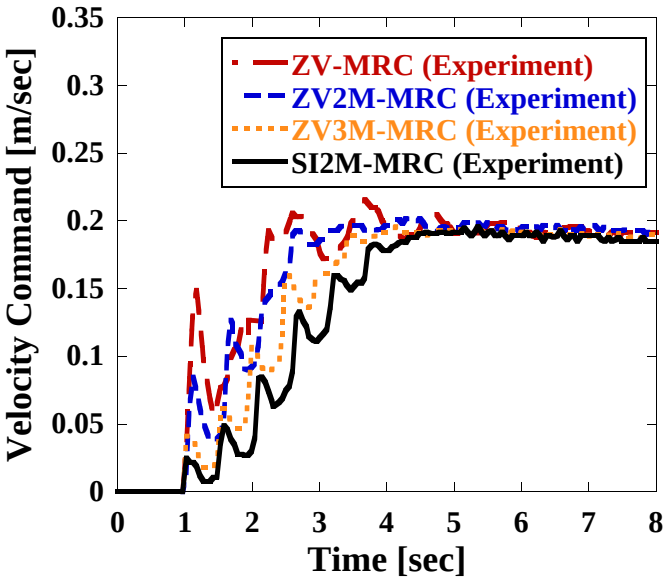

Figure 6.13: Experimental control signal of IS-MRC with -30% error in ω_n

Case #1 simulation results are shown in Figure 6.14, and the case #1 trial experimental results are shown in Figure 6.15. The performance index of ε, μ, $_{max}$, $\Delta_{1,max}$, and $\Theta_{2,max}$ were calculated for the ZV-MRC, ZV2M-MRC, ZV3M-MRC, and SI2M-MRC. Figure 6.16 shows the index values from the case #2 trial in simulation, and Figure 6.17 shows the index values from case #2 experiments. The residual swing of hook $\Delta_{1,res}$ was omitted because the index values from all testing cases were found to be all around zero. This indicates that the residual swings were nearly completely eliminated by both input shaping and MRC.

In both test cases, the SI2M-MRC and ZV3M-MRC exhibited excellent performance. This is because the SI2M and ZV3M shapers attempted to limit all frequency modes considered in the controller design; $\omega_{d,m}$ of the single-pendulum reference model, and $\omega_{1,med}$ and $\omega_{2,med}$ of the double-pendulum plant. In general, the SI2M-MRC index values were slightly lower and thus outperformed the ZV3M-MRC. This is primary due to the difference in the shaper design methods. While the ZV3M reduced the oscillations of the uncertain double-pendulum plant using the representative values $\omega_{1,med}$ and $\omega_{2,med}$, the SI2M shaper effectively suppressed both ranges of the oscillation mode under 5%, as was shown

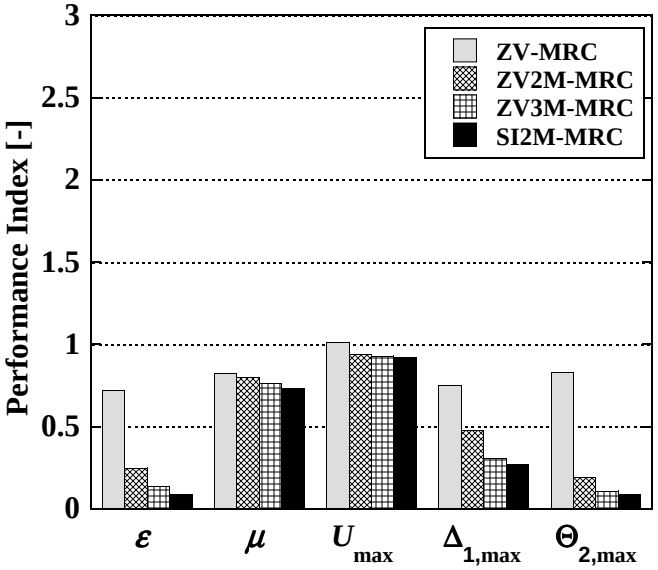

Figure 6.14: Simulation results for case study #1

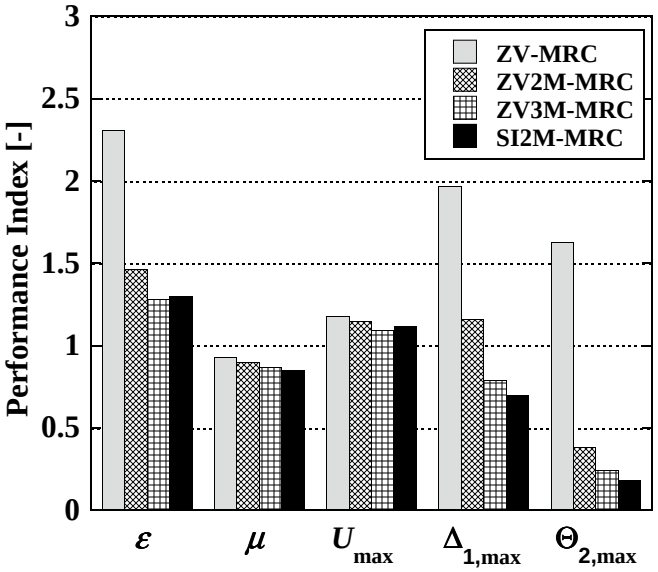

Figure 6.15: Experimental results for case study #1

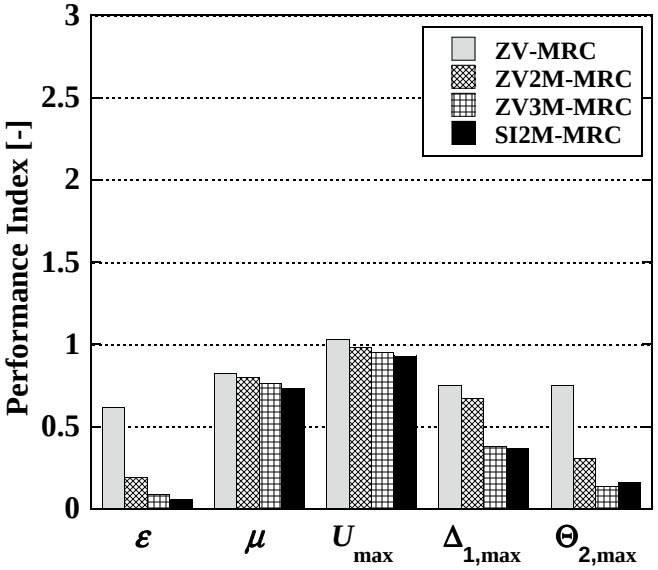

Figure 6.16: Simulation results for case study #2

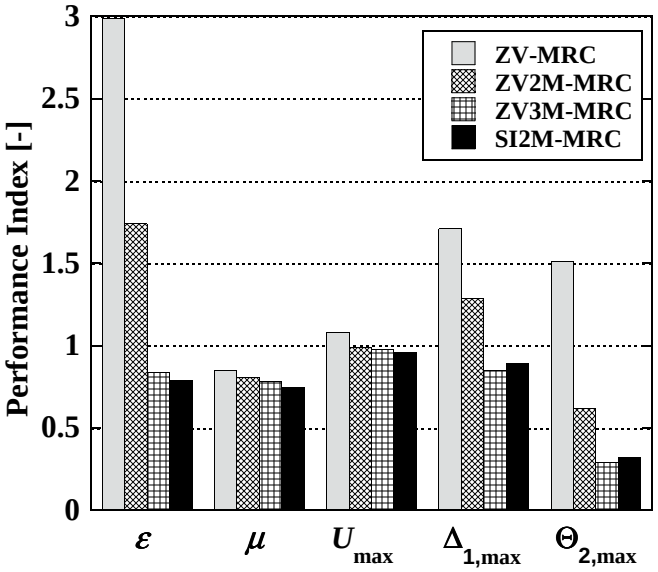

Figure 6.17: Experimental results for case study #2

in Figure 6.7. As a result, the SI2M-MRC became robust to plant uncertainties than the ZV3M-MRC, and produced lower performance index values. The trade-off was lower μ values which indicated that the SI2M-MRC moved the trolley slightly slower than the other IS-MRC designs to acquire large controller robustness.

The index values of the ZV2M-MRC were not as low as those for the SI2M-MRC and ZV3M-MRC. The difference occurred because the ZV2M shaper only suppressed $\omega_{m,d}$ and $\omega_{2,med}$ oscillations. This moderately helped to reduce the complex behavior in the states, facilitated the state tracking of the hook, and reduced the required control effort. However, the ZV2M-MRC performance was not as effective and robust as the SI2M-MRC and ZV3M-MRC because the ZV2M shaper used the representative $\omega_{2,med}$ value for its design. This value was not exact and missed the actual targets. In each case study the actual ω_2 values in the double-pendulum plant were 6.53 rad/sec and 8.25 rad/sec respectively. Therefore, like the ZV3M-MRC, the payload swing reduction by the ZV2M-MRC was not as effective as the SI2M-MRC.

The index values of the ZV-MRC indicated the worst performance of all the control systems. This is because the ZV-MRC was designed to eliminate only the single-pendulum mode in the reference model defined by $\omega_{d,m}$ (and some portion of ω_1 because their values are close). It ignored the second-mode oscillation in the double-pendulum plant. The large payload swing in the plant induces unwanted oscillatory dynamics in the hook, which complicates the state tracking and consequently increases the energy usage by the ZV-MRC. The results of ZV-MRC, as compared to the other IS-MRC designs taking the second-mode frequency into account, indicate that any attempt to reduce the second-mode oscillation in the uncertain double-pendulum plant would be beneficial even if the representative $\omega_{2,med}$ value has significant error.

The experimental results corroborated the simulation data because they showed similar characteristics. The SI2M-MRC and ZV3M-MRC produced the lowest performance indices, followed by the ZV2M-MRC and then the ZV-MRC, which produced the worst

Table 6.4: Performance comparison of IS-MRC controllers

$L_2 = 0.41$ m $(R_L = 0.78)$ $m_2 = 0.23$ kg $(R_M = 0.33)$		ε	μ	U_{max}	$\Delta_{1,max}$	$\Theta_{2,max}$
ZV-MRC	(Simulation)	0.72	0.82	1.01	0.75	0.83
	(Experiment)	3.07	0.98	1.06	0.67	0.99
ZV2M-MRC	(Simulation)	0.25	0.80	0.94	0.48	0.19
	(Experiment)	0.80	0.91	1.05	0.56	0.62
ZV3M-MRC	(Simulation)	0.14	0.76	0.93	0.31	0.11
	(Experiment)	0.21	0.87	1.04	0.38	0.60
SI2M-MRC	(Simulation)	0.09	0.73	0.92	0.27	0.09
	(Experiment)	0.16	0.84	1.05	0.25	0.25
$L_2 = 0.64$ m $(R_L = 1.22)$ $m_2 = 0.89$ kg $(R_M = 1.28)$		ε	μ	U_{max}	$\Delta_{1,max}$	$\Theta_{2,max}$
ZV-MRC	(Simulation)	0.62	0.82	1.03	0.75	0.75
	(Experiment)	3.83	0.98	1.08	1.05	1.27
ZV2M-MRC	(Simulation)	0.19	0.80	0.98	0.67	0.31
	(Experiment)	0.67	0.90	1.06	0.77	1.05
ZV3M-MRC	(Simulation)	0.09	0.76	0.95	0.38	0.14
	(Experiment)	0.22	0.86	1.03	0.46	0.60
SI2M-MRC	(Simulation)	0.06	0.73	0.93	0.37	0.16
	(Experiment)	0.11	0.80	1.03	0.39	0.34

values. The experimental index values were found to be larger than the simulations in most cases, especially in the state tracking. The majority of the sources for this deviation originate in the un-modeled dynamics and uncertainty/error in the real double-pendulum crane. The largest source of the error is likely the sensor noise in the data which hindered the effectiveness of MRC. The data also contained offsets and jumps that needed to be processed during the analysis. In addition, the swing angle of the payload was obtained via an image processing algorithm that does not have high accuracy. All of these factors contributed to the larger index values in the experiment cases.

Table 6.4 summarizes the simulation and experimental results from both test cases for each IS-MRC controller.

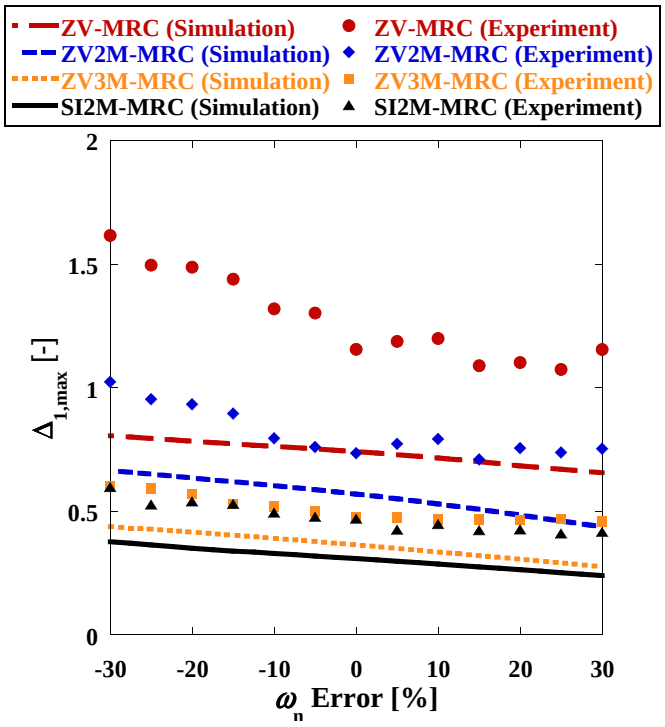

Figure 6.18: Maximum hook swing amplitude $\Delta_{1,max}$ as a function of error in ω_n

6.2.5 Robustness to Plant Estimation

The robustness for the various IS-MRC controllers to the parameter estimation error in the uncertain plant was investigated. A modeling error in the plant's natural frequency ω_n was purposely introduced. The estimated plant model was assumed to have the form defined in (6.1) with $L_{1,med}$, while the hoist cable length in the actual double-pendulum crane was varied to manipulate the first-mode frequency of the plant by $-30\% \sim +30\%$ from the nominal value set to ω_n ($\omega_{actual} = 0.7\omega_n \sim 1.3\omega_n$). The rigging and payload were set to $L_2 = 0.64$ m and $m_2 = 0.23$ kg. The data from the simulation and experiment were recorded for the accelerating motion of the trolley until it was stopped at the edge of the crane workspace.

Figure 6.18 shows the index values of the maximum hook swings, and Figure 6.19 shows the indices of the residual hook swings. On both plots, the experimental data display similar trends as the simulation results. The indices result in higher values at -30% error

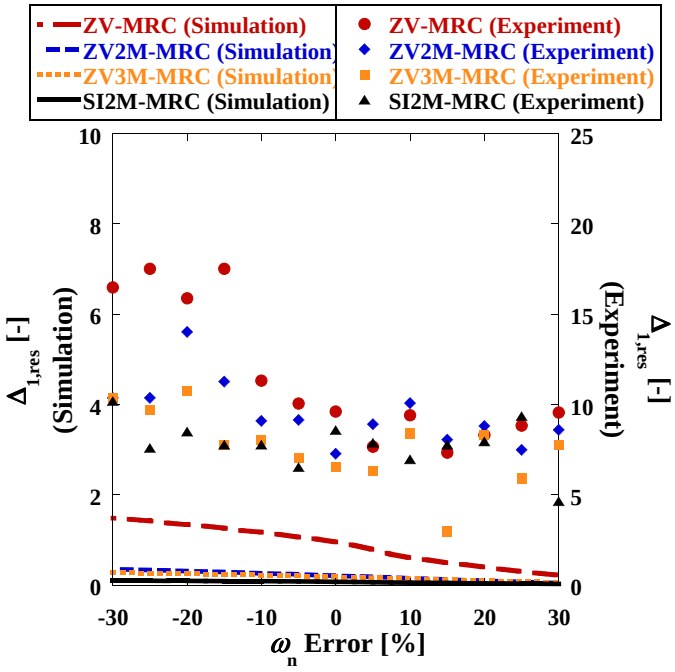

Figure 6.19: Residual hook swing amplitude $\Delta_{1,res}$ as a function of error in ω_n

and lower values as they shift toward $+30\%$ error. This is because when the actual plant has the lower oscillating frequency of $\omega_m = 0.7\omega_n$, the actual cable length is elongated which increases the horizontal displacement of the hook and makes the precise control difficult.

The simulated $\Delta_{1,max}$ values were lower than 1.0, meaning that all IS-MRC designs reduced the maximum hook swing compared to the MRC only case. The simulated $\Delta_{1,res}$ values were near zero for the entire range of ω_n variation except the ZV-MRC because the ZV shaper implemented was the least robust to ω_n error. In addition, the scale of the simulation results and experimental data were found to be significantly different. The experimental data were larger on the scale because of 1) the uncertainties associated with the measurements, and 2) the residual swing amplitude of the simulated MRC used to normalize the index was near zero.

The state tracking performances of the IS-MRC designs are shown in Figure 6.20. Again, the SI2M-MRC resulted in the best performance and the ZV-MRC in the worst. The ZV3M-MRC and ZV2M-MRC also had good performance throughout the range of ω_n variation. The values of ε calculated from the simulation are lower than the experimental

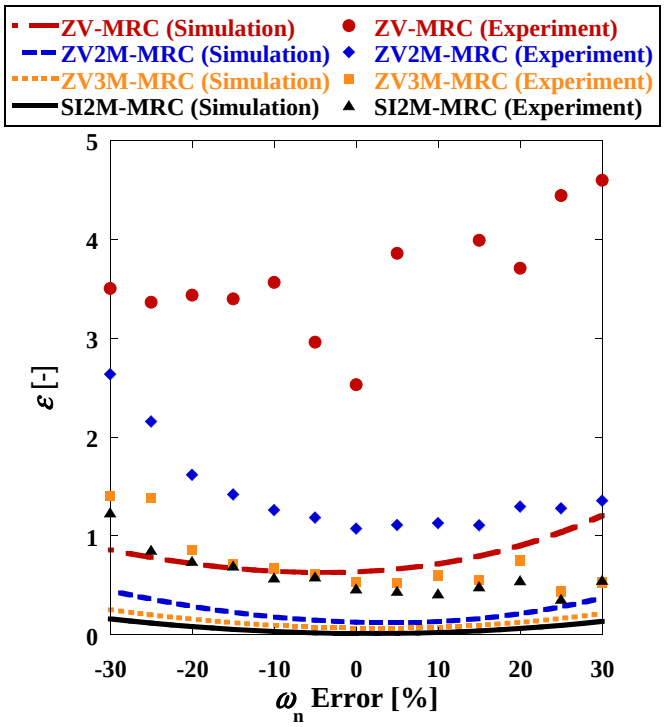

Figure 6.20: State tracking ε as a function of error in ω_n

values, but they exhibit a similar trend in the plots. The ε are the highest when ω_n has the largest variation of $\pm 30\%$ and the lowest when the variation equals to zero, forming parabolic lines. This is intuitive as the state tracking would be the most effective when there is no error in the plant parameter estimation and the most challenged at high errors.

The performance indices of the maximum payload swing are shown in Figure 6.21. The $\Theta_{2,max}$ plots again confirm that the SI2M-MRC and ZV3M-MRC provide superior performance, followed by the ZV2M-MRC and then ZV-MRC. The simulated index values, especially the ZV-MRC, increase as the ω_n error moves toward the $+30\%$ value. At the $+30\%$ region, the hoisting cable length L_1 is shortened. Hence, the fixed rigging L_2 becomes more significant and, as the result, so does the payload oscillation. The experimental data were found to be on a similar scale from the simulated values. However, the data did not capture the same trend observed in the simulation. The cause is likely the uncertainty in the payload swing angle measurements which imposed large imprecision in the data.

Figure 6.22 shows the maximum control effort against the ω_n estimation error, and

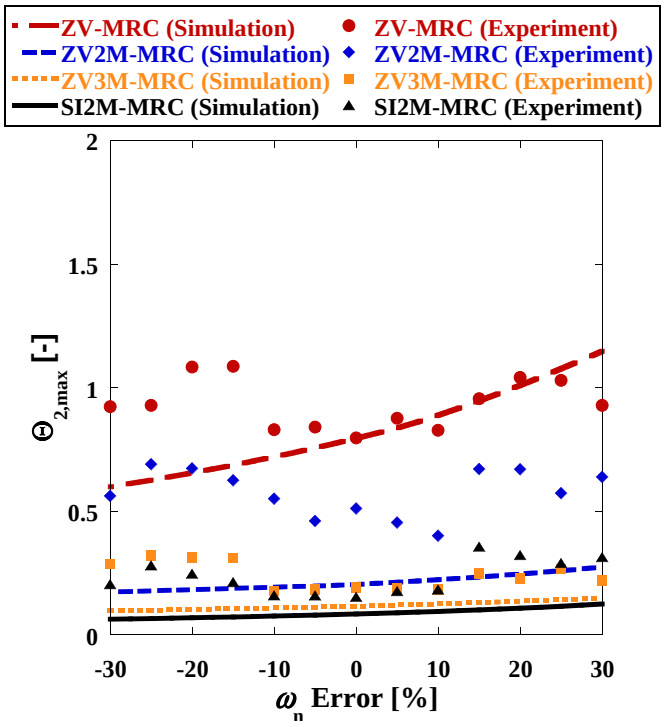

Figure 6.21: Maximum payload swing amplitude $\Theta_{2,max}$ as a function of error in ω_n

Figure 6.23 shows the energy usage against the estimation error. Both U_{max} and μ plots show lower index values at -30% error, indicating that at the lower swing frequency lesser magnitudes of the control effort and energy are used. Similarly, the plots show higher index values at $+30\%$ error because the trolley reacts more aggressively to control the higher frequency swing. The plot of U_{max} shows a good agreement between the simulation and experimental data. The ZV-MRC again resulted in the worst performance, while other IS-MRC designs performed equally well in reducing the maximum control effort. The SI2M-MRC had the lowest μ values and reduced the energy usage most effectively, however, at the trade-off of a slower motion.

The simulation and experimental data also show a similar trend in the plot of μ. However, the experimental values were calculated to be lower than the simulation. There were several unmodeled factors in the real crane, such as the hard nonlinearities and rail friction, that would negatively influence the double-pendulum behavior in the experiment. To minimize the dynamic complexity, the MRC controller tended to move slower in the ex-

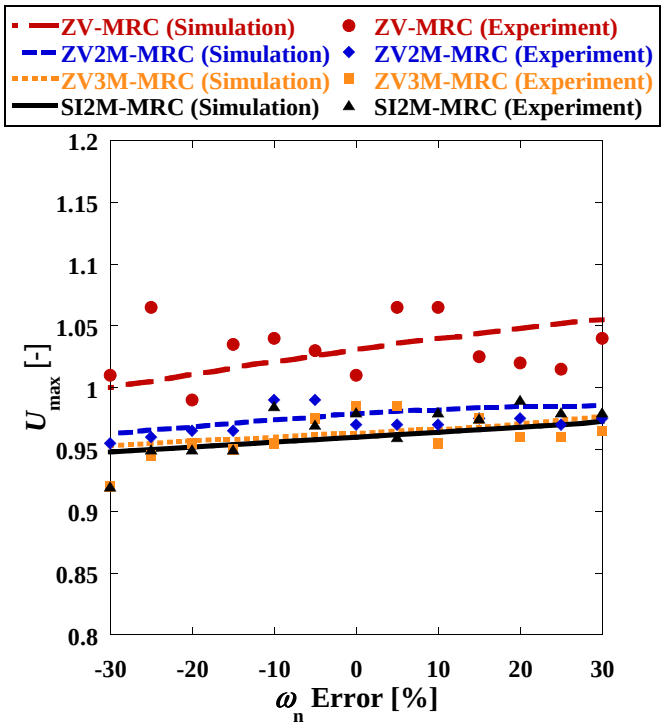

Figure 6.22: Maximum control effort U_{max} as a function of error in ω_n

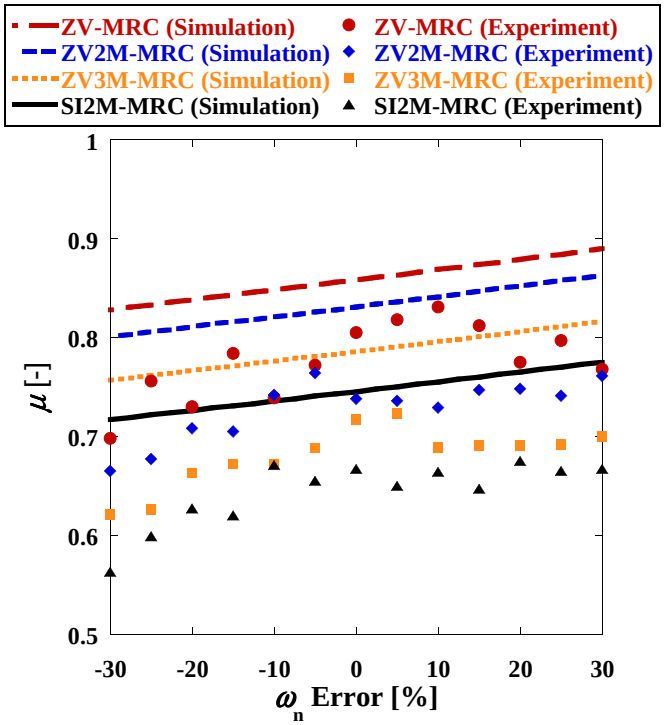

Figure 6.23: Control energy μ as a function of error in ω_n

periments which led to the lower values of μ.

6.3 Summary

In this chapter, four types of IS-MRC designs were developed and applied on a crane with a double-pendulum payload. The crane plant had nonlinear dynamics and uncertain parameters. The IS-MRC controllers were redesigned to reduce sensitivity to the plant parameter variations and system order difference, while maintaining control effort reduction and oscillation suppression performances.

The 4^{th}-order double-pendulum crane was driven via the IS-MRC using a 2^{nd}-order single-pendulum reference model. This was because of easier implementation and difficulty in obtaining accurate measurement of the second mode of a real double-pendulum crane. As the result, the Lyapunov control law using only the states associated with the first mode was derived for asymptotic stability.

Four input shapers (ZV, ZV2M, ZV3M, and SI2M shapers) were designed using the reference model parameters and the possible ranges of the double-pendulum crane natural frequencies. The multi-mode input shapers were targeted to suppress the second-mode payload oscillation. The natural frequency analysis was conducted to determine the appropriate frequency ranges that the shapers must suppress. The plant parameter was estimated by $L_{1,med}$, which was based on the best representation of the uncertain plant. The single-pendulum reference model parameters were calculated with the actuator saturation and maximum overshoot consideration.

The effectiveness of the proposed IS-MRC designs were evaluated via numerical simulations and experiments. The ZV-MRC, ZV2M-MRC, ZV3M-MRC, and SI2M-MRC controllers were investigated for the controllers' robustness to the plant variance and estimation error. Performance indices for the maximum and residual hook swings ($\Delta_{1,max}$, $\Delta_{1,res}$), maximum payload swing ($\Theta_{2,max}$), state tracking (ε), maximum control effort (U_{max}), and energy usage (μ) were measured.

The robustness testing on the system parameters was performed by examining different double-pendulum crane payload and rigging combinations. The robustness to the plant modeling error was also analyzed by inducing $-30\% \sim +30\%$ error in the estimated plant natural frequency. The ZV-MRC presented the worst performance due to its inability to effectively suppress the second-mode oscillation in the double-pendulum crane. The ZV2M-MRC showed a moderate effectiveness because the controller was not as robust as the ZV3M-MRC and SI2M-MRC. The ZV3M-MRC demonstrated slightly less effectiveness than the SI2M-MRC because its shaper design was based on the representative values. The SI2M-MRC achieved the results that were most robust to the plant uncertainties and the system order difference because it suppressed the hook and payload oscillations most effectively. The SI2M-MRC control signal was also very smooth and closely tracked the theoretical velocity profile. The trade-off, however, was a slower motion.

CHAPTER 7
OPTIMIZED IS-MRC DESIGN

CHAPTER SUMMARY:

This chapter will explain the derivation process of the optimized input-shaped model reference control (OIS-MRC) methodology designed for driving a nonlinear, uncertain, time-varying double-pendulum crane. In Section 7.1, the crane plant dynamics is described. The possible ranges of the natural frequencies of the double-pendulum crane are calculated. Section 7.2 presents the OIS-MRC controller design procedure. The reference model parameters and input shaper impulses are obtained via an optimization technique. The OIS-MRC design realizes the shortest time duration while meeting a set of design constraints. In Section 7.3, the performance of the OIS-MRC design is analyzed by numerical simulations and experiments. The state tracking, oscillation suppression, and control effort reduction performances are measured and compared to the traditional SI2M-MRC design.

In the previous chapter, the IS-MRC method (i.e. SI2M-MRC) had shown to be effective in controlling uncertain plant and robust to the plant estimation errors. However, the robust input shaper combined with MRC structure raised an issue of longer rise time and slower trolley motion. For example, the SI2M-MRC took more than 2.5 sec to reach the desired velocity magnitude. This is because the traditional IS-MRC controllers design the input shpaer and MRC independently, and thus results in an overly-robust IS-MRC design.

In this chapter, the IS-MRC design process is refined to solve this issue. The optimal combination of input shaping and MRC design with minimal time-delay is investigated. The improved IS-MRC design is tested on an uncertain, nonlinear, time-varying double-pendulum crane. The performance of the improved IS-MRC is compared and evaluated

against the SI2M-MRC design from Chapter 6.

7.1 Plant Dynamics

The controlled plant considered in this chapter is an uncertain double-pendulum crane with nonlinear dynamics and time-varying parameter. The nonlinear equations of motion in (2.6) and (2.7) are utilized to simulate the plant. The time-variance is introduced to the suspension cable length $L_1(t)$, which corresponds to hoisting up/down motion during the operation. The changing cable length can significantly influences the natural frequencies of the double-pendulum payload.

$$\begin{aligned} \theta_1(t) &= f(m_1, m_2, L_1(t), L_2) \\ \theta_2(t) &= f(m_1, m_2, L_1(t), L_2) \end{aligned} \tag{7.1}$$

7.1.1 Natural Frequency Analysis

Similar to Section 6.1.4, the hook and the payload oscillation modes are analyzed to determine the appropriate frequency ranges that must be suppressed. The expressions of the linearized natural frequencies of the double-pendulum crane from (6.11) are utilized. Because the double-pendulum payload varies with time, the oscillation frequencies for various combinations of the suspension cable length L_1 and rigging L_2 are calculated for the entire range of $R_M = 0 \sim 0.625$.

Figure 7.1 shows the first-mode frequency ω_1 as a function of the cable lengths L_1 and L_2 for the range of R_M. The top surface stands for the $R_M = 0$ and the bottom surface stands for the $R_M = 0.625$ case respectively. The value of ω_1 ranges between the minimum of 2.56 rad/sec, and the maximum of 4.95 rad/sec. The maximum frequency mode corresponds to the shortest $L_1 = 0.40$ m with no rigging $L_2 = 0$ m case where the double-pendulum crane essentially acts as a single-pendulum. The range gives an overall variation of $\pm 31.8\%$ about the median value of 3.76 rad/sec.

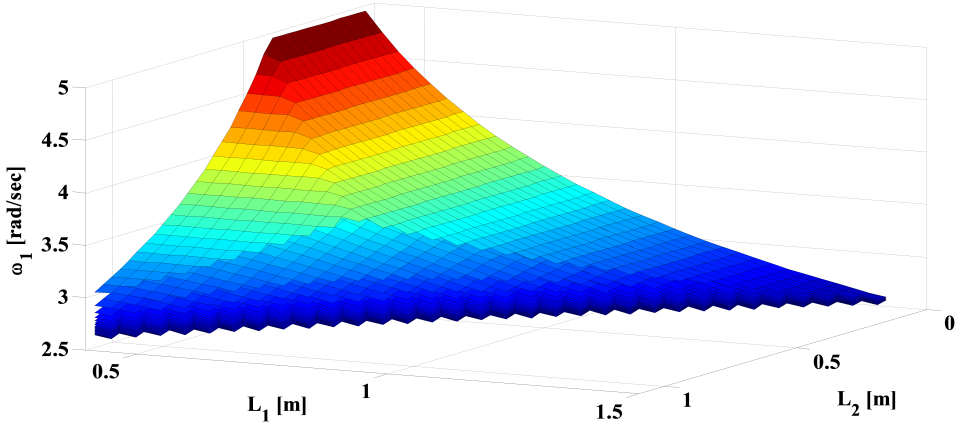

Figure 7.1: ω_1 as a function of L_1 and L_2

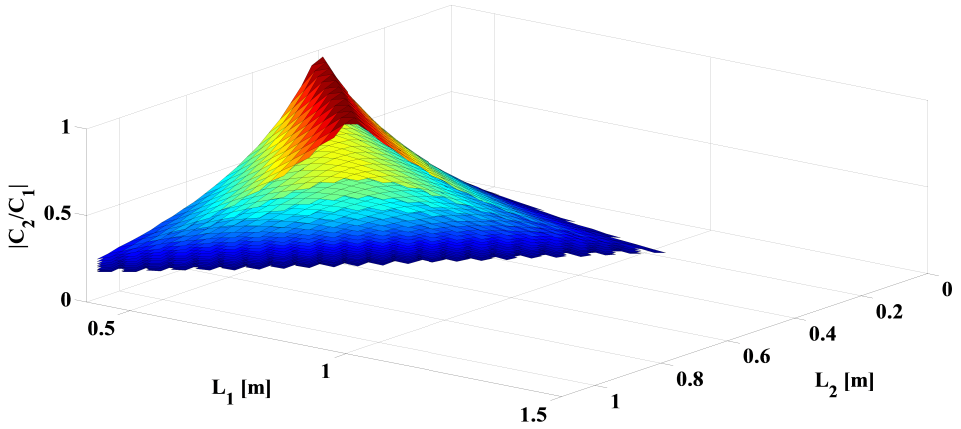

Figure 7.2: Amplitude ratio as a function of L_1 and L_2

The relative swing contribution of the two modes is examined by the coefficients C_1 and C_2 calculated from (6.12). Figure 7.2 shows the ratio C_2/C_1 as a function of L_1 and L_2 for the entire R_M range. The top and bottom surfaces stand for the $R_M = 0$ and $R_M = 0.625$ cases respectively. The plot indicates that the maximum value of the amplitude ratio is around $C_2/C_1 \approx 1.0$, and occurs when the cable and rigging are nearly equal in length ($L_1 \approx L_2$). This corresponds to the case when the double-pendulum dynamics is most vivid in the crane. The significant region of $C_2/C_1 \geqslant 10\%$ is found on the parameter ranges of 0.40 m $\leqslant L_1 \leqslant 1.14$ m and 0 m $\leqslant L_2 \leqslant 1.07$ m.

Using the significant L_1 and L_2 ranges found from the C_2/C_1 ratio analysis, the second-mode frequency ω_2 range that produces problematic second-mode oscillation is determined. Figure 7.3 shows the ω_2 frequency as a function L_1 and L_2 for the entire range of R_M. The

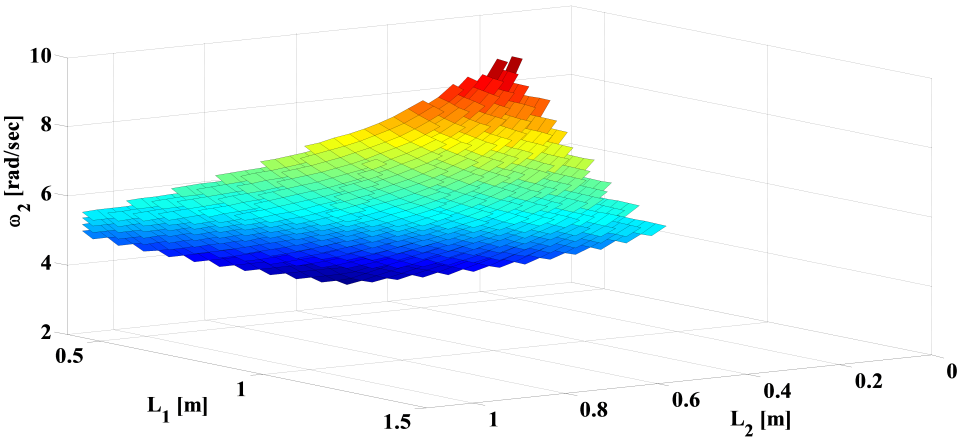

Figure 7.3: ω_2 as a function of L_1 and L_2

top and bottom surfaces stand for the $R_M = 0.625$ and $R_M = 0$ cases respectively. The ω_2 range is found to be 3.63 rad/sec $\leqslant \omega_2 \leqslant 8.99$ rad/sec. This is a $\pm 42.5\%$ variation about the median value of 6.31 rad/sec. The maximum frequency mode corresponds to the shortest $L_1 = 0.40$ m with very small rigging $L_2 \approx 0$ m case.

7.2 Optimized Input-Shaped Model Reference Control

The IS-MRC structure for a double-pendulum payload was discussed in Chapter 6. Taking the same controller form, the optimization method is utilized to find the optimal combination of the input shaper and MRC design. The method concurrently calculates the reference model parameters ω_m and ζ_m, and the input shaper impulses A_i and t_i while satisfying a set of design constraints. The constraints are enforced on 1) the oscillation overshoot, 2) control effort, 3) residual oscillation, and 4) shaper impulses. The method finds the optimized solution that has the minimum time delay in IS-MRC. Hence, it is named an *Optimized Input-Shaped Model Reference Control* (OIS-MRC) [180].

7.2.1 Overshoot Constraints

First, the design constraint is placed on the maximum oscillation overshoot to avoid excessive swing in the hook. The constraint is implemented on the response of the single-

pendulum reference model. The hook swing dynamics in the reference model with input-shaped, step velocity command is derived. Taking an inverse Laplase transformation of the system transfer function in (2.5) gives:

$$\mathcal{L}^{-1}\left\{\Theta_i(s)\right\} = \mathcal{L}^{-1}\left\{G_m(s)V_i(s)\right\} = \mathcal{L}^{-1}\left\{\frac{-\omega_m^2 v_{max}\ A_i e^{-t_i s}}{g\left(s^2 + 2\zeta_m\omega_m s + \omega_m^2\right)}\right\} \tag{7.2}$$

where, *i* indicates the *i*th step command supplied.

Solving the inverse Laplace transformation, the hook' swing angle response in time-domain is obtained:

$$\theta\left(t - t_i\right) = -\frac{\omega_m A_i v_{max}}{g\sqrt{1-\zeta_m^2}} e^{-\zeta_m\omega_m(t-t_i)} \text{sin}\left(\omega_m\sqrt{1-\zeta_m^2}\left(t - t_i\right)\right) \tag{7.3}$$

Because the response to a single step command has been obtained, the response to multiple steps at different time locations can be calculated. The full dynamic response of the hook swing due to input-shaped command is a total sum of each step command response:

$$\theta_{IS}\left(t\right) = \sum_{i=1}^{n} \theta\left(t - t_i\right) \tag{7.4}$$

The expression in (7.4) is simplified by using the following trigonometric identity [94]:

$$\sum_{i=1}^{n} \beta_i \text{sin}\left(\lambda t + \psi_i\right) = B\text{sin}\left(\lambda t + \Psi\right) \tag{7.5}$$

where,

$$B = \sqrt{\left(\sum_{i=1}^{n} \beta_i \text{sin}\left(\psi_i\right)\right)^2 + \left(\sum_{i=1}^{n} \beta_i \text{cos}\left(\psi_i\right)\right)^2} \tag{7.6}$$

$$\Psi = \text{tan}^{-1}\left(\frac{\sum_{i=1}^{n} \beta_i \text{sin}\left(\psi_i\right)}{\sum_{i=1}^{n} \beta_i \text{cos}\left(\psi_i\right)}\right) \tag{7.7}$$

By analogizing the identity expressions to the overall system response in (7.4) and

working some manipulation, the revised hook swing expression is obtained:

$$\theta_{IS}(t) = -\Upsilon \sin\left(\omega_m \sqrt{1-\zeta_m^2}\, t + \Psi\right) \tag{7.8}$$

where,

$$\Upsilon = \frac{\omega_m v_{max}}{g\sqrt{1-\zeta_m^2}} e^{-\zeta_m \omega_m t} \sqrt{(S_{tot})^2 + (C_{tot})^2} \tag{7.9}$$

$$\Psi = \tan^{-1}\left(\frac{S_{tot}}{C_{tot}}\right) \tag{7.10}$$

$$S_{tot} = \sum_{i=1}^{n} A_i e^{\zeta_m \omega_m t_i} \sin\left(-\omega_m \sqrt{1-\zeta_m^2}\, t_i\right) \tag{7.11}$$

$$C_{tot} = \sum_{i=1}^{n} A_i e^{\zeta_m \omega_m t_i} \cos\left(-\omega_m \sqrt{1-\zeta_m^2}\, t_i\right) \tag{7.12}$$

The peak in the input-shaped oscillation response in (7.8) is determined by taking the derivative and setting it equal to zero, $\dot{\theta}_{IS}(t) = 0$. This represents the condition where the swing angle θ, or equivalently the horizontal swing distance x_2, exhibits the largest magnitude. The peak time of the oscillation due to a shaped command t_{p,x_2} is:

$$t_{p,x_2} = \frac{\tan^{-1}\left(\frac{\sqrt{1-\zeta_m^2}}{\zeta_m}\right) - \Psi}{\omega_m \sqrt{1-\zeta_m^2}} \tag{7.13}$$

Also, the maximum horizontal swing distance $x_{2,max}$ at the peak time is:

$$\begin{aligned} x_{2,max} &= \theta_{IS}(t_{p,x_2}) \\ &= \left| \frac{-|v_{max}|}{\omega_m \sqrt{1-\zeta_m^2}} e^{-\zeta_m \omega_m t_{p,x_2}} \sqrt{C_{tot}^2 + S_{tot}^2} \sin\left(\omega_m \sqrt{1-\zeta_m^2}\, t_{p,x_2} + \Psi\right) \right| \end{aligned} \tag{7.14}$$

Similarly, the peak time of the oscillation due to an unshaped command $t_{p,unshaped}$ can be obtained by setting the derivative of the swing response in (7.3), with all $t_i = 0$, equal to zero:

$$t_{p,unshaped} = \frac{\tan^{-1}\left(\frac{\sqrt{1-\zeta_m^2}}{\zeta_m}\right)}{\omega_m\sqrt{1-\zeta_m^2}} \tag{7.15}$$

The expression of the maximum oscillation overshoot Mp_{max} is obtained by finding the ratio of the the maximum horizontal swing distance of input-shaped case to that of unshaped case:

$$Mp_{max} = \frac{\theta_{IS}\left(t_{p,x_2}\right)}{\theta\left(t_{p,unshaped}\right)} = \left|\frac{e^{-\zeta_m\omega_m t_{p,x_2}}\sqrt{C_{tot}^2 + S_{tot}^2}\sin\left(\omega_m\sqrt{1-\zeta_m^2}t_{p,x_2} + \Psi\right)}{e^{-\zeta_m\omega_m t_{p,x_{unshaped}}}\sin\left(\omega_m\sqrt{1-\zeta_m^2}t_{p,x_{unshaped}}\right)}\right| \tag{7.16}$$

This expression presents how much oscillation overshoot would be reduced by implementing an input shaper. The low Mp_{max} indicates small overshoot magnitude achieved by input shaping.

Then, the overshoot constraint is enforced by specifying how much overshoot would be tolerated in the controller design:

$$Mp_{max} \leqslant Mp_{tol} \tag{7.17}$$

7.2.2 Control Effort Constraints

The second design constraint is enforced on the control effort of IS-MRC. MRC possesses an issue of enlarging control effort when the value of natural frequency is estimated poorly, and IS-MRC has shown to mitigate the problem by reducing the maximum actuation and energy usage requirements [158, 159, 161]. In addition, the past research has shown that the crane driven by MRC could move at a low velocity when there is a large modeling error in the LTV system [160]. To achieve an effective performance, MRC must generate sufficient magnitude of the control signal so that the crane can operate at adequate speed.

By intelligently design the shaper and reference model, IS-MRC can confine the control effort magnitude within the desired level.

The maximum magnitude of the control signal is determined from the expression in (6.3) and inserting appropriate system representations. The absolute maximum of the signal occurs when all terms are added constructively:

$$\begin{aligned} u_{max} = &\left|\omega_{est}^2 - \omega_m^2\right| x_{1,max} + 2\left|\zeta_{est}\omega_{est} - \zeta_m\omega_m\right| x_{2,max} \\ &+ |v_{max}| + e_{1,max}P_{1,2} + e_{2,max}P_{2,2} \end{aligned} \tag{7.18}$$

where, ω_{est} and ζ_{est} are estimated natural frequency and damping ratio of the plant. The maximum allowable errors are:

$$e_{1,max} = \alpha \cdot x_{1,max} \tag{7.19}$$

$$e_{2,max} = \alpha \cdot x_{2,max} \tag{7.20}$$

where, α is the allowable tracking error limit of the states given in the percentage and the $x_{2,max}$ term is calculated from (7.14). The error terms are formulated as estimations because the complex nonlinear dynamics in the crane states obstruct the exact form expressions.

The $x_{1,max}$ term is obtained by finding the time where the state x_1 results in the maximum magnitude. As described in Chapter 2, the state x_2 is the derivative of x_1. Therefore, the peak time of x_1, t_{p,x_1}, can be determined by setting (7.8) equal to zero:

$$t_{p,x_1} = \frac{\pi - \Psi}{\omega_m\sqrt{1-\zeta_m^2}} \tag{7.21}$$

The expression of the state x_1 is obtained by taking the integral of x_2. The value of the

$x_{1,max}$ at $t = t_{p,x_1}$ is:

$$x_{1,max} = \frac{|v_{max}|}{\omega_m^2\sqrt{1-\zeta_m^2}} \sum_{i=1}^{n} \Big| A_i e^{-\zeta_m\omega_m\left(t_{p,x_1}-t_i\right)} \Big[\sqrt{1-\zeta_m^2}\cos\left(\omega_m\sqrt{1-\zeta_m^2}\,(t_i - t_{p,x_1})\right) - \zeta_m \sin\left(\omega_m\sqrt{1-\zeta_m^2}\,(t_i - t_{p,x_1})\right)\Big] \tag{7.22}$$

Then, the upper limit constraint on the control effort is placed by enforcing the u_{max} term to be less than the tolerated level, $U_{tol,H}$:

$$u_{max} \leqslant U_{tol,H} \tag{7.23}$$

Next, the lower limit of the control signal is determined to ensure a sufficient speed of the trolley after accelerating to the coasting velocity, or the steady-state. Similar to (7.18), the magnitude of the steady-state control signal u_{ss} can be calculated from (6.3) as $t \to \infty$. In this case, the interest is in determining the minimum value of u_{ss}. The absolute minimum of the signal occurs when all terms except the input velocity command are in negative:

$$\begin{aligned} u_{ss} = &- \left|\omega_{est}^2 - \omega_m^2\right| x_{1,ss} - 2\left|\zeta_{est}\omega_{est} - \zeta_m\omega_m\right| x_{2,ss} \\ &+ |v_{max}| - e_{1,ss}P_{1,2} - e_{2,ss}P_{2,2} \end{aligned} \tag{7.24}$$

where, $x_{1,ss}$ and $x_{2,ss}$ are the steady-state of x_1 and x_2:

$$x_{1,ss} = \lim_{t\to\infty} x_1(t) \tag{7.25}$$

$$x_{2,ss} = \lim_{t\to\infty} x_2(t) \tag{7.26}$$

The steady-state tracking error in $x_{1,ss}$ and $x_{2,ss}$ can also be formulated as:

$$e_{1,ss} = \beta \cdot x_{1,ss} \tag{7.27}$$

$$e_{2,ss} = \beta \cdot x_{2,ss} \tag{7.28}$$

where, β is the allowable steady-state tracking error limit of the states given in the percentage of $x_{1,ss}$ and $x_{2,ss}$ respectively.

Then, the lower limit constraint on the control effort at the steady-state is placed by enforcing the u_{ss} term to be greater than the tolerated level, $U_{tol,L}$:

$$U_{tol,L} \leqslant u_{ss} \tag{7.29}$$

7.2.3 Residual Oscillation Constraints

The third design constraint is placed on a residual oscillation amplitude limit. The constraint is aimed to suppress the two frequencies of a double-pendulum crane while making the IS-MRC robust to any expected oscillation in the two modes. This constraint is the same as other form of optimized input shaper, such as SI2M shaper [105].

The maximum residual oscillation amplitude after applying input shaping needs to be limited under the tolerable level. The expression in (3.1) is applied twice to limit the oscillation of both frequency modes (ω_1 and ω_2) in the double-pendulum crane found in Section 7.1.1. The residual oscillation at each frequency is set below a tolerable level $V_{1,tol}$ and $V_{2,tol}$:

$$V\left(\omega_1, \zeta_1 = 0\right) \leqslant V_{1,tol} \ , \quad V\left(\omega_2, \zeta_2 = 0\right) \leqslant V_{2,tol} \tag{7.30}$$

To ensure the oscillations remain small over a range of frequencies, the oscillation suppression constraint above is enforced at several points near the target frequencies. This approach allows to specify the frequency range over which the oscillation is suppressed

(i.e. frequency range for both the first and second modes of double-pendulum crane).

7.2.4 Optimization procedure

The final set of constraints is enforced on the shaper's impulse amplitude. This constraint can also be found in many common types of input shapers [94].

For the OIS-MRC design, only the positive-impulse shaper is considered. Therefore, the impulse amplitudes are constrained to be positive:

$$A_i > 0 \ , \quad for \ \ i = 1, \cdots, n \tag{7.31}$$

where, n is the total number of impulses in the shaper.

Also, it is desired that the reference command reaches the desired final state. So, the impulse amplitudes are constrained to sum to one:

$$\sum_{i=1}^{n} A_i = 1 \tag{7.32}$$

Due to the transcendental nature of the residual oscillation equations, there are an infinite number of solutions. To select the optimal solution, the cost function minimizing the sum of time location of the final shaper impulse t_n and the shortest rise time t_r is assigned:

$$\min(t_n + t_r) \tag{7.33}$$

where, the rise time of the crane response is estimated from the reference model response [181]:

$$t_r = \frac{1 - 0.4167\zeta_m + 0.2917\zeta_m^2}{\omega_m} \tag{7.34}$$

The OIS-MRC is then obtained using the *fmincon* function of the MATLAB optimization toolbox. The input arguments of the function include the ranges of the suppressing frequencies and estimated plant parameters found in Section 7.1.1 and Section 6.1.5 re-

Table 7.1: Input arguments for OIS-MRC optimization

$V_{1,tol}$	5 %		$U_{tol,H}$	105 % v_{max}
$V_{2,tol}$	5 %		$U_{tol,L}$	95 % v_{max}
Mp_{tol}	30 %		ω_m range	0.01 $\sim$ 9.00 rad/sec
α	10 %		ζ_m range	0.00 $\sim$ 0.90
β	10 %			

spectively. Other arguments are listed on Table 7.1. The numerical values of $V_{1,tol}$, $V_{2,tol}$, and Mp_{tol} were chosen to be consistent with the SI2M-MRC design derived in Chapter 6.

The resulting OIS-MRC design is presented on Table 7.2. The value of ω_m is the same as ω_{est} set at $L_{1,med} = 0.75$ m. This value is determined due to the control effort consideration as the modeling error in ω_n is known to increase the control effort significantly, as shown in Chapter 4. The value of ζ_m is selected to balance the small oscillation overshoot and short response rise time in the reference model. The shaper design of OIS-MRC also has an interesting profile. The shaper consists of only five impulses, where as other input shapers obtained through an optimization process, such as the SI2M shaper shown on Table 6.3, usually consist of even number of impulses and have a symmetric amplitude profile. The shaper of OIS-MRC has the largest amplitude of 31 % in the first impulse, and gradually decreases the amplitudes in a descending order. This profile design allows the controller to respond quickly to the user input and reach the desired final velocity faster. The OIS-MRC design takes only 629 ms to reach 59 % of the final magnitude, where as the SI2M requires 1038 ms to reach only 50 %. To obtain the shaper amplitude over 80 %, the OIS-MRC shaper design takes 1132 ms, compared to the SI2M which need to wait as long as 2078 ms. The time location of the final impulse t_n of the OIS-MRC is 2137 ms, which is 461 ms shorter than the SI2M.

Table 7.2: Controller parameters of the OIS-MRC

ω_m [rad/sec]	3.62				
ζ_m [-]	0.17				
t_i [ms]	0	629	1132	1636	2137
A_i [%]	32	27	22	13	6

7.3 Performance Verification

Numerical simulations and experimental data are used to compare and analyze the OIS-MRC design against the SI2M-MRC. The performances are measured for state tracking, oscillation suppression, and control effort reduction in terms of the indices defined in Chapter 6. The controllers' robustness to the plant uncertainty and time-variance is investigated.

7.3.1 Oscillation and Control Effort Reduction

The hook oscillation response, the payload oscillation response, and the control signal of the IS-MRC designs were analyzed given varying hoist cable length. The trial was conducted for the transient motion where the trolley was initially at rest and accelerated to a constant velocity. A rigging payload of $L_2 = 0.40$ m and $m_2 = 0.26$ kg ($R_M = 0.37$) was used to form the double-pendulum crane. While the crane was in motion, the hoist cable length was either 1) hoisted down from $L_1 = 0.40$ m to 1.00 m ($1.05 \geqslant R_L \geqslant 0.42$), or 2) hoisted up from $L_1 = 1.00$ m to 0.40 m. The data from the simulation and experiment were recorded until the trolley was stopped at the edge of the crane workspace.

Figure 7.4 shows the horizontal swing distances of the hook when the cable is hoisted-down simultaneously. The experimental data generally agree with the simulated plant responses in both the OIS-MRC and SI2M-MRC controllers. The peak-to-peak amplitude values of the SI2M-MRC are 0.62 cm and 1.35 cm for simulation and experiment respectively. The peak-to-peak values of the OIS-MRC are 0.94 cm and 1.55 cm for simulation and experiment respectively. The maximum oscillation amplitude is slightly larger in the

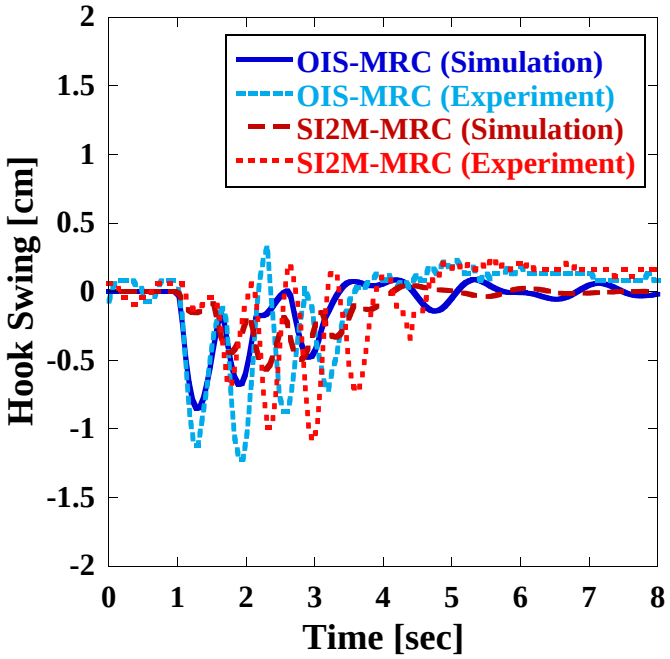

Figure 7.4: Hook responses during hoist-down motion

OIS-MRC due to a larger first impulse amplitude in the shaper design. The maximum amplitude is observed within the first 1.0 sec of the trolley motion in the OIS-MRC controller, compared to the first $1.0 \sim 2.0$ sec in the SI2M-MRC. The OIS-MRC also completes the transient motion earlier in time, slightly before $t = 3.5$ sec, while the SI2M-MRC takes until around $t = 4.5$ sec to finish. This is also consistent with their controller designs which tell that the OIS-MRC controller completes the movement faster than the SI2M-MRC. Both controllers are successful in eliminating the residual hook oscillations.

One source of the noise in the experimental data may be the inaccuracy in the sensor reading. The hook oscillation data tends to be more noisy when the hook is hoisted too close to the camera attached to the trolley. This is because in such condition, the hook fills up almost the entire view of camera. Therefore, any small motion in the hook, such as twist and wobble, may be mistakenly recorded as oscillation.

Figure 7.5 shows the horizontal swing distances of the hook when the cable is hoisted-up. The experimental data very closely tracks the simulated plant responses in both the OIS-MRC and SI2M-MRC controllers. The peak-to-peak amplitude values of the SI2M-

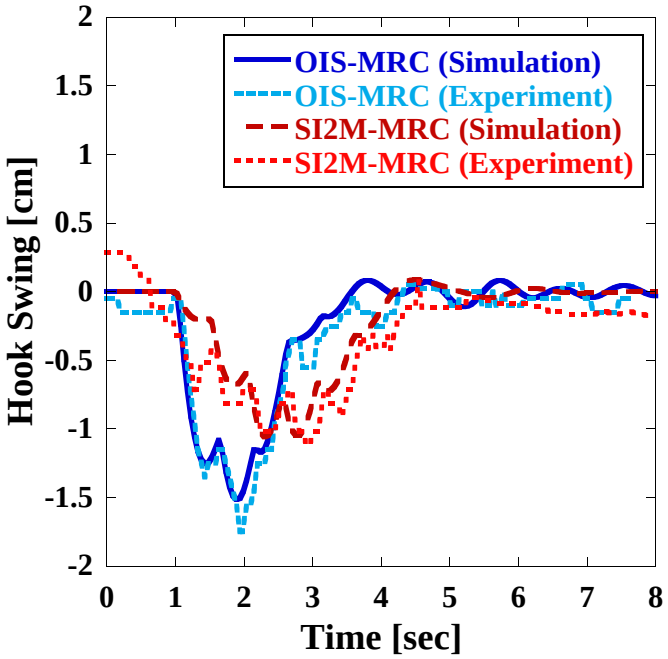

Figure 7.5: Hook responses during hoist-up motion

MRC are 1.15 cm and 1.40 cm for simulation and experiment respectively. The peak-to-peak values of the OIS-MRC are 1.60 cm and 1.80 cm for simulation and experiment respectively. The plot also exhibits a very similar characteristics from the hoisting-down case in Figure 7.4. The main difference is that the maximum swing distance is larger because this trial has a longer cable length of 1.0 m at the beginning of the hoist-up motion.

Figure 7.6 shows the payload oscillation responses during the hoist-down motion. The experimental data of the SI2M-MRC mostly agrees with the simulation. The payload swing angles are reduced within a bounded magnitude of $\pm 0.5^o$. However, the experimental data of the OIS-MRC is found to be different from the simulated value. The maximum swing angle is 1.75^o in the simulation and 0.59^o in the experiment. This is because the OIS-MRC has a larger first impulse magnitude than the SI2M-MRC, thus tends to induce more oscillation. The difference also originates in the uncertainty of the image processing method used to obtain the experimental data. The resolution of the video image is hard to distinguish a very small oscillation of a distant object. Although there is a gap between

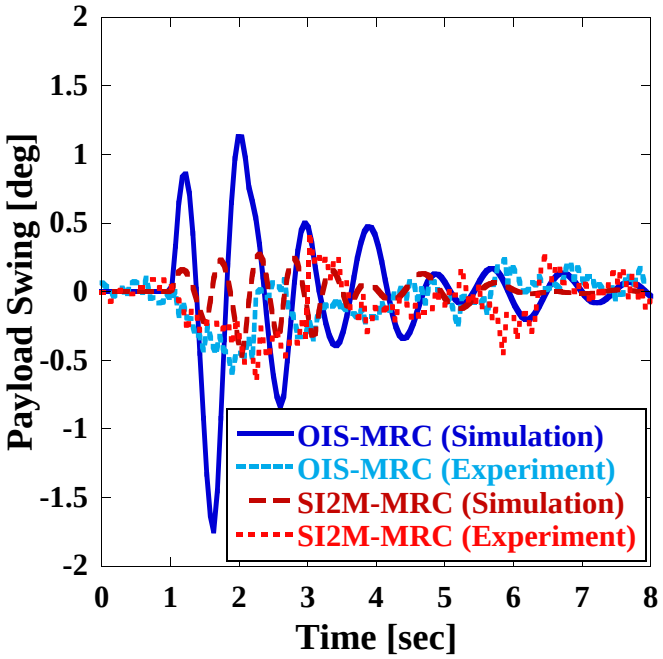

Figure 7.6: Payload responses during hoist-down motion

the experiment and simulation, the OIS-MRC limited the payload oscillations to small magnitude. Both controllers are again successful in eliminating the residual oscillations.

Figure 7.7 shows the payload oscillation responses during the hoist-up motion. The experimental data of the OIS-MRC and SI2M-MRC mostly agrees with the simulation. The plot is very similar to Figure 7.6, and the payload swing angles are mostly limited within a bounded magnitude of $\pm 0.5^o$. The key difference is in the maximum swing angle of the OIS-MRC, which is found to be much smaller in the hoist-up case. This is because when the cable length is long (i.e. 1.0 m or $R_L = 0.42$), the double-pendulum crane acts much like single-pendulum and the first mode oscillation becomes more dominant. This leads to a less oscillation in the second payload mode.

Figure 7.8 shows the velocity command signals during the hoist-down motion. The OIS-MRC reaches the final velocity earlier than the SI2M-MRC because of the shorter shaper duration. In both controllers, the experimental velocity profiles lag the simulation profiles. The final velocity of the SI2M-MRC from the experiment is found to be about 10 % lower than the simulation. The difference in the final velocity indicates that the SI2M-

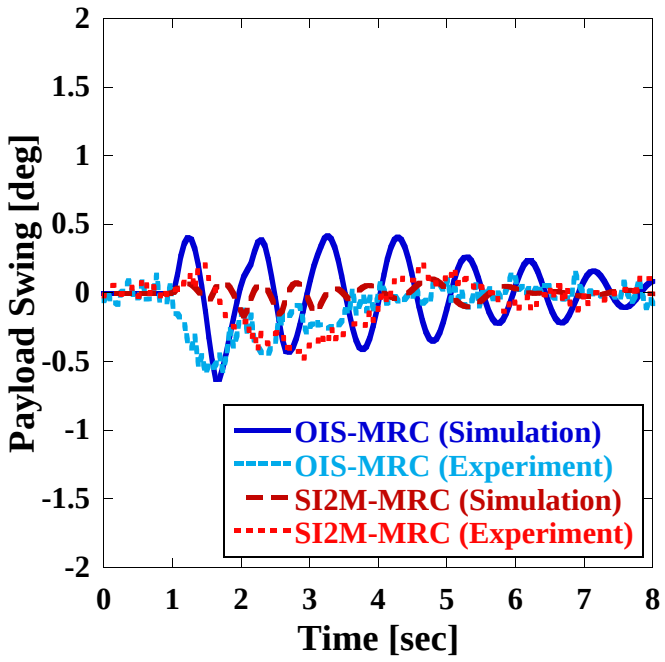

Figure 7.7: Payload responses during hoist-up motion

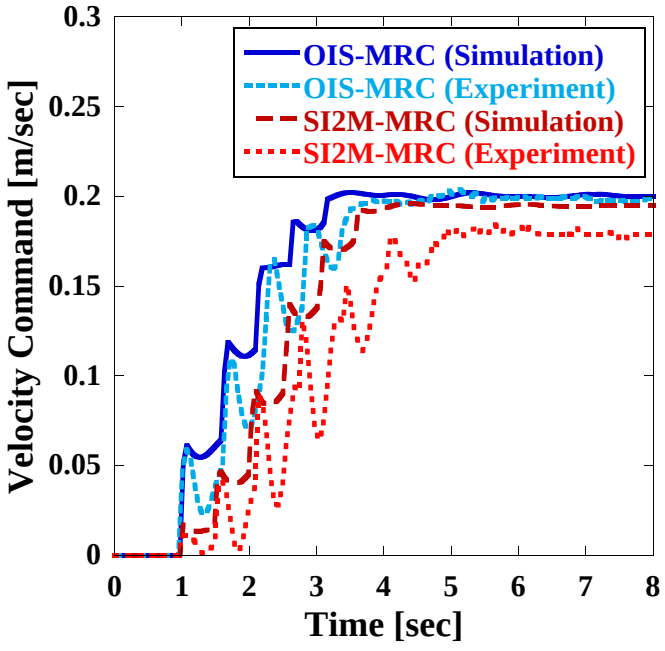

Figure 7.8: Control signal during hoist-down motion

MRC maintains the robustness to the varying parameter and actual plant uncertainties at the cost of moving speed, which is omitted from its design consideration. The experimental data of the OIS-MRC mostly agrees with the simulation. It also reaches the final velocity of 0.2 m/sec, as dictated by one of its design constraints.

Another source of the differences in the profiles may be the inaccuracy of the sensor reading. As discussed in Figure 7.4, the hook oscillation data tend to be noisy when the hook is too close to the camera, which could influence the control signal to either increase significantly or reduce speed to avoid further aggravation. The influence of noise at the beginning persisted throughout the trial and caused the erroneous velocity profiles because the error in the hook swing, or x_2, accumulates in its integral x_1 which is also utilized in the generation of control signal. In addition, the first impulse amplitude of the SI2M-MRC is only 9 % and more likely to cause wobble than oscillation in the hook, unlike the OIS-MRC that supplies 32 % in its first impulse amplitude. Therefore, the OIS-MRC resulted in a better velocity profile than the SI2M-MRC.

Figure 7.9 shows the velocity command signals during the hoist-up motion. Unlike Figure 7.8, the plot shows a very good match between the experiment and simulation velocity profiles. The OIS-MRC resulted in a better profile again because its control parameters were intelligently tuned for the optimal performance. On the other hand, the SI2M-MRC design is merely a simple combination of the SI2M shaper and MRC that were designed independently. Therefore, it is observed that the MRC moderately interferes with the performance of the SI2M shaper, resulting in an inefficient use of the control effort.

7.3.2 Robustness to Time-Variance

The robustness of the OIS-MRC and SI2M-MRC controllers to the time-varying parameter in the plant was investigated. The different values of time-variance in the plant was introduced by changing the hoist cable length L_1 by various lengths while in motion. The cable was either 1) hoisted down from $L_1 = 0.40$ m, or 2) hoisted up from $L_1 = 1.00$ m. The

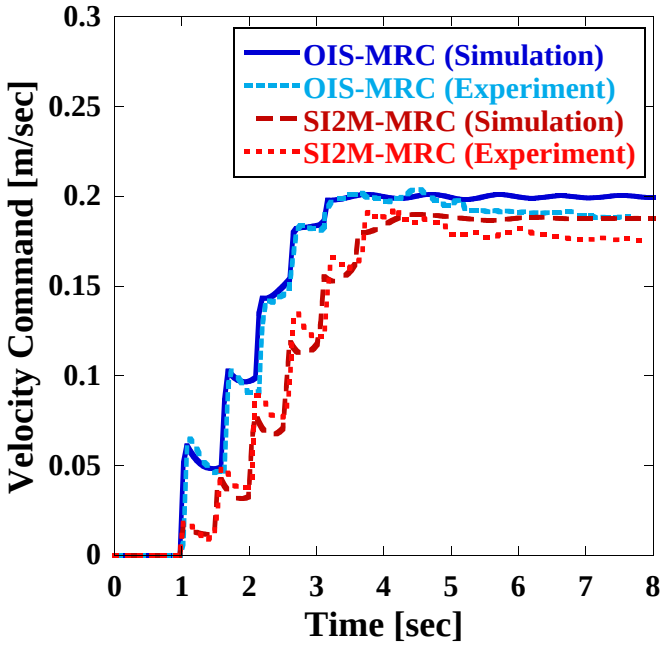

Figure 7.9: Control signal during hoist-up motion

same rigging payload and trial settings were utilized to obtain he data from the simulation and experiment.

Figure 7.10 shows the maximum hook oscillation amplitude index against the hoist down distance. The 0 cm change in L_1 means no change in the hoist cable, and the change of -60 cm indicates that the cable is lowered by that amount. The experimental data agree with the simulation values in both the OIS-MRC and SI2M-MRC. The experimental data result in slightly higher values than simulation, but are within the tolerance. The index values for the OIS-MRC are higher than the SI2M-MRC because of the larger first impulse amplitude which likely to cause a larger swing. The index values also remain flat for the entire range of the hoist distances. This is because both OIS-MRC and SI2M-MRC effectively limited the oscillation of time-varying uncertain plant.

A very similar trend in the hook oscillation can be observed in the hoist-up motion shown in Figure 7.11. Again, 0 cm indicates no change in L_1 and +60 cm indicates that the cable is hoisted upward by that amount. Both OIS-MRC and SI2M-MRC limit the hook oscillation throughout hoist distances. The key difference from the hoist-down case

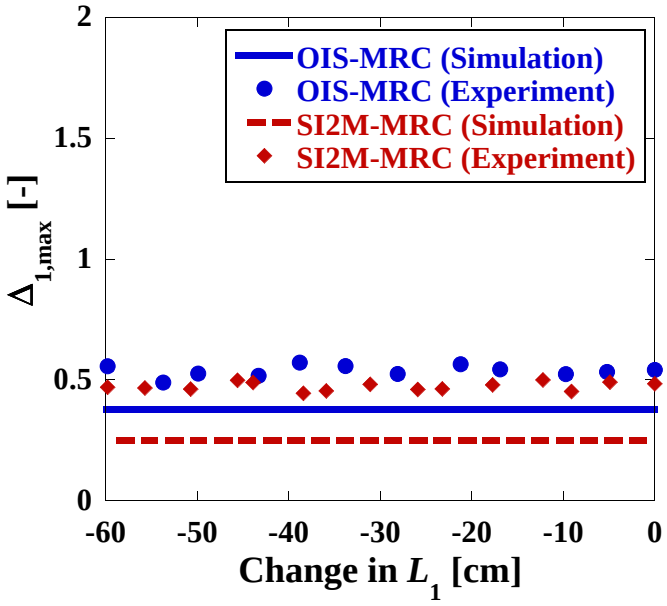

Figure 7.10: Maximum hook oscillation vs hoist-down distance

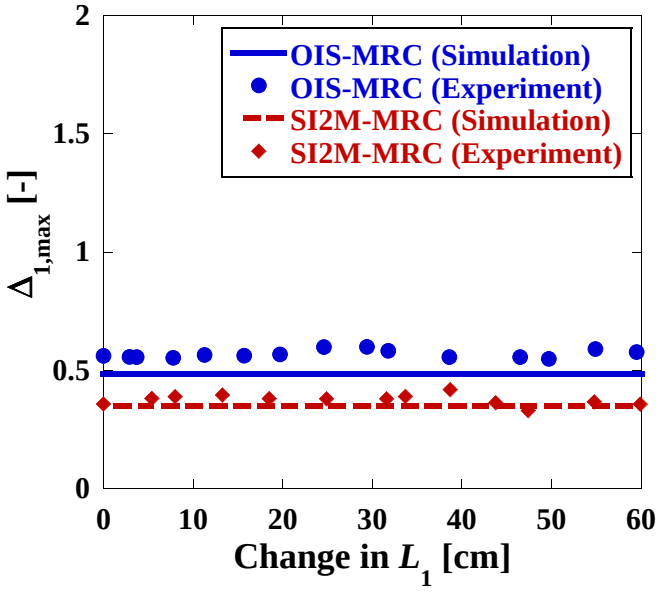

Figure 7.11: Maximum hook oscillation vs hoist-up distance

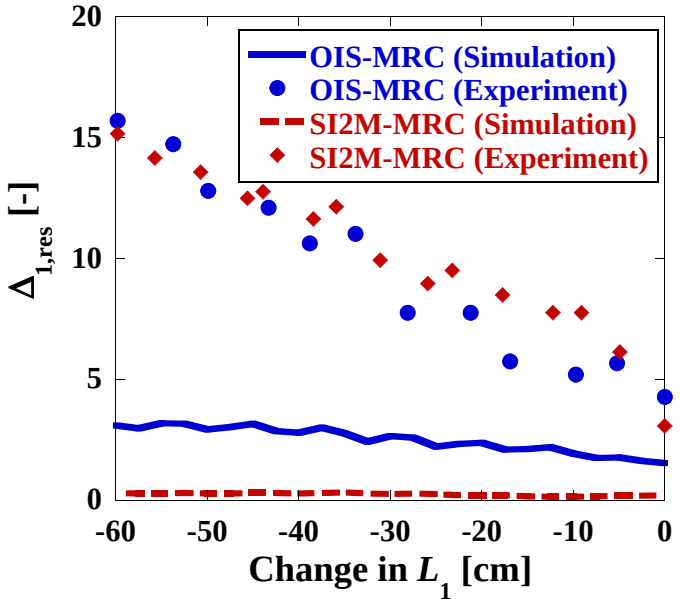

Figure 7.12: Residual hook oscillation vs hoist-down distance

is that the simulated index values are slightly higher compared to Figure 7.10. This is because hoisting the cable upward and downward can either increase or decrease the hook oscillation depending on the states when the hoisting motion is introduced.

Figure 7.12 shows the residual hook oscillation amplitude index against the hoist down distance. The simulation results indicate that the residual oscillations are eliminated by the OIS-MRC and SI2M-MRC in the time-varying plant. Although there are very small residual oscillations, the index values of OIS-MRC result higher. Because the residual oscillation of the MRC used to normalize the index is reduced to near 0 by the damping $\zeta_m = 0.36$, any small residual oscillation remained could magnify the index value. The experimental data are larger and vary significantly than the simulated results. This is because at a longer hoist distance of -60 cm, the hook is positioned further away from the trolley. Therefore, even for the small swing angle, the hook displaces more horizontally than with a short cable length. A similar residual oscillation behavior is also observed for the hoist-up motion shown in Figure 7.13.

Figure 7.14 shows the state tracking error index of hook oscillation against the hoist down distance, and Figure 7.15 shows the index values against the hoist up distance. Both

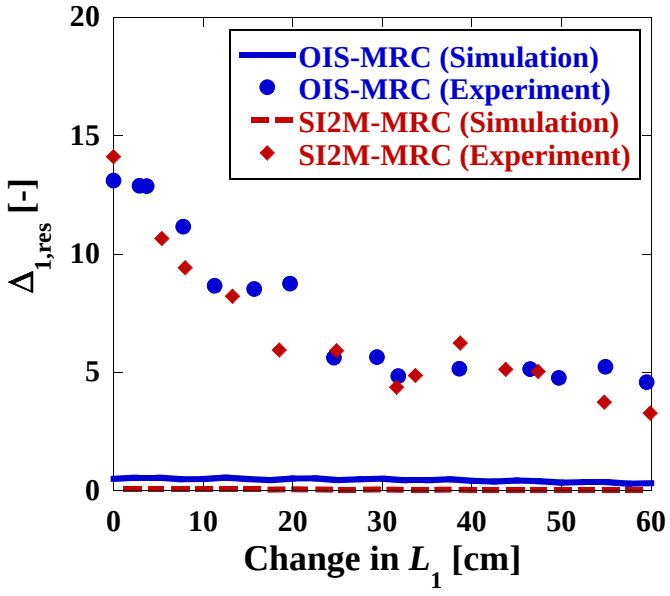

Figure 7.13: Residual hook oscillation vs hoist-up distance

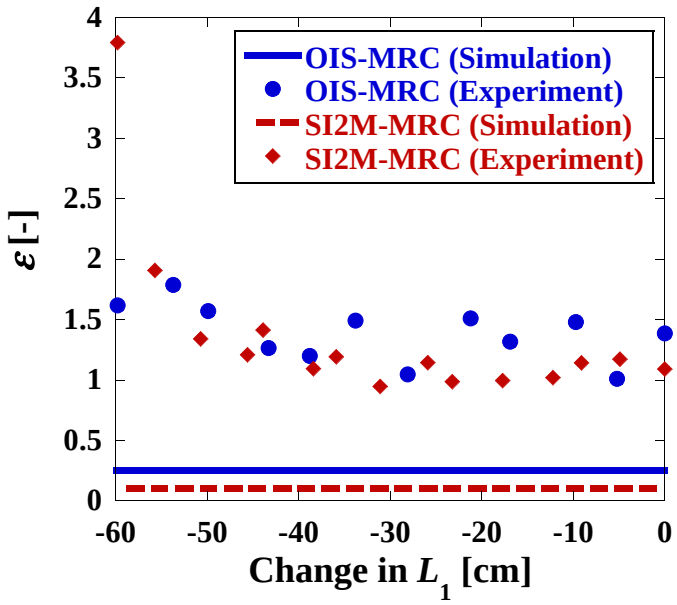

Figure 7.14: State tracking error vs hoist-down distance

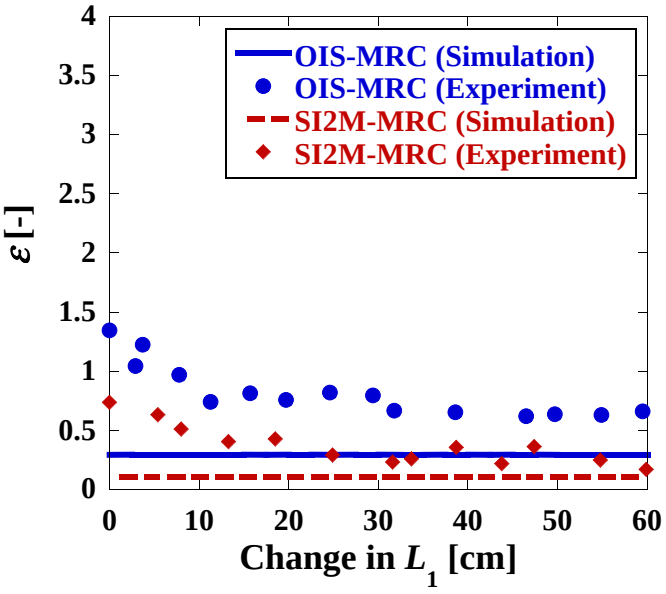

Figure 7.15: State tracking error vs hoist-up distance

figures show higher values in the experimental data, and exhibits the same trend with the simulation in both the OIS-MRC and SI2M-MRC. The index values for the OIS-MRC are slightly higher but about the same low level as the SI2M-MRC, and remain flat for the entire range of the hoist distances. This is because both OIS-MRC and SI2M-MRC effectively limited the oscillation of time-varying uncertain plant, and thus facilitated the state tracking of the hook.

Figure 7.16 shows the maximum payload oscillation angle index against the hoist-down distance. The experimental data show a consistent trend with the simulated results. Both OIS-MRC and SI2M-MRC reduce the payload oscillation and limit the index values flat at the low level throughout the hoist distances. One reason is because the rigging payload set, L_2 and m_2, remained constant in the trials. Another reason is because varying the hoist cable length has more impact on the first mode oscillation associated with the hook than on the second mode oscillation in the payload. The simulated values of the OIS-MRC are small, but higher than the SI2M-MRC because the OIS-MRC controller is designed to be more aggressive compared to the SI2M-MRC. The experimental data for both controllers are at the same level because the image processing method cannot distinguish very small

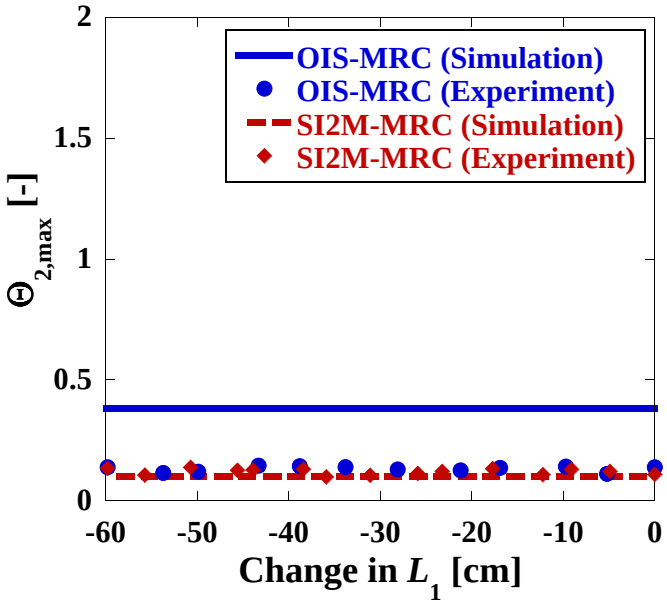

Figure 7.16: Maximum payload oscillation vs hoist-down distance

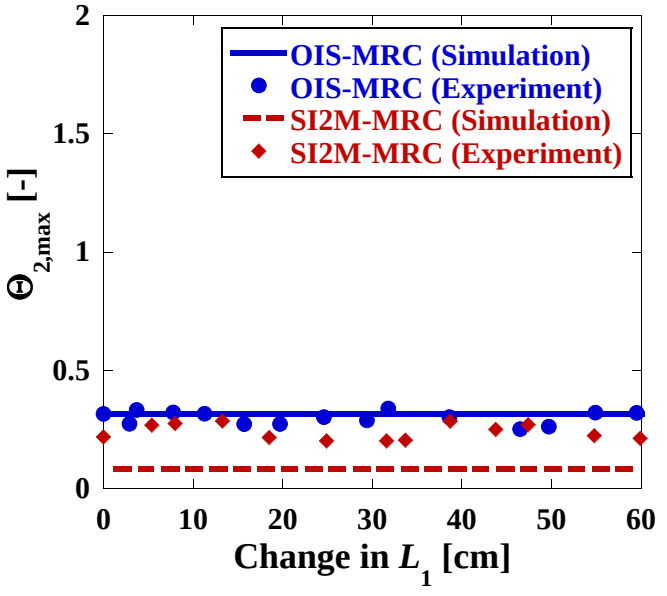

Figure 7.17: Maximum payload oscillation vs hoist-up distance

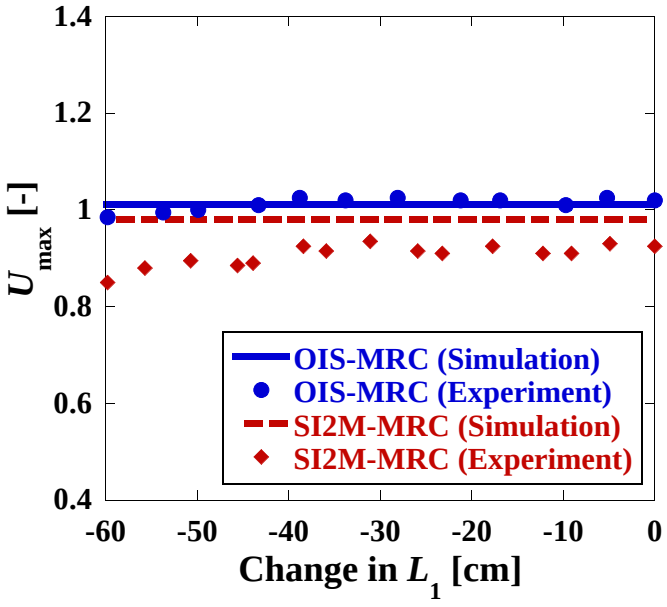

Figure 7.18: Maximum control effort vs hoist-down distance

difference in the payload oscillation. A very similar observation can be also made on the payload oscillation with the hoist-up motion shown in Figure 7.17.

Figure 7.18 shows the maximum control effort index against the hoist-down distance. The experimental data agree well with the simulated results. The OIS-MRC and SI2M-MRC both show nearly no change in the index values, indicating that the hoisting motion itself does not cause a significant change to the control effort. This is because the oscillations are effectively suppressed for the range of frequencies so that the effects of frequency variation on the controller and system dynamics are minimized. The U_{max} of OIS-MRC are contained at the tolerated value of $U_{tol,H}$, specified in Section 7.2.4, and thus prevents the saturation. The index values of SI2M-MRC are found to be lower than the OIS-MRC, especially in the experiment which is -10.49% lower on the average. This indicates that the SI2M-MRC cannot obtain velocity magnitude as high as the OIS-MRC in order to realize the same level of robustness against the plant uncertainty and variance. One of the reason is because, unlike the OIS-MRC, the control effort is not specifically addressed in the design consideration of the SI2M-MRC. The results from the hoist-up motion trials also exhibit the same characteristics, as shown in Figure 7.19.

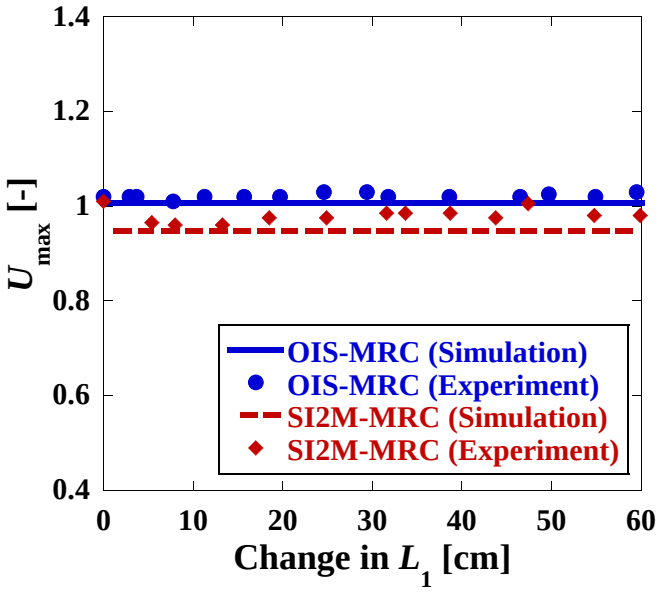

Figure 7.19: Maximum control effort vs hoist-up distance

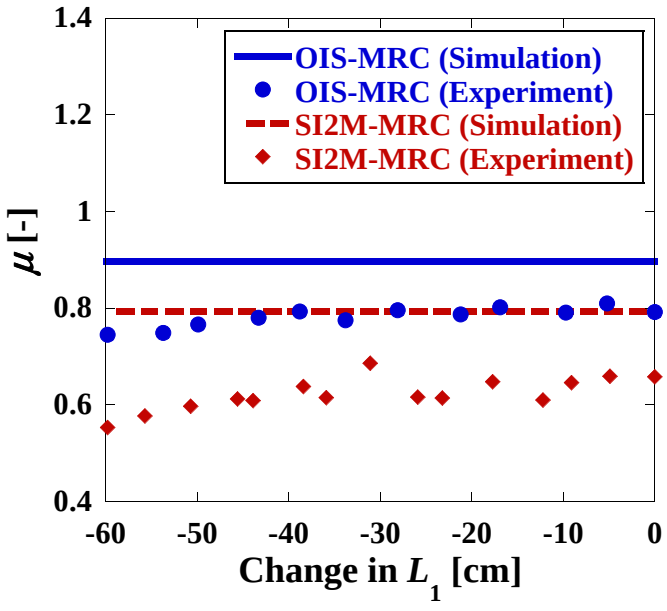

Figure 7.20: Control energy usage vs hoist-down distance

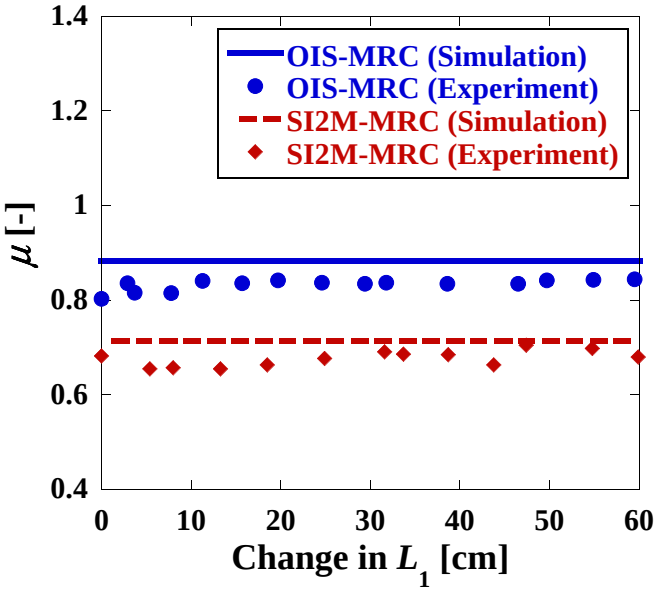

Figure 7.21: Control energy usage vs hoist-up distance

Figure 7.20 shows the control energy index against the hoist-down distance. As discussed in the U_{max} plots, the OIS-MRC and SI2M-MRC show nearly no change in the index values because hoisting motion has a very little influence to the IS-MRC control effort. The values of μ are found to be less than 1 for both controllers, meaning that energy consumptions are reduced compared to the raw trapezoidal command. However, overly reduced μ values also indicate that the trolley travels at much slower speed and thus takes longer operation time. The energy reduction originates in the input shaper element as well as the MRC component which tends to move at slower final velocity, thus less energy usage, to accommodate for the large modeling errors. This effect is more evident in the SI2M-MRC than the OIS-MRC (lower by -14.89 % in simulation and -17.29 % in experiment on the average) because the control effort consideration is not included in its design. The OIS-MRC, as shown in Figure 7.8 and Figure 7.9, travels at the final velocity close to v_{max} due to the u_{ss} constraint. This design constraint allows the OIS-MRC to balance between the energy usage reduction and the fast trolley speed while realizing the same level of the controller robustness as SI2M-MRC. In addition, the experimental data differ on the scale but show a similar trend with the simulated results. The experimental values are lower

because the trolley travels at slower speed due to the modeling errors and the un-modeled nonlinearities present in the real crane system.

The plot of the control energy index against the hoist-up distance also exhibits a similar trend as shown in Figure 7.21. A major difference is that experimental data matches more closely with simulated values for the hoist-up case.

7.4 Summary

In this chapter, an optimized input-shaped model reference control (OIS-MRC) design method was developed. The controller was tested on a nonlinear, uncertain, time-varying double-pendulum crane.

The time-variance in the plant was introduced by changing the hoist cable length $L_1(t)$, which significantly influences the oscillating frequency of the payload. Through natural frequency analysis, the possible ranges of the double-pendulum frequencies that need to be suppressed were calculated.

The derivation method for designing the OIS-MRC was explained. The controller parameters ω_m and ζ_m, and the shaper impulse amplitudes A_i and timings t_i were found through an optimization process. The cost function was set to minimize the total time-delay induced by the IS-MRC design. A set of design constraints on the oscillation overshoot, control effort, and residual oscillations were addressed. The analytical expressions of the constraint equations were obtained.

In the numerical simulations and experiments, the OIS-MRC achieved a large robustness against the plant uncertainty and parameter variance while reducing the time-delay. The controller's robustness was analyzed and compared with a non-optimized IS-MRC method (SI2M-MRC) for different hoist-up and -down distances in the crane. Both the OIS-MRC and SI2M-MRC exhibited large robustness that changing the hoist length did not have notable impacts on the measurement indices, except the $\Delta_{1,res}$ values that are significantly dependent on the final cable length. The OIS-MRC demonstrated a robust

oscillation suppression in the hook and payload, and good state tracking performance. The controller also generated more aggressive control signal with a faster rise time than the SI2M-MRC.

As the trade-off, the OIS-MRC slightly compromised its performance. However, the penalty was minimal and the OIS-MRC was able to maintain the same level of controller robustness as the SI2M-MRC.

CHAPTER 8
DISTURBANCE REJECTION OF IS-MRC

CHAPTER SUMMARY:

This chapter will evaluate the robustness of IS-MRC controller to external disturbances. Disturbance rejection performance of the IS-MRC designs introduced in this thesis are evaluated experimentally. In Section 8.1, the disturbance rejection of the ZV-MRC is tested. An impulsive displacement disturbance is applied to the single-pendulum crane while the trolley is at rest. In Section 8.2, the disturbance rejection of various controllers including the OIS-MRC are evaluated. An external force disturbance is applied to the double-pendulum crane while the trolley is in motion. In Section 8.3, limitations of the IS-MRC design were discussed.

The IS-MRC designs were proven to be robust to the difference between the reference model and plant in Chapter 5, the error in plant parameter estimation in Chapter 6, and the time-variance and uncertainty in plant in Chapter 7. Another important factor to consider in the controller robustness is external disturbance. Figure 8.1 shows the IS-MRC control structure subjected to an external disturbance D in the feedback state. The disturbance could impact the plant behavior and affect the state measurement that is sent to the control law. Thus, successful disturbance rejection is critical especially for MRC controllers because the controller instability can occur not only when the reference model is chosen inappropriately, but also when the state measurements are strongly affected by external disturbances. In this chapter, the disturbance rejection of the IS-MRC designs discussed in this thesis is evaluated experimentally. The ZV-MRC, SI2M-MRC, and OIS-MRC designs are investigated. The tests are conducted on the crane with a single- and double-pendulum payload while the trolley is at rest and in motion, respectively.

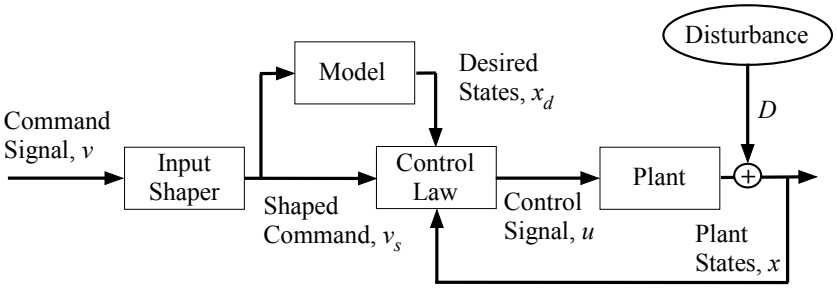

Figure 8.1: IS-MRC controller with external disturbance

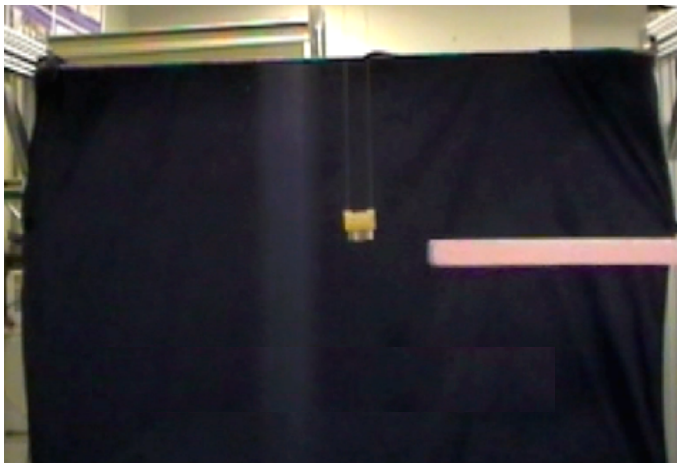

Figure 8.2: Single-pendulum payload given an impulsive disturbance by a rod

8.1 Disturbance Rejection while at Rest

The disturbance rejection feature of the ZV-MRC from Chapter 5 was tested on the single-pendulum crane with small and large errors in the modeling parameters. The parameters of the plant were set to $\omega_n = 3.62$ rad/sec and $\zeta = 0.15$. The parameters of the reference model ω_m and ζ_m were assigned with giving a small ($+1\%$) and large ($+30\%$) modeling error to the values. The experiments were conducted by giving an impulsive displacement disturbance to the payload which was initially at rest (i.e. hitting the payload with a rod as shown in Figure 8.2).

Figure 8.3 shows the payload response and trolley velocity of the crane at the presence of a small modeling error. The external displacement disturbance was added to the payload around $t = 2$ sec. Even when there is a small error in the model parameter estimation, the ZV-MRC can still quickly react to the disturbance (reaching the absolute limit of the trolley

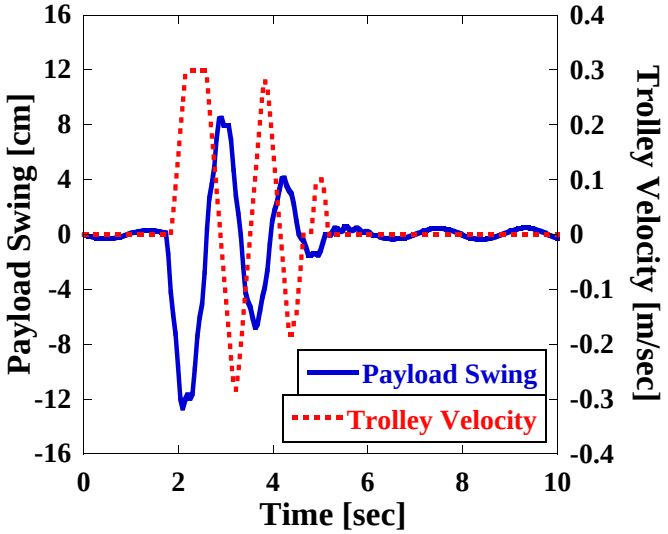

Figure 8.3: Displacement disturbance rejection of ZV-MRC with small modeling error [1.0%]

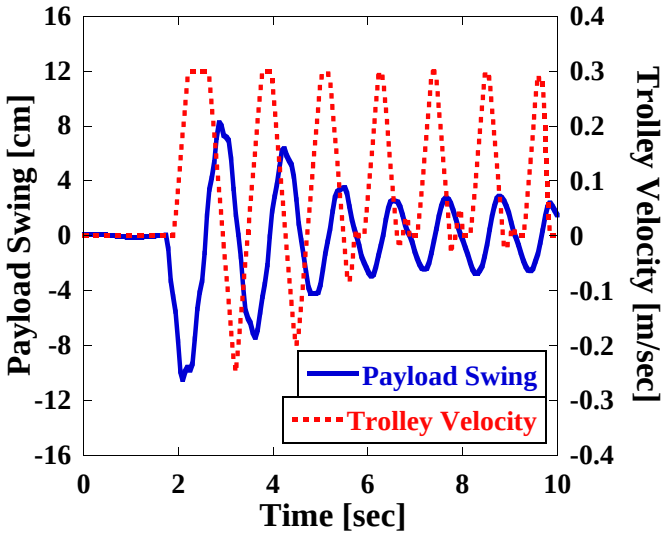

Figure 8.4: Displacement disturbance rejection of ZV-MRC with large modeling error [30%]

velocity 0.3 m/sec) and eliminate the externally induced oscillation in roughly 2.5 sec.

On the other hand, the disturbance rejection functionality becomes ineffective when there is a large error in the parameter estimation, as shown in Figure 8.4. The ZV-MRC reduced some externally induced oscillation but failed to eliminate the residual swings completely, despite of the aggressive attempts by the trolley. The trolley's excitation persisted even after the residual swings were moderately lowered. This is because of the high modeling error which unexpectedly magnifies the control signal u even for small values of the system states $[x_1, x_2]$ and state errors $[e_1, e_2]$. This is highly undesirable in terms of the actuator requirement. In the worst case scenario, because the signal u may no longer reflect the correct state of the system it could even lead to a system instability. The result tells that reasonably accurate modeling of the plant is required for ZV-MRC in order to realize effective displacement disturbance rejection.

8.2 Disturbance Rejection while in Motion

The external force disturbance rejection of the proposed IS-MRC designs were also analyzed and compared against other types of controllers. In this testing, the trolley of the double-pendulum crane started from rest and moved toward an obstacle, a rotating pad shown on Figure 8.5. The payload collided with the pad and was applied a resistant force for a very short amount of time to knock it down, which caused a force disturbance to the payload swing. The tests were conducted for the trapezoidal (raw) command, SI2M shaper, MRC, SI2M-MRC, and OIS-MRC controllers discussed in Chapter 7.

Figure 8.6 shows the hook swing distance and trolley velocity subjected to the external force disturbance when moved by the trapezoidal velocity command. The hook oscillation is induced when the trapezoidal command is supplied to initiate the trolley motion. The force disturbance is applied around $t = 5$ sec and alters the oscillation response behavior. Further oscillation is induced when the stop command is supplied at $t = 8$ sec. The oscillation persists due to a lack of anti-oscillation controller.

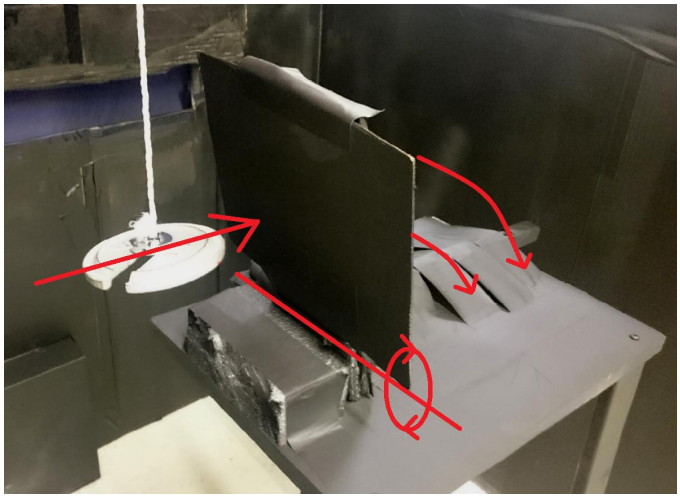

Figure 8.5: Rotating pad obstacle applying an external force disturbance to the payload

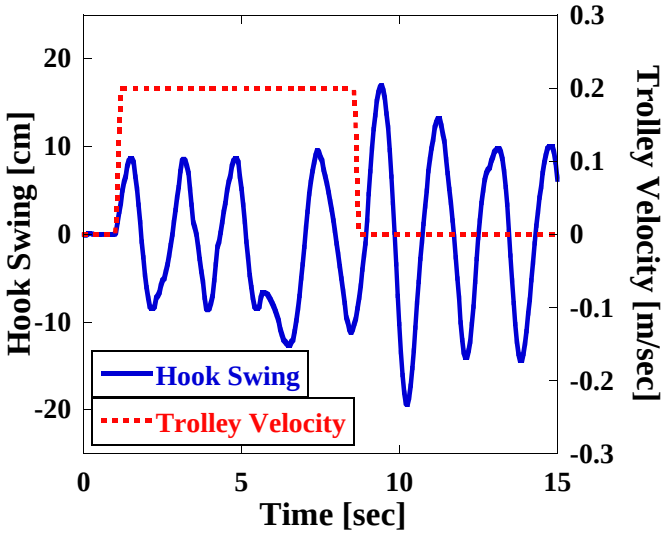

Figure 8.6: External disturbance rejection of the crane moved by trapezoidal command

Figure 8.7 shows the hook swing distance and trolley velocity subjected to the external force disturbance when moved by the SI2M shaped velocity command. When the SI2M shaped command is supplied, the hook oscillation is suppressed for both start and stop command. After the collision around $t = 6$ sec, however, the external disturbance induces a hook oscillation. The oscillation persists for the remainder of the trial because SI2M shaper does not have an adapting feedback loop to reject the external disturbance.

Figure 8.8 shows the hook swing distance and trolley velocity subjected to the external force disturbance when moved by the MRC. The hook oscillation response shows some

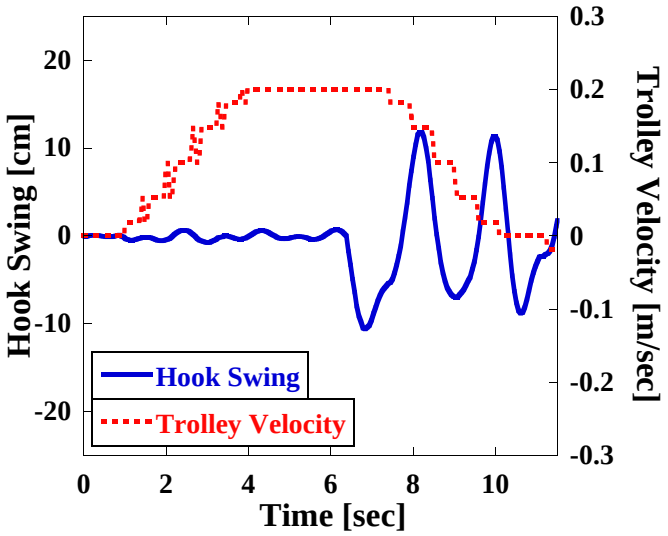

Figure 8.7: External disturbance rejection of the crane moved by SI2M shaper

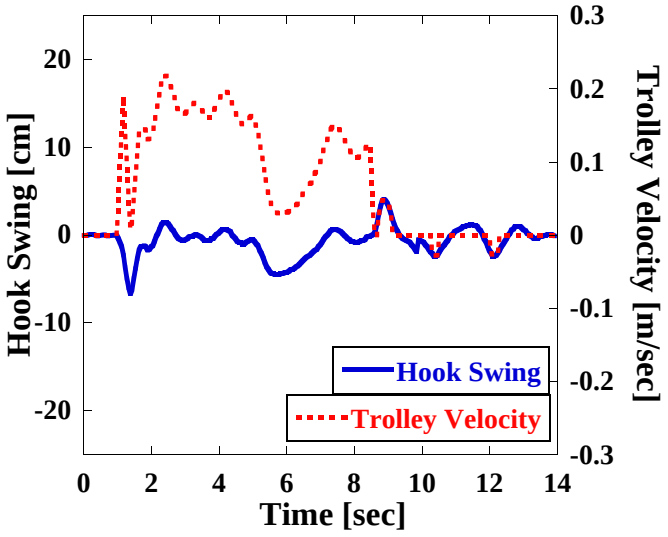

Figure 8.8: External disturbance rejection of the crane moved by MRC

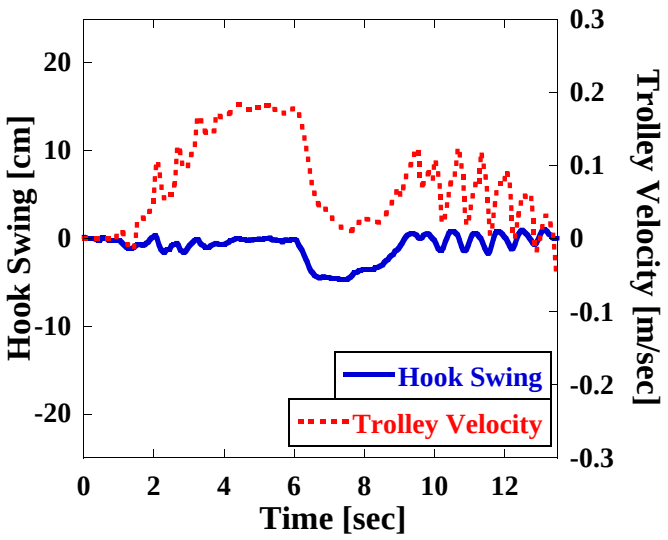

Figure 8.9: External disturbance rejection of the crane moved by SI2M-MRC

spikes at the instances when the start and stop commands are initiated, and when it hits the pad at $t = 5$ sec. However, the oscillations are quickly reduced by the MRC adaptation. The feedback feature of MRC rejects external disturbance well and maintains the hook oscillation at low level throughout the trial. The velocity profile of MRC shows large fluctuations, especially at the start and the obstacle collision where large amount of oscillations are induced. The MRC controller needs to reduce the trolley velocity and vary the control signal significantly to reject the undesired oscillations. In addition, the control signal peaks little after $t = 2$ sec and returns a value of 0.218 m/sec, +9 % above the v_{max} of 0.200 m/sec. This again suggests a concern of actuator saturation when only using MRC.

Figure 8.9 shows the hook swing distance and trolley velocity subjected to the external force disturbance when moved by the SI2M-MRC. Compared to the MRC case in Figure 8.8, the SI2M-MRC effectively limits the oscillations due to the input command and external disturbance to small values. The velocity profile also increases smoothly until it reaches to the maximum of 0.186 m/sec. However, the SI2M-MRC decreases the velocity significantly once the payload collides with the obstacle at $t = 6$ sec. After the collision, the trolley continues to move forward with a fluctuating velocity, even though a stop command is sent. The movement is required to reject the external disturbance and reduce the residual

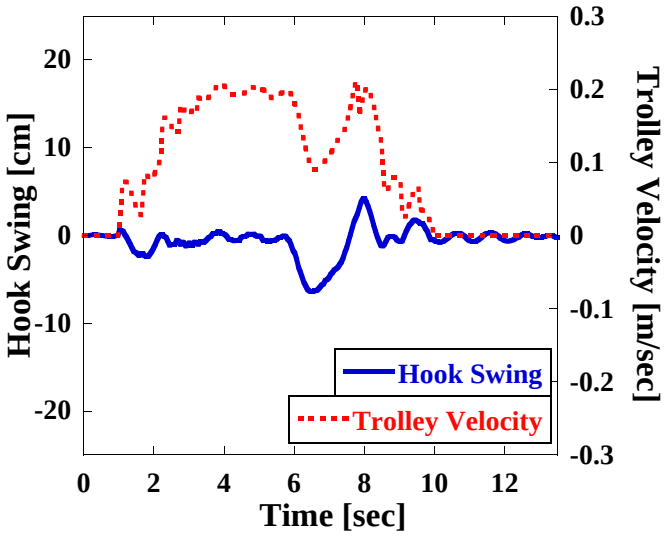

Figure 8.10: External disturbance rejection of the crane moved by OIS-MRC

oscillation.

Figure 8.10 shows the hook swing distance and trolley velocity subjected to the external force disturbance when moved by the OIS-MRC. Compared to the SI2M-MRC case in Figure 8.9, the enhanced robustness in the OIS-MRC contributes to better performances in rejecting an external disturbance, eliminating residual oscillations and generating a smoother velocity profile. The oscillation response shows small humps at the beginning of the velocity command and at the collision with the rotating pad. However, the controller reduces those induced oscillations to nearly zero within a few seconds. The OIS-MRC also eliminates the residual oscillation to nearly zero after the stop command is supplied. The velocity profile is also very smooth at the start and stop command, and shows no rapid and large fluctuations that are observed in the SI2M-MRC case. The trolley travels at the speed very close to v_{max} before the collision. The collision with the obstacle reduces the trolley velocity down to the minimum of 0.090 m/sec, which is much faster than 0.008 m/sec in the SI2M-MRC case. After the collision, the trolley increases the velocity up to 0.210 m/sec (within the tolerance of 5 % limit). Overall, the OIS-MRC demonstrates better performance in rejecting the external force disturbance than other controllers. This can be explain by the OIS-MRC's better parameter selection process compared to the SI2M-MRC where the

controller parameters are designed based on the representative values.

8.3 Limitations of IS-MRC Controller

The IS-MRC designs exhibit robust performance, but also contain few limitations such as signal chattering (explained in Section 5.1.3) and slow rise time (explained in Section 6.2.5). The major limitation of the controller was apparent when these two conditions were met; 1) there was a large gap between the actual plant and estimated model, and 2) the system was subjected to a large external disturbance.

Although IS-MRC controllers demonstrated good robustness to disturbance, there were few instances where the controllers resulted in poor disturbance rejection. Figure 8.11 shows an externally induced response of a payload and trolley velocity with a large estimation error between the actual plant and estimated model. The OIS-MRC controller attempts to suppress oscillation by moving the trolley aggressively. The trolley velocity fluctuated between positive and negative velocities, increased over 0.20 m/sec velocity limit, and reached the absolute actuator limit of 0.30 m/sec and resulted in actuator saturation. However, the residual oscillation persisted and the OIS-MRC controller failed to reject external disturbance completely.

A poor disturbance rejection is caused by a severe increase of the control effort. When a large external disturbance is applied, the plant states x_1 and x_2 also largely increase. This, along with poorly estimated plant parameters, can magnify the control effort significantly due to the state-dependent terms in the control law. In addition, the OIS-MRC design does not consider external forces in its design constraint, and thus cannot guarantee to prevent actuator saturation due to external disturbances.

Another reason that the IS-MRC design is vulnerable to large external disturbance originates from the Lyapunov control law. The structure of MRC control demands that the desired states x_d of reference model and actual states x of plant have similar definition of the system. As explained in Section 4.2, reasonable correspondence between x_d and x is a crit-

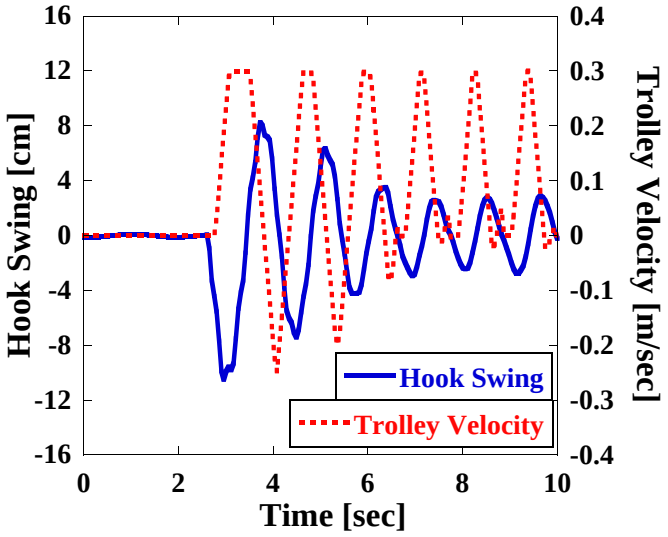

Figure 8.11: Disturbance rejection of OIS-MRC with a large estimation error in the plant model

ical assumption to guarantee a global asymptotic stability of the controller. The IS-MRC control justified this assumption by linearizing system dynamics and realizing a good state tracking. However, this assumption could be violated by large external disturbance that disrupts x state reading and induces significant gap between x_d and x. When the condition for the Lyapunov theory fails, IS-MRC controller could become unstable and produce volatile motion as observed in Figure 8.11

8.4 Summary

In this chapter, the disturbance rejection of the IS-MRC scheme was experimented by applying external disturbances while the crane was at rest and in motion. The IS-MRC designs discussed in this thesis were tested for rejecting the displacement and force disturbances on the single- and double-pendulum cranes.

The single-pendulum crane at rest was subjected to an impulsive displacement disturbance. The ZV-MRC controller was designed with a small ($+1\%$) and large ($+30\%$) modeling error in ω_m and ζ_m. The ZV-MRC successfully negated the disturbance when the reference model parameters were estimated fairly accurately. However, when the model-

ing error was large, the magnitude of the control signal u was unexpectedly amplified and failed to reject the displacement disturbance. The result showed that reasonably accurate modeling of the plant is required for a successful disturbance rejection.

The external force disturbance rejection of IS-MRC designs were also analyzed while the crane was in motion. The trolley started from rest moved toward an obstacle and knocked it down with a payload. When the crane was moved by the SI2M shaper, the payload swing was effectively suppressed before the collision. After the collision, however, the payload swing persisted because input shaping does not have a feedback loop to reject the external disturbance. The payload response of the MRC controller initially showed a small spike caused by the velocity command sent to the trolley. The payload also exhibited some oscillations after knocking down the obstacle. In both cases, the MRC controller rapidly adapted to the disturbances and eliminated the oscillations.

The disturbance rejection of OIS-MRC resulted in superior performance than other controllers. The payload response of OIS-MRC showed the minimal oscillation before and after the collision. The enhanced robustness in OIS-MRC contributed to effectively limit the payload swings caused by the velocity command and also the external force disturbance. The SI2M-MRC controller also demonstrated a good performance in rejecting an external force disturbance exerted while in motion.

However, IS-MRC design also possesses limitation in rejecting external disturbance. A large disturbance could violate the important assumption in the Lyapunov control law and lead to a loss of global asymptotic stability of MRC design. This could result in poor oscillation reduction, controller instability, and significant increase in the control effort.

CHAPTER 9
HUMAN OPERATOR STUDY

CHAPTER SUMMARY:

This chapter will evaluate the performance and usability of the proposed IS-MRC designs by conducting human operator testing. Section 9.1 describes the operator testing setup. The obstacle course features, controller programming and calibration, and experimental procedure are presented. In Section 9.2, the crane trajectories using various controllers are explained. The controller performance is analyzed by observing the navigation path made by each controller design. Section 9.3 shows the results from the human operator testing. A statistical analysis is performed to validate the significance of the data.

In Chapter 7, the OIS-MRC and SI2M-MRC designs were both shown to be effective in controlling a nonlinear, uncertain, time-varying double-pendulum crane. The OIS-MRC design reduced the rise time and shaper duration, while maintaining the same level of the controller robustness as SI2M-MRC. The shorter time-delay also makes the controller more responsive and improves the ease of use. Ergonomics, or usability, is an important factor to evaluate the practicality of IS-MRC controller [182]. In this chapter, the practical use of the OIS-MRC design is evaluated by conducting human operator testing. The controller performance is analyzed by navigating the crane through an obstacle course that simulates a real-world crane tasks and workspace.

9.1 Testing Setup

In this human operator testing, twenty one subjects drove the small-scale bridge crane through an obstacle course. Each subject performed five trials using a trapezoidal (raw

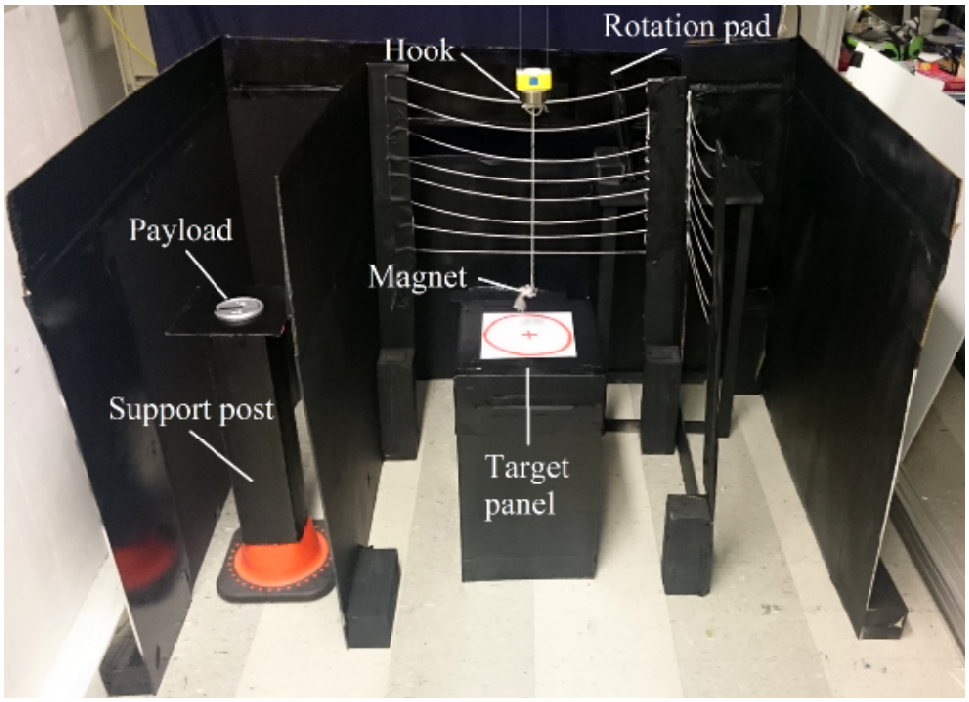

Figure 9.1: Obstacle course for human operator testing

bang-coast-bang) command, SI2M shaper, MRC, SI2M-MRC and OIS-MRC controllers discussed in Chapter 7. In each trial, the completion time and collision count with sidewalls were recorded. The subjects also rated the controller's ease of use after each trial on a scale of 1 to 10, with 1 being the hardest and 10 being the easiest to use.

9.1.1 Obstacle Course

Figure 9.1 shows the obstacle course setup. The course is designed to simulate a real-world crane operation of variable hoist height and payload weight. The course assesses the controllers' robustness to the plant uncertainty and time-variance, external disturbance, and accurate navigation/positioning. The course consists of a target panel, supporting post, and rotation pad. The target panel has a red circle mark where the hook starts from resting position at the beginning and ends with depositing the payload at the end. The supporting post places a metallic payload on the top that is picked up via a magnet wired to the hook. The payload is a metallic weight of 0.227 kg. The rotation pad from Figure 8.5 provides sufficient resistance that induces an external force disturbance. The panel, post and pad

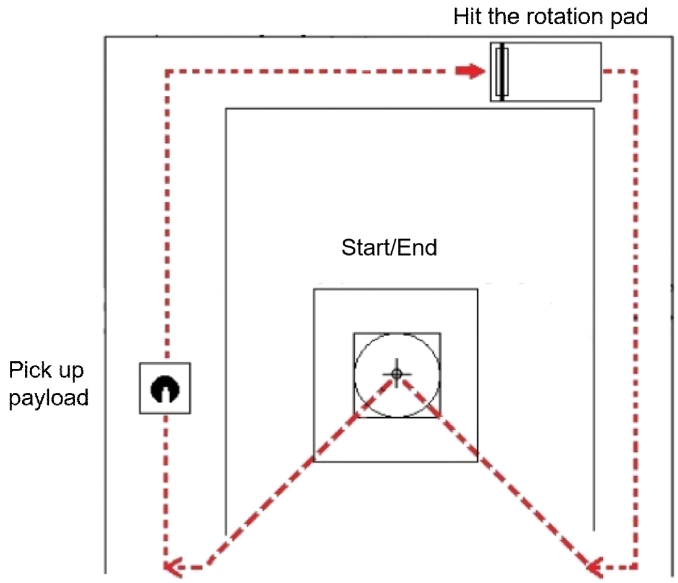

Figure 9.2: Overview of the obstacle course

have a height of 50 cm, 70 cm and 60 cm respectively. The crane is navigated through the narrow path constructed by the sidewalls.

Figure 9.2 shows an overview of the obstacle course and navigated path. Initially, the crane is place within the circle on the target panel at the course center. Then, the crane is moved to the course entrance on the left opening and picks up the payload placed on the support post. The payload is lifted and brought along the course. In the middle of the course, the crane clears the path by knocking down the rotation pad by the payload. Finally, the crane is navigated out of the course and deposits the payload onto the center of the target panel. The goal is to complete the tasks as fast as possible while minimizing the number of collisions.

Figure 9.3 shows the GUI touch panel used to operate the crane. The operators move the trolley, hoist the cable, record and send data, and activate/deactivate various controllers by pressing the corresponding buttons. The screen also displays the current readings of the hook swing, cable length, and position and velocity of the trolley. The operators were given enough time to familiarize with the GUI before the trials.

One restriction on the test subjects was that they were novice operators with a low level

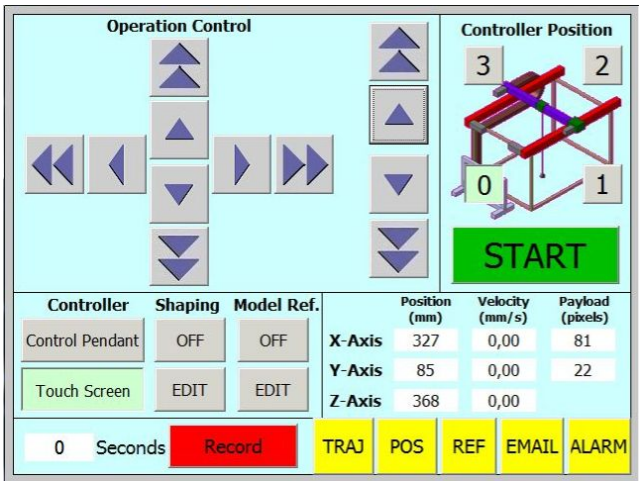

Figure 9.3: GUI on a touch panel

of crane control skills. Novice operators better illustrate how an appropriate control method contributes to efficient crane control. Another limitation was operation learning. The operators become familiar with the controllers and perform more efficiently as they experience more trials. This issue was solved by randomizing the order at which the different control methods were experimented.

9.1.2 Camera Calibration

The crane control and IS-MRC controllers were programmed using *Simotion Scout* software. Figure 9.4 shows a segment of Simotion object-oriented program. The program contains block sections for input shaping, MRC, and inputting and outputting necessary signals to drive the crane setup. The program was implemented on both the trolley (y-axis) and bridge (x-axis) axes of the small-scale bridge crane so that the crane can be operated in a 2D workspace.

The hook position is measured with a camera attached to the trolly. It captures laser light reflected from a reflective card on the hook. Due to the structural limitation, the camera can not be placed perfectly normal to the ground and captures the image at tilted position. This affects the accuracy of the hook angle measurement. This problem is predominant in the x-axis of the crane. The problem aggravates when the hook is hoisted up

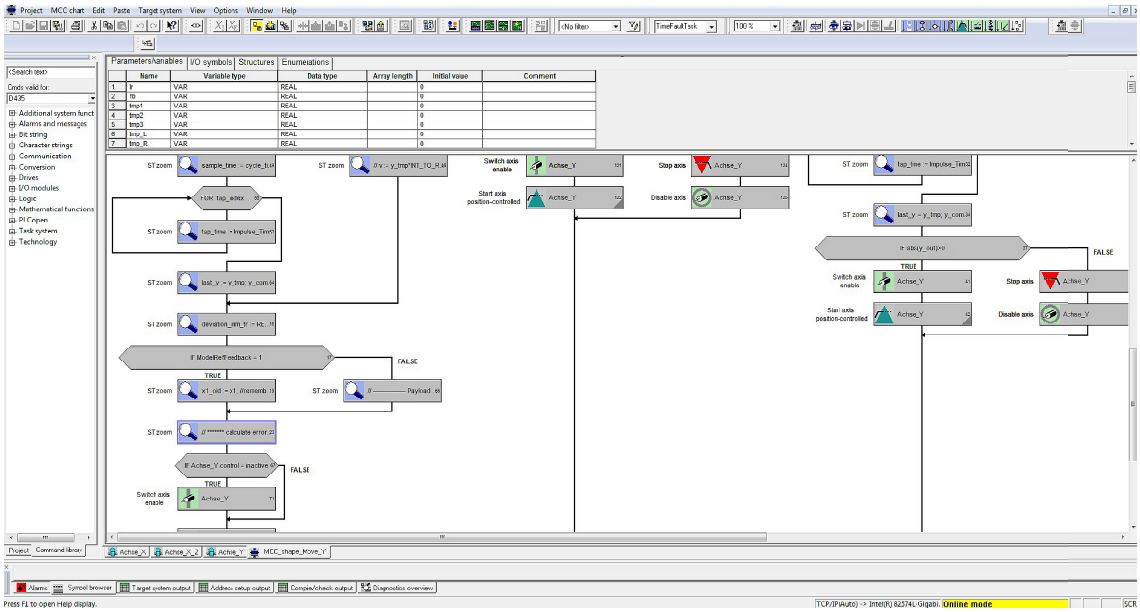

Figure 9.4: Simotion Scout program

and positioned close to the camera.

Figure 9.5 shows the captured image of the hook position at the cable length equals to 115 cm. The green square represents the detecting window and the white blob represents the hook. The center of the blob is off the window center by only 8 pixels in the x-direction. The camera successfully captured the blob position at the center of the image. However, in case of the cable length equals to 45 cm, the camera had difficulty in fully capturing the blob as shown in Figure 9.6. In this case, the blob center is off the window center by 77 pixels in the x-direction. Furthermore, the blob is placed too close to the camera that the majority of the image lays outside of the detecting window. This could cause errors in the hook position measurement, which is a critical issue for implementing MRC controller.

To solve this issue, the camera reading was calibrated in x-axis direction. Figure 9.7 shows the 3rd order regression line for the camera readings at various hoist cable length. At no swing condition, 24 data points at various cable lengths between 45 cm to 115 cm are acquired and processed for a polynomial regression fit. The regression line equation is:

$$DR = -0.0048CL^3 + 0.2607CL^2 - 6.6005CL + 82.09 \tag{9.1}$$

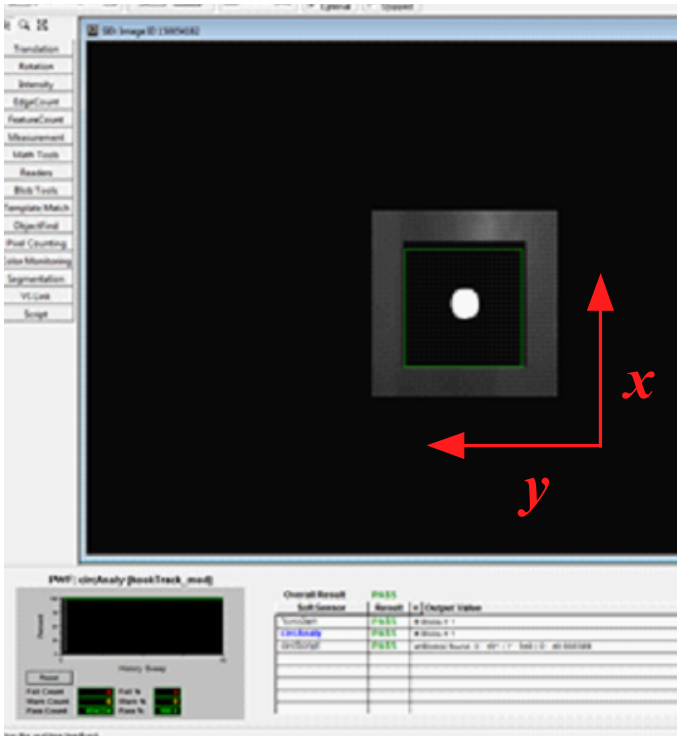

Figure 9.5: Captured image of the hook position at cable length of 115 cm

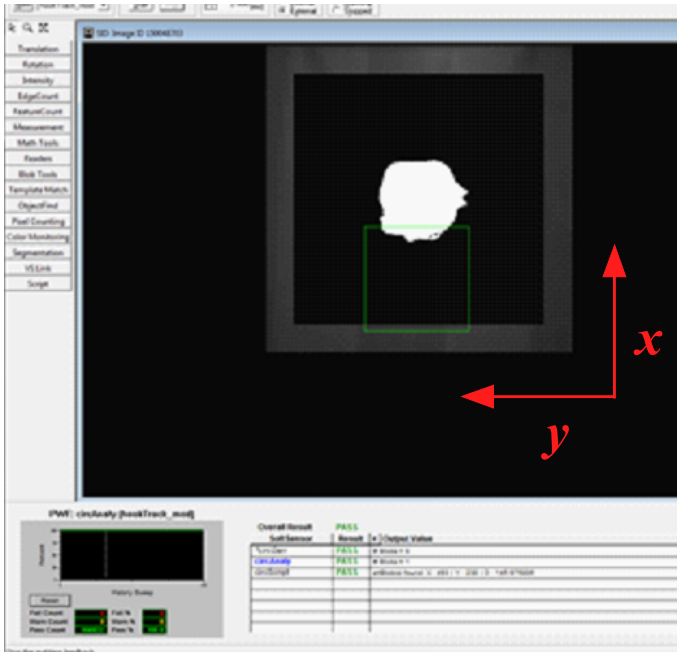

Figure 9.6: Captured image of the hook position at cable length of 45 cm

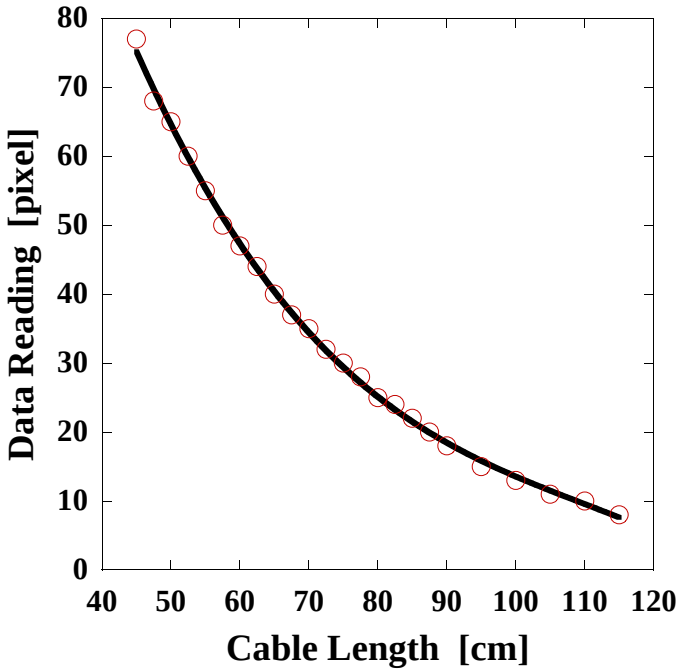

Figure 9.7: 3rd order regression fit for x-axis reading

where, DR is the data reading in pixel and CL is the cable length in centimeter. The curve fits well and captures all the data points ($R^2 = 99.88\%$). The position measurements in the x-axis are then offset by the regression model at the corresponding cable length.

9.2 Trajectory Observation

The test results were analyzed for the effectiveness of each control method. Figure 9.8 shows a crane trajectory using a trapezoidal command. Without any anti-swing control, large amount of oscillations and collisions can be observed throughout the course. The oscillations are the worst when the crane attempts entering the course, picking up the payload, colliding with the rotation pad, and depositing the payload. Also, the crane fails to regain stability after knocking down the rotation pad. These observations indicate that anti-swing control method is necessary for effective crane control.

Figure 9.9 shows the crane trajectory using a SI2M shaper. The SI2M shaper reduces the command-induced oscillations and produces a smoother overall trajectory. However, the crane oscillates significantly when colliding with the rotation pad. The crane cannot

Figure 9.8: Crane trajectory with trapezoidal command

Figure 9.9: Crane trajectory with SI2M shaper

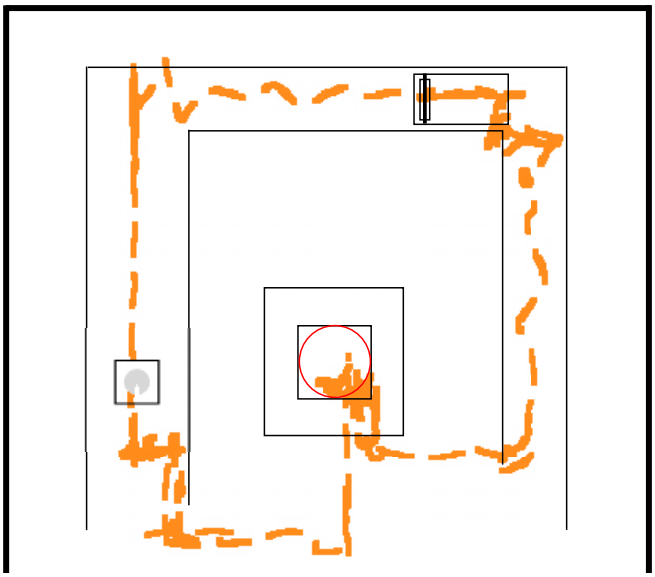

Figure 9.10: Crane trajectory with MRC

reject the external disturbance caused by the pad because the SI2M shaper does not have a feedback loop. This oscillation persists for the remainder of the path and caused difficulty in placing the payload onto the target panel.

Figure 9.10 shows the crane trajectory using a MRC controller. The crane trajectory is smoother compared to that from the trapezoidal command. However, some oscillations still exist before picking up and dropping down the payload. This is because the operators need to adjust the crane position precisely to complete the tasks. Also notice that the crane oscillations are vastly reduced after knocking down the rotation pad. The MRC structure contains a feedback loop that aggressively adapts to cancel the large oscillations caused by the external disturbance.

Figure 9.11 shows the crane trajectory using a SI2M-MRC controller. The trajectory illustrates very little oscillations and no collisions with the sidewalls. The crane remains stable even after hitting the rotation pad. This is because the SI2M shaper limits oscillations from the crane movement and the MRC control reduces oscillations from the external disturbance.

Figure 9.12 shows the crane trajectory using a OIS-MRC controller. The crane trajec-

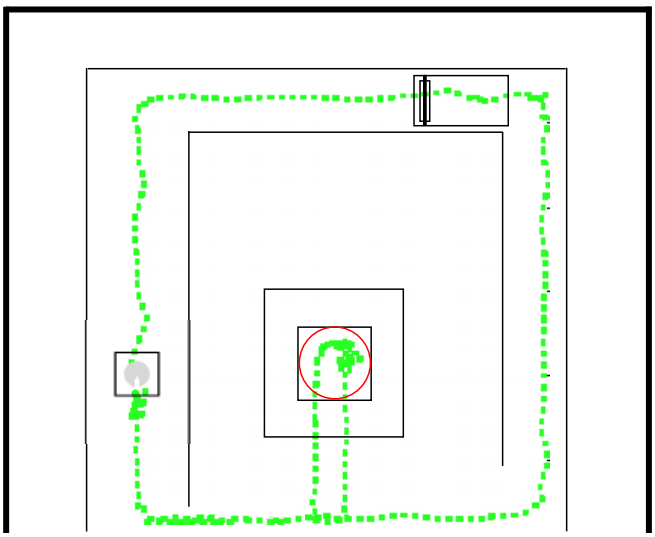

Figure 9.11: Crane trajectory with SI2M-MRC

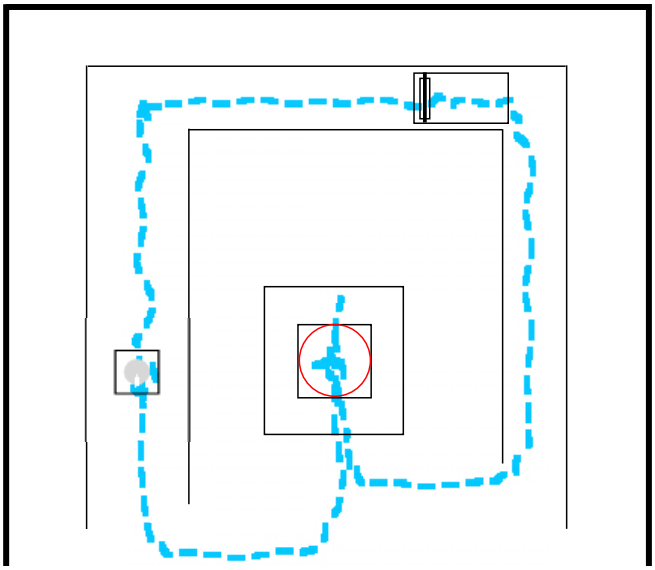

Figure 9.12: Crane trajectory with OIS-MRC

Table 9.1: Average and standard deviation of experiment results

Completion time [sec]	Average	Standard deviation
Trapezoidal	93.90	17.00
SI2M	90.23	15.44
MRC	82.00	13.02
SI2M-MRC	103.57	20.87
OIS-MRC	67.50	14.12
Collision count		
Trapezoidal	7.64	3.76
SI2M	2.45	1.53
MRC	0.57	0.81
SI2M-MRC	0.56	0.70
OIS-MRC	0.35	0.81
Usability rating		
Trapezoidal	1.50	2.13
SI2M	4.86	1.28
MRC	6.67	2.56
SI2M-MRC	4.00	1.81
OIS-MRC	8.85	1.81

tory is as smooth as that of the SI2M-MRC with no occurrence of collisions, indicating that the OIS-MRC design is as robust as the SI2M-MRC design. Furthermore, note that the trajectory follows a tighter and shorter path compared to other controllers. This is realized by the improved ease of navigation via the OIS-MRC controller.

9.3 Operator Testing Results

The results of the human operator testing were analyzed for the completion time, collision count, and usability rating. Table 9.1 summarizes the average and standard deviation of the collected data. One-way ANOVA statistical analysis was used to examine whether there was a significance when different control methods were utilized. Table 9.2 presents the One-way ANOVA results. For each data group, the p-value corresponding to the F-statistic of one-way ANOVA is lower than 0.05. This suggests that the one or more average

Table 9.2: One-way ANOVA results

	F-statistic	p-value
Completion time	13.694	6.606×10^{-9}
Collision count	52.687	1.110×10^{-16}
Usability rating	41.390	1.110×10^{-16}
critical value	$> 2.465 = F(4, 98)$	< 0.05

values in the group are significantly different. The analysis suggests that significant difference exists in the completion time (F-statistic = 13.694 >2.465 and p-value = 6.606×10^{-9} <0.05), collision count (F-statistic = 52.687 2.465 and p-value = 1.110×10^{-16} <0.05), and usability rating (F-statistic = 41.390 >2.465 and p-value = 1.110×10^{-16} <0.05).

Figure 9.13 shows the average values and standard deviations of the course completion time for each control method. Asterisks indicate the significance level ($* :\ p < 0.05,\ \ ** :\ p < 0.01$). The trapezoidal command and SI2M shaper do not have significant difference because they both lack the feature to reject external disturbance, which is a critical factor in completing the course quickly. The trapezoidal command has significantly longer completion time than the MRC and OIS-MRC controllers, because a feedback loop in the MRC structure greatly improves the operating performance by rejecting disturbance and producing smoother crane motion. However, this does not apply to the SI2M-MRC controller. The SI2M-MRC design has significantly longer completion time than other control methods. This is because in the SI2M-MRC design the MRC controller continuously damps out the oscillations caused by each shaper impulse. However, the SI2M shaper (or any input shapers) needs to complete sending all impulses in order to effectively reduce the command-induced oscillations. Because both the MRC control and SI2M shaper attempt to reduce oscillations, the MRC control interferes with the SI2M shaper. This creates an overly-robust controller that causes an extra long time-delay. The OIS-MRC control, on the other hand, has significantly shorter completion time than other control methods. This is because the OIS-MRC is designed specifically to couple with MRC, which avoids this

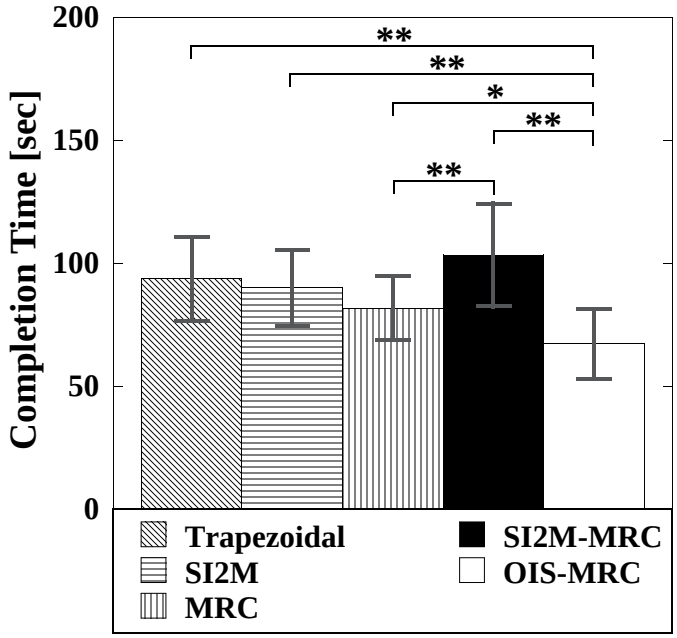

Figure 9.13: Completion time results

Table 9.3: Tukey's HSD test result of completion time

	Trapezoidal	SI2M	MRC	SI2M-MRC
SI2M	1.566	-	-	-
MRC	***4.862***	3.618	-	-
SI2M-MRC	3.185	***4.538***	***4.681***	-
OIS-MRC	***8.436***	***9.991***	***6.150***	***9.272***
$q_{critical}$	> 3.882			

overly-robust issue in the SI2M-MRC.

The Tukey's HSD test was also used to identify which of the pairs of average values were significantly different from each other. The test results are shown in Table 9.3. In this operator testing, the $q_{critical}$ value was calculated to be 3.882. The results greater than the $q_{critical}$ value (highlighted in bold) suggest that there is a significant difference between the two compared groups.

Figure 9.14 shows the average values and standard deviations of the collision count for each control method. Asterisks indicate the significance level. The results from Tukey's HSD test are shown in Table 9.4. The trapezoidal command results in significantly larger

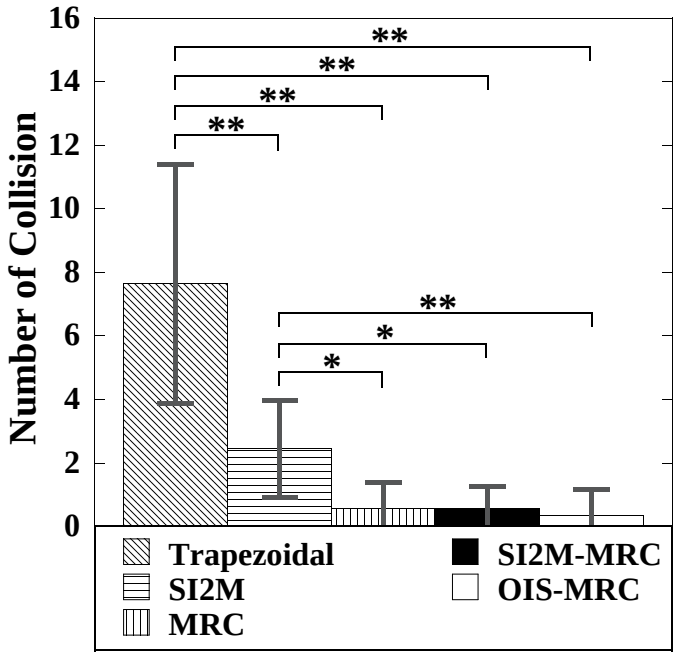

Figure 9.14: Collision count results

Table 9.4: Tukey's HSD test result of collision count

	Trapezoidal	SI2M	MRC	SI2M-MRC
SI2M	***8.692***	-	-	-
MRC	***10.199***	***7.882***	-	-
SI2M-MRC	***10.120***	***7.944***	0.136	-
OIS-MRC	***10.276***	***8.388***	1.773	1.752
$q_{critical}$	> 3.882			

collision counts than other control methods because there is no anti-swing control implemented. Similarly, the SI2M shaper has significantly larger collision counts than the MRC, SI2M-MRC and OIS-MRC designs. This is because the feedback adaptation from the MRC scheme plays a critical role in correcting large oscillation angles and avoiding collisions. The collision counts of the MRC, SI2M-MRC and OIS-MRC controllers do not differ significantly, because the MRC scheme in the controller reduced the collision count to $0 \sim 1$ in each trial.

Figure 9.15 shows the average values and standard deviations of the usability rating for each control method. The results from Tukey's HSD test are shown in Table 9.5. The trape-

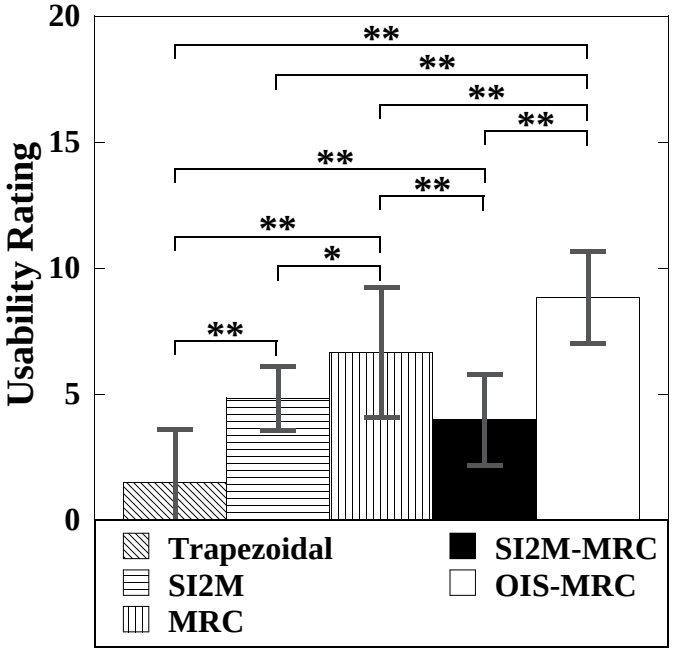

Figure 9.15: Usability rating results

Table 9.5: Tukey's HSD test result of usability rating

	Trapezoidal	SI2M	MRC	SI2M-MRC
SI2M	***8.960***	-	-	-
MRC	***9.581***	***5.352***	-	-
SI2M-MRC	***6.927***	3.531	***6.664***	-
OIS-MRC	***11.335***	***10.190***	***5.752***	***10.348***
$q_{critical}$	> 3.882			

zoidal command has significantly lower usability rating than other control methods because of the lack of control design. The SI2M shaper also has significantly lower usability rating than the MRC and OIS-MRC controllers due to the lack of feedback loop. Although not different significantly, the SI2M-MRC control results in lower usability rating than the SI2M shaper. This confirms the disadvantage of non-optimally combining the SI2M shaper and MRC design, which causes a long rise time due to counter-active interference between these controllers and a delayed actuation response to the user command. The OIS-MRC design has significantly higher usability rating than other control methods. This is because the OIS-MRC design realizes a smooth oscillation-free crane navigation while minimizing

the controller's time duration, which makes the controller responsive to the user command and facilitates the operation for the novice operators.

9.4 Summary

In this chapter, the human operator testing was conducted to validate the superior performance of the proposed OIS-MRC controller design. The test subjects were asked to navigate the crane through the obstacle course as fast as possible without making any collisions. The trapezoidal command, SI2M shaper, MRC, SI2M-MRC, and OIS-MRC designs were tested. The completion time, number of collisions, and rating on ease of use were recorded.

The obstacle course setup was described. The course consisted of tasks that simulate the real-world crane operation; picking up a payload, navigating through a path without collisions, negating external disturbances, and depositing a payload accurately. The programming for the IS-MRC controller and crane drive was implemented using Simotion Scout software. The camera was calibrated using a 3rd order regression fit.

The trajectory from each control method were observed. The trapezoidal command induced large oscillations throughout the trial due to a lack of anti-swing control. The SI2M shaper effectively suppressed command-induced oscillations but suffered large swings from the external disturbance. The MRC control showed small oscillations only at the beginning of sending new commands and when attempting accurate positioning. The SI2M-MRC and OIS-MRC controllers produced oscillation-free trajectories. The OIS-MRC control also traveled shorter distance than the SI2M-MRC because of its easier operation.

The averages and standard deviations of the completion time, collision count, and usability rating were obtained. The operator testing results were analyzed using one-way ANOVA and Tukey's HSD tests for significance. The trapezoidal command had the least usability rating because it had the second longest completion time and significantly larger collision counts than other controllers.

The MRC controller generally benefited the crane operation. This was because the MRC design corrected the crane oscillations in real-time, allowing a fast oscillation cancellation and disturbance rejection. On the contrary, the SI2M shaper suffered disturbance swings from the rotation pad.

The SI2M-MRC design resulted in one of the worst performance. Although the controller effectively prevented the sidewall collisions, it had the longest completion time and the second lowest usability rating. The problem originated in the non-optimized SI2M-MRC combination, which caused an interference in oscillation reduction and a time lag between the crane motion and user input.

The OIS-MRC design had the shortest completion time, the lowest collision count and the highest usability rating. The superior performance of the OIS-MRC design validated its large robustness and quick response to the user command. The results from the human operator testing indicated that the OIS-MRC was successfully designed and vastly improved the overall performance of the crane operation.

CHAPTER 10
CONCLUSIONS AND FUTURE WORK

10.1 Conclusions

In this thesis, a novel control method of combining an input shaping with a model reference control (MRC) scheme was developed. The proposed input-shaped model reference control (IS-MRC) scheme supplemented the weaknesses of both input shaping and MRC control. The MRC provided an increased robustness to modeling errors and external disturbances, while the input shaper smoothed the control signal and prevented an excessive actuator magnification. The various IS-MRC designs were developed and tested on a bridge crane with a single- and double-pendulum payload.

The MRC scheme and control law based on the Lyapunov theory was developed. The nonlinear differential equations of motions of the single- and double-pendulum were presented. The linear state space representations of the systems were obtained. They were utilized as the reference model and estimated plant model that were implemented as parts of the MRC scheme. The second method of Lyapunov was utilized to obtain the closed form of the control signal generated by the MRC control. The issue of increasing control effort was addressed in the crane control simulation. It was found that obtaining close values of the system's natural frequency in the reference model and plant played a crucial role in minimizing the MRC control effort.

The IS-MRC controller for the single-pendulum crane was designed by combining the MRC structure with a Zero-Vibration shaper, called a Zero-Vibration Model Reference Control (ZV-MRC). The ZV-MRC design was tested for the oscillation suppression, state tracking, and control effort reduction performances. The ZV-MRC improved the overall controller performance by linearizing the crane dynamics, which also helped in reducing

the control effort and stabilizing the system. The robustness to the modeling errors between the reference model and plant parameters was analyzed. The ZV-MRC control improved the controller robustness and performed effectively than the MRC only case.

The work was extended to driving an uncertain, nonlinear double-pendulum crane with incomplete state information. Because a real-time measurement of the second payload was very difficult, the MRC control law based only on the states associated with the hook was developed. To model the uncertain crane, the estimated plant model was developed using the median of the possible cable length range. The multi-mode input shapers (Two-Mode Zero-Vibration shaper, Three-Mode Zero-Vibration shaper, and Two-Mode Specified Insensitivity shaper) were designed. The proposed controller designs were referred as ZV2M-MRC, ZV3M-MRC, and SI2M-MRC respectively. The proposed IS-MRC designs were evaluated and compared for the performance improvements. The SI2M-MRC demonstrated the superior performance and robustness to the plant estimation error. The trade-off, however, was a slower motion due to a delayed rise time.

To resolve the time-delay issue and further improve the IS-MRC design, the optimized combination of input shaping and MRC was investigated. The method of designing the optimized IS-MRC (OIS-MRC) control was developed. The reference model parameters and input shaper impulses were obtained via an optimization technique that minimized the rise time and shaper duration. The OIS-MRC controller was also derived to meet the design constraints on the residual oscillation, maximum overshoot, and control effort bounds. The analytical expressions of the constraints were derived and explained. The OIS-MRC design was tested on the uncertain double-pendulum crane with time-varying cable length. The numerical simulations and physical experiments verified that the OIS-MRC achieved the same level of the robustness as the SI2M-MRC, while allowing the controller to operate more aggressively. The disturbance rejection of the IS-MRC designs were also examined via displacement and force disturbances. The proposed designs successfully rejected the external disturbance when the crane was at rest and in motion.

The ergonomics, or usability, of the OIS-MRC design was validated by conducting a human operator testing. The test subjects were asked to navigate the crane through the obstacle course that simulated a real-world crane workspace and multiple practical tasks. The completion time, collision count, and usability rating were measured for various control methods for comparison. The one-way ANOVA and Tukey's HSD tests were used to support the significance of the data. In the testing, the OIS-MRC achieved the smoothest trajectory, the shortest completion time, the lowest collision counts, and the highest usability rating. The test results indicated the superior control performance of the OIS-MRC design due to the large robustness and improved rise time.

10.2 Future Work

The results and insights gained in this thesis build an important foundation in the field of the model-based system control. There are many directions the future investigations can extend. First, the reference model and plant representations utilized in this research can be refined to integrate additional dynamic factors. The dynamic models considered in this thesis mainly focused on the flexible dynamics of the pendulum oscillation. The factors, such as the actuator dynamics and hard nonlinearities in the trolley, could degrade the performance of the IS-MRC controller. They may need to be analyzed more in detail to further increase the utility and reliability of the IS-MRC method.

Also, the IS-MRC control algorithm developed in this thesis can easily be implemented to the other industrial crane applications by replacing the reference model with an adequate representation of the system. For example, the research can extend to study the cranes with more complex dynamics, such as a dual hoist crane and crane with a distributed payload that are known to exhibit complex dynamic behaviors. For these types of dynamic systems, the IS-MRC controller will provide an excellent solution to reduce the system oscillations and limit the complex dynamic behaviors.

The IS-MRC methodology can also be adapted to other mechanical systems with flexi-

ble dynamics, such as robot arms and aerial lifts. The reference model and plant representations need to be revised with the appropriate system models, but the general control theory and derivation process remain the same. This simplicity in the IS-MRC structure awards it a high compatibility with many types of machines and provides unbounded possibilities for future topics.

In addition, the effectiveness of the IS-MRC design using an inappropriate choice of the reference model can be investigated. In this research, the reference model and plant had the same, or at least a similar, system descriptions (i.e. a single- and double-pendulum payload as the reference model and plant respectively). The performance and robustness of the IS-MRC design remains unknown when the reference model representation is fundamentally different from the controlling plant. An example would be using a stable system (i.e. a single-pendulum payload) as the reference model to control an inherently unstable plant (i.e. an inverted-pendulum).

Future work could further refine the optimization process for the OIS-MRC design. The input shaper impulses in this thesis were assumed to have positive amplitudes. However, there are input shaper designs that have negative impulses. They generate more aggressive command profiles and reduce the shaper durations, thus speeding up the system motion. This relaxed constraint on the impulses could influence the OIS-MRC design, and thus be an important extension to the study of the IS-MRC method.

Another way the future work can stem from this thesis is to modify the MRC scheme by using different control laws and adaptation methods. A control method that has characteristics similar to the MRC control is called *Model Reference Adaptive Control* (MRAC). Like the MRC controller, the goal of the MRAC method is to drive the plant response to match the response of the reference model. The major difference is that the MRAC scheme has adapting parameters in its control law and they are updated based on the error between the desired and actual states. This feature of MRAC plays a similar role as the Λ term in the MRC control law, but with more controller design flexibility. It may provide additional

benefits to the control design and thus worth investigating.

REFERENCES

[1] E. Arnold, O. Sawodny, A. Hilderbrandt, and K. Schneider, "Anti-sway system for boom cranes based on an optimal control approach," in *American Control Conference*, vol. 4, Denver, CO, 2003, pp. 3166–71.

[2] E. Abdel-Rahman and A. Nayfeh, "Pendulation reduction in boom cranes using cable length manipulation," *Nonlinear Dynamics*, vol. 27, no. 3, pp. 255–269, 2002.

[3] U. Civil Aviation Authority Safety Regulation Group, *Helicopter external load operations*. The Stationary Office, 2006. CAP 426.

[4] D. Fujioka, A. Rauch, W. Singhose, and T. Jones, "Tip-over stability analysis of mobile boom cranes with double-pendulum payloads," in *2009 American Control Conference*, St. Louis, Missouri, 2009, pp. 3136–3141.

[5] D. Fujioka, "Tip-over stability analysis for mobile boom cranes with single- and double-pendulum payloads," PhD thesis, 2010.

[6] D. D. Fujioka, E. Maleki, and W. Singhose, "Tip-over stability of a cherrypicker," in *Multibody Dynamics 2011 ECCOMAS Thematic Conference*, Brussels, Belgium, 2011, pp. 1–12.

[7] A. Rauch, W. Singhose, D. Fujioka, and T. Jones, "Tip-over stability analysis of mobile boom cranes with swinging payloads," *Journal of Dynamic Systems, Measurements, and Control*, vol. 135, pp. 031 008–1 –031008–6, 2013.

[8] F. Harashima, S. Kondo, K. Ohnishi, M. Kajita, and M. Susono, "Multimicroprocessor-baced control system for quick response induction motor drive," *IEEE Trans. Ind. Applicant.*, vol. IA-21, pp. 602–609, 1985.

[9] R. Souissi and A. J. Koivo, "Modeling and control of a rotary crane for swing-free transport of payloads," in *IEEE Conference on Control Applications*, Dayton, Ohio, 1992, pp. 782–787.

[10] J. H. Yang and K. S. Yang, "Adaptive coupling control for overhead crane systems," *Mechatronics*, vol. 17, no. 2/3, pp. 143–152, 2007.

[11] Y. C. Fang, B. J. Ma, P. C. Wang, and X. B. Zhang, "A motion planning-based adaptive control method for an underactuated crane system," *IEEE Transactions on Control Systems Technology*, vol. 20, no. 1, pp. 241–248, 2012.

[12] I. Mizumoto, T. Chen, S. Ohdaira, M. Kumon, and Z. Iwai, "Adaptive output feedback control of general MIMO systems using multirate sampling and its application to a cart-crane system," *Automatica*, vol. 43, no. 12, pp. 2077–2085, 2007.

[13] H. C. Cho and K. S. Lee, "Adaptive control and stability analysis of nonlinear crane systems with perturbation," *Journal of Mechanical Science and Technology*, vol. 22, no. 6, pp. 1091–1098, 2008.

[14] B. Ma, Y. Fang, and X. Zhang, "Adaptive tracking control for an overhead crane system," in *17th IFAC World Congress*, Seoul, Korea, pp. 12 194–12 199.

[15] W. Wang, J. Yi, D. Zhao, and D. Liu, "Design of a stable sliding-mode controller for a class of second-order underactuated systems," *IEE Control Theory and Applications*, vol. 151, no. 6, pp. 683–690, 2004.

[16] H. Lee, Y. Liang, and D. Segura, "A sliding-mode antiswing trajectory control for overhead cranes with high speed load hoisting," *ASME Journal of Dynamic Systems, Measurement, and Control*, vol. 128, no. 4, pp. 842–845, 2006.

[17] D. Liu, J. Yi, D. Zhao, and W. Wang, "Adaptive sliding mode fuzzy control for a two-dimensional overhead crane," *Mechatronics*, vol. 15, no. 5, pp. 505–522, 2005.

[18] Q. H. Ngo and K. S. Hong, "Adaptive sliding mode control of container cranes," *Control Theory and Applications*, vol. 6, no. 5, pp. 662–668, 2012.

[19] ——, "Sliding-mode antisway control of an offshore container crane," *IEEE/ASME Transactions on Mechatronics*, vol. 17, no. 2, pp. 201–209, 2012.

[20] N. B. Almutari and M. Zribi, "Sliding mode control of a threedimensional overhead crane," *Journal of Vibration and Control*, vol. 15, no. 11, pp. 1679–1730, 2009.

[21] L. A. Tuan, S.-C. Moon, W. G. Lee, and S.-G. Lee, "Adaptive sliding mode control of overhead cranes with varying cable length," *Journal of Mechanical Science and Technology*, vol. 27, no. 3, pp. 885–893, 2013.

[22] G. S. Hu, C. J. Ong, and C. L. Teo, "Minimum-time control of a crane with simultaneous traverse and hoisting motions," *Journal of Optimization Theory and Applications*, vol. 120, no. 2, pp. 395–416, 2004.

[23] Y. Sakawa and Y. Shindo, "Optimal control of container cranes," *Automatica*, vol. 18, no. 3, pp. 257–266, 1982.

[24] A. Z. Al-Garni, K. A. F. Moustafa, and S. S.A.K. J. Nizami, "Optimal control of overhead cranes," *Control Engineering Practice*, vol. 3, no. 9, pp. 1277–1284, 1995.

[25] G. C. Konstantopoulos and A. T. Alexandridis, "Simple energy based controllers with nonlinear coupled-dissipation terms for overhead crane systems," in *Joint 48th IEEE Conference on Decision and Control / 28th Chinese Control Conference*, Shanghai, China, 2009, pp. 3149–3154.

[26] B. Ma, Y. Fang, and Y. Zhang, "Switching-based emergency braking control for an overhead crane system," *IET Control Theory and Applications*, vol. 4, no. 9, pp. 1739–1747, 2010.

[27] T. Burg, D. Dawson, C. Rahn, and W. Rhodes, "Nonlinear control of an overhead crane via the saturation control approach of teel," in *IEEE International Conference on Robotic and Automation*, 1996, pp. 3155–3160.

[28] R. Liu, S. Li, and S. Ding, "Nested saturation control for overhead crane systems," *Transactions of the Institute of Measurement and Control*, vol. 34, no. 7, pp. 862–875, 2012.

[29] M. Moon, H. VanLandingham, and Y. Beliveau, "Fuzzy time optimal control of crane load," in *35th Conf. Decision Control*, 1996, pp. 1127–1132.

[30] C. Chang, "Adaptive fuzzy controller of the overhead cranes with nonlinear disturbance," *IEEE Transactions on Industrial Informatics*, vol. 3, no. 2, pp. 164–172, 2007.

[31] C. Chang and K. Chiang, "Fuzzy projection control law and its application to the overhead crane," *Mechatronics*, vol. 18, no. 10, pp. 607–615, 2008.

[32] C. Chang and T. Chiang, "Overhead cranes fuzzy control design with deadzone compensation," *Neural Computing and Applications*, vol. 18, no. 7, pp. 749–757, 2009.

[33] W. Yu, M. A. Moreno-Armendariz, and F. O. Rodriguez, "Stable adaptive compensation with fuzzy CMAC for an overhead crane," *Information Sciences*, vol. 181, no. 21, pp. 4895–4907, 2011.

[34] G. Corriga, A. Giua, and G. Usai, "An implicit gain-scheduling controller for cranes," *IEEE Transactions on Control Systems Technology*, vol. 6, no. 1, pp. 15–20, 1998.

[35] H. M. Omar and A. H. Nayfeh, "Gantry cranes gain scheduling feedback control with friction compensation," *Journal of Sound and Vibration*, vol. 281, no. 1-2, pp. 1–20, 2005.

[36] Y. Fang, W. E. Dixon, D. M. Dawson, and E. Zergeroglu, "Nonlinear coupling control laws for an underactuated overhead crane system," *IEEE/ASME Transactions on Mechatronics*, vol. 8, no. 3, pp. 418–423, 2003.

[37] M. Park, D. Chwa, and S. Hong, "Antisway tracking control of overhead cranes with system uncertainty and actuator nonlinearity using an adaptive fuzzy sliding-mode control," *IEEE Transactions on Industrial Electronics*, vol. 55, no. 11, pp. 3972–3984, 2008.

[38] H. Lee, Y. Liang, and D. Segura, "A new approach for the antiswing control of overhead cranes with high-speed load hoisting," *International Jounal of Control*, vol. 76, no. 15, pp. 1493–1499, 2003.

[39] J. W. Auernig and H. Troger, "Time optimal control of overhead cranes with hoisting of the load," *Automatica*, vol. 23, no. 4, pp. 437–447, 1987.

[40] K. Terashima, Y. Shen, and K. Yano, "Modeling and optimal control of a rotary crane using the straight transfer transformation method," *Control Engineering Practice*, vol. 15, no. 9, pp. 1179–1192, 2007.

[41] J. Valera, E. Irigoyen, V. Gomez-Garay, and F. Artaza, "Application of neuro-genetic techniques in solving industrial crane kinematic control problem," in *IEEE International Conference on Mechatronics*, Malaga, Spain, 2009.

[42] A. K. Kamath, N. M. Singh, F. Kazi, and R. Pasumarthy, "Dynamics and control of 2d spidercrane: A controlled lagrangian approach," in *IEEE Conference on decision and control*, 2010, pp. 3596–3601.

[43] F. Kazi, R. Banavar, P. Mullhaupt, and D. Bonvin, "Stabilization of a 2d-spidercrane mechanism using damping assignment passivity- based control," in *17th IFAC World Congress*, Seul, Korea, 2008, pp. 3155–3160.

[44] I. Sarras, F. Kazi, R. Ortega, and R. Banavar, "Total energy-shaping IDA-PBC control of the 2d-spidercrane," in *IEEE Conference on decision and control*, 2010, pp. 1122–1127.

[45] G. Bartolini, A. Pisano, and E. Usai, "Second-order sliding-mode control of container cranes," *Automatica*, vol. 38, no. 10, pp. 1783–1790, 2002.

[46] J. A. Acosta, R. Ortega, A. Astolfi, and A. M. Mahindrakar, "Interconnection and damping assignment passivity-based control of mechanical systems with underactuation degree one," *IEEE Trans. Autom. Control*, vol. 50, no. 12, 2005.

[47] S. Ning, F. Yoongchun, and X. Zhang, "Energy coupling output feedback control of 4-dof underactuated cranes with saturated inputs," *Automatica*, vol. 49, no. 5, pp. 1318–1325, 2013.

[48] R. Mehra, S. Satpute, F. Kazi, and N. Singh, "Energyshaping based tracking control of 4-dof underactuated cranes with practical constraints," *Transactions on Control Systems Technology*, 2015.

[49] D. Chwa, "Nonlinear tracking control of 3-d overhead cranes against the initial swing angle and the variation of payload weight," *IEEE Transactions on Control Systems Technology*, vol. 17, no. 4, pp. 876–883, 2009.

[50] N. Sun, Y. Fang, Y. Zhang, and B. Ma, "A novel kinematic coupling-based trajectory planning method for overhead cranes," *IEEE/ASME Transactions on Mechatronics*, vol. 17, no. 1, pp. 166–173, 2012.

[51] C. Makkar, G. Hu, W. Sawyer, and W. Dixon, "Lyapunov-based tracking control in the presence of uncertain nonlinear parameterizable friction," *IEEE Transactions on Automatic Control*, vol. 52, no. 10, pp. 1988–1994, 2007.

[52] M. M. Seron, G. C. Goodwin, and S. F. Graebe, "Control system design issues for unstable linear systems with saturated inputs," *IEE Proc. Control Theory Applications*, vol. 142, no. 4, 1995.

[53] F. Amato, R. Iervolino, M. Pandit, S. Scala, and L. Verde, "Analysis of pilot-in-the-loop oscillations due to position and rate saturations," in *Conference on Decision and Control*, Sydney, Australia, 2000, pp. 3564–3569.

[54] J. Danielson, J. Lawrence, and W. Singhose, "Command shaping for flexible systems subject to constant acceleration limits," *Journal of Dynamic Systems Measurement and Control*, vol. 130, no. 5, 2008.

[55] M. Tian and G. Tao, "Adaptive output dead-zone compensation," in *IEEE Conference on Decision and Control*, San Diego, CA, 1997, pp. 1157–1161.

[56] G. Tao and P. V. Kokotovic, "Continuous-time adaptive control of systems with unknown backlash," *IEEE Transactions on Automatic Control*, vol. 40, no. 6, 1995.

[57] J. Lawrence, M. Falkenberg, and W. Singhose, "Input shaping for a flexible nonlinear, one-link robotic arm with backlash," in *Japan-USA Symposium on Flexible Automation*, Denver, CO, 2004.

[58] J. Lawrence, W. Singhose, and K. Hekman, "Friction-compensating command shaping for vibration reduction," *Journal of Vibration and Acoustics*, vol. 127, pp. 307–314, 2005.

[59] H. Kawai, Y. B. Kim, and Y. W. Choi, "Anti-sway system with image sensor for container cranes," *Journal of Mechanical Science and Technology*, vol. 23, no. 10, pp. 2757–2765, 2009.

[60] Y. Y. Tabata and H., "Visual feedback control of an overhead crane and its combination with time-optimal control," in *IEEE/ASME International Conference on Advanced Intelligent Mechatronics*, 2008, pp. 1114–1119.

[61] M. Bisgaard, A. la Cour-Harbo, and J. Dimon Bendtsen, "Adaptive control system for autonomous helicopter slung load operations," *Control Engineering Practice*, vol. 18, no. 7, pp. 800–811, 2010.

[62] J. A. Ottander and E. N. Johnson, "Precision slung cargo delivery onto a moving platform," in *AIAA Modeling and Simulation Technologies Conference*, Toronto, Canada, AIAA Paper 2010-8090.

[63] O. Sawodny, H. Aschemann, J. Kumpel, C. Tarin, and K. Schneider, "Anti-sway control for boom cranes," in *American Control Conference*, Anchorage, AK, 2002.

[64] O. Sawodny, H. Aschemann, and S. Lahres, "An automated gantry crane as a large workspace robot," *Control Engineering Practice*, vol. 10, no. 12, pp. 1323–1338, 2002.

[65] J. M. Veciana, S. Cardona, and P. Català, "Modified adaptive input shaping for maneuvering cranes using a feedback MEM gyroscope with null drift," *INTERNATIONAL JOURNAL OF PRECISION ENGINEERING AND MANUFACTURING*, vol. 16, no. 9, pp. 1911 –1917, 2015.

[66] J. Neupert, E. Arnold, K. Schneider, and O. Sawodny, "Tracking and anti-sway control for boom cranes," *Control Engineering Practice*, vol. 18, no. 1, pp. 31–44, 2010.

[67] M. S. Weinberg and A. Kourepenis, "Error sources in in-plane silicon tuning-fork MEMS gyroscopes," *Journal of Microelectromechanical Systems*, vol. 15, no. 3, p. 479 491, 2006.

[68] I. P. Prikhodko, A. A. Trusov, and A. M. Shkel, "Compensation of drifts in high-q MEMS gyroscopes using temperature self-testing," *Sensors and Actuators A: Physical*, vol. 201, pp. 517 –524, 2013.

[69] J.-P. Richard, "Time-delay systems: An overview of some recent advances and open problems," *Automatica*, vol. 39, no. 10, pp. 1667–1694, 2003.

[70] H. M. Omar and A. H. Nayfeh, "A simple adaptive feedback controller for tower cranes," in *ASME Design Engineering Technical Conferences*, Pittsburgh, Pennsylvania, 2001.

[71] C. J. Chien and L. C. Fu, "A new approach to model reference control for a class of arbitrarily fast time-varying unknown plants," *Automatica*, vol. 28, no. 2, pp. 437–440, 1992.

[72] P. Y. Huang and B. S. Chen, "Robust model-reference control of linear MIMO time-varying systems," *Control-Theory and Advanced Technology*, vol. 9, no. 2, pp. 405–439, 1993.

[73] A. Abdullah and M. Zribi, "Model reference control of LPV systems," *Journal of the Franklin Institute - Engineering and Applied Mathematics*, vol. 346, no. 9, pp. 854–871, 2009.

[74] H. Nijmeijer and S. M. Savaresi, "On approximate model-reference control of SISO discrete-time nonlinear systems," *Automatica*, vol. 34, no. 10, pp. 1261–1266, 1998.

[75] J. Y. Kim, V. Natarajan, S. D. Kelly, and J. Bentsman, "Partial difference equation based model reference control of a multiagent network of underactuated aquatic vehicles with strongly nonlinear dynamics," *Nonlinear Analysis: Hybrid Systems*, vol. 4, no. 3, pp. 513–523, 2010.

[76] I. D. Landau, *Adaptive control: The model reference approach*. New York: Marcel Dekker, 1979.

[77] A. Ekrekli and D. J. Brookfield, "The practical implementation of model reference robot control," *Mechatronics*, vol. 7, pp. 549–564, 1997.

[78] N. Hovakimyan, R. Rysdyk, and A. J. Calise, "Dynamic neural networks for output feedback control," in *38th IEEE Conference on Decision and Control*, vol. 2, 1999, pp. 1685–1690.

[79] A. Ucar, "Model-reference control of chaotic systems," *Chaos, Solitons and Fractals*, vol. 31, pp. 712–717, 2007.

[80] P. Zhao, C. Liu, and X. Feng, "Model reference control of hyperchaotic systems," *Journal of Applied Mathematics*, vol. 2012, 2012.

[81] H. Hongjie and M. Yuqiao, "A lyapunov-based model reference control scheme with CMAC neural network," in *Sixth International Symposium on Instrumentation and Control Technology: Sensors, Automatic Measurement, Control, and Computer Simulation*, vol. 6358, Beijing, China, 2006.

[82] A. M. H. Basher and R. Mukundan, "Model-reference control of uncertain systems with time delays in plant state and control," *International Journal of Systems Science*, vol. 18, no. 9, pp. 1609–1626, 1987.

[83] H. A. Basher, "Model reference control of uncertain time-delay systems," in *IEEE SoutheastCon*, Concord, NC, 2010, pp. 467–470.

[84] S. Santosh and M. Chidambaram, "Model reference control of unstable second-order systems with time delay," *Indian Chemical Engineer*, vol. 55, no. 2, pp. 104–111, 2013.

[85] J. Belikov and E. Petlenkov, "Model reference control of nonlinear TITO systems by dynamic output feedback linearization of neural network based ANARX models," in *IEEE International Conference on Control Applications and International Symposium on Intelligent Control*, Saint Petersburg, Russia, 2009, pp. 1820–1825.

[86] ——, "Model reference control of nonlinear MIMO systems by dynamic output feedback linearization of ANARX models," in *IEEE International Conference on Control and Automation*, Christchurch, New Zealand, 2009, pp. 536–541.

[87] S. Sastry and A. Isidori, "Adaptive control of linearizable systems," *IEEE Transactions on Automatic Control*, vol. AC-34, pp. 1123–1131, 1989.

[88] F. C. Chen and C. C. Liu, "Adaptively controlling nonlinear continuous-time systems using neural networks," *IEEE Transactions on Automatic Control*, vol. AC-39, pp. 1306–1310, 1994.

[89] J. Krause and G. Stein, "Structual limitations of model reference adaptive controllers," in *Ameican Control Conference*, Minneapolis, Minnesota, 1987, pp. 230–237.

[90] G. Duan, W. Liu, and G. Liu, "Robust model reference control for multivariable linear systems: A parametric approach," *Journal of Systems and Control Engineering of IMech*, pp. 599–610, 2001.

[91] J. Sun, A. Olbrot, and M. P. Polis, "Robust stabilization and robust performance using model-reference control and modeling error compensation," *IEEE Transactions on Automatic Control*, vol. 39, no. 3, pp. 630–635, 1994.

[92] C. Pedret, R. Vilanova, R. Moreno, and I. Serra, "A new architecture for robust model reference control," in *44th IEEE Conference on Decision Control*, Seville, Spain, 2005, pp. 7876–7881.

[93] J. He and Z. Zhang, "Model reference control based on SVM," in *International Symposium on Neural Networks*, vol. 3174, Dalian, China, 2004, pp. 138–143.

[94] N. C. Singer and W. P. Seering, "Preshaping command inputs to reduce system vibration," *Journal of Dynamic Systems, Measurement and Control*, vol. 112, no. 1, pp. 76–82, 1990.

[95] O. J. M. Smith, "Posicast control of damped oscillatory systems," *Institute of Radio Engineers*, vol. 45, no. 9, pp. 1249–1255, 1957.

[96] ——, *Feedback control systems*. New York: McGraw-Hill Book Co., Inc., 1958, pp. 331–345.

[97] W. Singhose, S. Derezinski, and N. Singer, "Extra-insensitive input shapers for controlling flexible spacecraft," *AIAA Journal of Guidance, Control, and Dynamics*, vol. 19, no. 2, pp. 385–391, 1996.

[98] J. Vaughan, A. Yano, and W. Singhose, "Comparison of robust input shapers," *Journal of Sound and Vibration*, vol. 315, no. 4-5, pp. 797–815, 2008.

[99] M.-C. Pai, "Robust input shaping control for multi-mode flexible structures," *International Journal of Control, Automation, and Systems*, vol. 9, no. 1, pp. 23–31, 2011.

[100] ——, "Robust input shaping control for multi-mode flexible structures using neuro-sliding mode output feedback control," *Journal of the Franklin Institute*, vol. 349, 1283–1303, 2012.

[101] J. Y. Park and P. H Chang, "Vibration control of a telescopic handler using time delay control and commandless input shaping technique," *Control Engineering Practice*, vol. 12, no. 6, pp. 769–780, 2004.

[102] E. Pereira, J. R. Trapero, I. M. Diaz, and V. Feliu, "Adaptive input shaping for single-link flexible manipulators using an algebraic identification," *Control Engineering Practice*, vol. 20, no. 2, pp. 138–147, 2012.

[103] A. Khalid, J. Huey, W. Singhose, J. Lawrence, and D. Frakes, "Human operator performance testing using an input-shaped bridge crane," *Journal of Dynamic Systems, Measurement and Control*, vol. 128, no. 4, pp. 835–841, 2006.

[104] K. L. Sorensen, W. Singhose, and S. Dickerson, "A controller enabling precise positioning and sway reduction in bridge and gantry cranes," *Control Engineering Practice*, vol. 15, no. 7, pp. 825–837, 2007.

[105] W. Singhose, D. Kim, and M. Kenison, "Input shaping control of double-pendulum bridge crane oscillations," *Journal of Dynamic Systems, Measurement, and Control*, vol. 130, 2008.

[106] D. Kim and W. Singhose, "Performance studies of human operators driving double-pendulum bridge cranes," *Control Engineering Practice*, vol. 18, no. 6, pp. 567–576, 2010.

[107] Q. H. Ngo and K. S. Hong, "Skew control of a quay container crane," *Journal of Mechanical Science and Technology*, vol. 23, no. 12, pp. 3332–3339, 2009.

[108] W. Singhose and D. Kim, "Manipulation with tower cranes exhibiting double-pendulum oscillations," in *IEEE Int. Conf. on Robotics and Automation*, Rome, Italy, 2007.

[109] D. Blackburn, W. Singhose, J. Kitchen, V. Patrangenaru, J. Lawrence, T. Kamoi, and A. Taura, "Advanced input shaping algorithm for nonlinear tower crane dynamics," in *8th International Conference on Motion and Vibration Control*, Daejeon, Korea, 2006.

[110] ——, "Command shaping for nonlinear crane dynamics," *Journal of Vibration and Control*, vol. 16, no. 4, pp. 1–25, 2010.

[111] D. Lewis, G. G. Parker, B. Driessen, and R. Robinett, "Command shaping control of an operator-in-the-loop boom crane," in *American Control Conference*, vol. 5, Philadelphia, Pennsylvania, 1998, pp. 2643–7.

[112] G. Parker, K. Groom, J. Hurtado, J. Feddema, R. Robinett, and F. Leban, "Experimental verification of a command shaping boom crane control system," in *American Control Conference*, San Diego, CA, 1999, pp. 86–90.

[113] V. Drapeau and D. Wang, "Verification of a closed-loop shaped input controller for a five-bar-linkage manipulator," in *IEEE Conference on Robotics and Automation*, Atlanta, Georgia, 1993, pp. 216–221.

[114] D. P. Magee, D. W. Cannon, and W. J. Book, "Combined command shaping and inertial damping for flexure control," in *American Control Conference*, Albuquerque, NM, 1997, pp. 1330–1334.

[115] R. Orszulik and J. Shan, "Vibration control using input shaping and adaptive positive position feedback," *AIAA Journal of Guidance, Control, and Dynamics*, vol. 34, no. 4, pp. 1031–1044, 2011.

[116] M. Romano, B. Agrawal, and Bernelli-Zazzera, "Experiments on command shaping control of a manipulator with flexible links," *AIAA Journal of Guidance, Control, and Dynamics*, vol. 25, no. 2, pp. 232–239, 2002.

[117] A. K. Banerjee and W. E. Singhose, "Command shaping in tracking control of a two-link flexible robot," *Journal of Guidance, Control, and Dynamics*, vol. 21, no. 6, pp. 1012–1015, 1998.

[118] S. J. Farshad Khorrami and A. Tzes, "Experiments on rigid body-based controllers with input preshaping for a two-link flexible manipulator," *Transactions on Robotics and Automation*, vol. 10, pp. 55–65, 1994.

[119] H. Utsuno, K. Isomura, H. Matsuhisa, and K. Yamada, "Acceleration and deceleration pattern to suppress residual vibration of the robot arm," in *17th International Congress on Sound and Vibration*, Cairo, Egypt, 2010.

[120] T. Singh and S. Vadali, "Input-shaped control of three-dimensional maneuvers of flexible spacecraft," *AIAA Journal of Guidance, Control, and Dynamics*, vol. 16, no. 6, pp. 1061–1068, 1993.

[121] B. Wie, R. Sinha, and Q. Liu, "Robust time-optimal control of uncertain structural dynamic systems," *AIAA Journal of Guidance, Control, and Dynamics*, vol. 15, no. 5, pp. 980–983, 1993.

[122] T. Singh and S. Vadali, "Robust time-optimal control: A frequency domain approach," *AIAA Journal of Guidance, Control, and Dynamics*, vol. 17, no. 2, pp. 346–353, 1994.

[123] W. Singhose, K. Bohlke, and W. Seering, "Fuel-efficient pulse command profiles for flexible spacecraft," *AIAA Journal of Guidance, Control, and Dynamics*, vol. 19, no. 4, pp. 954–960, 1996.

[124] T. D. Tuttle and W. P. Seering, "Experimental verification of vibration reduction in flexible spacecraft using input shaping," *Journal of Guidance Control and Dynamics*, vol. 20, no. 4, pp. 658–664, 1997.

[125] Q. L. Hu, "Simultaneous vibration reduction and attitude control of flexible spacecraft with on-off actuators," *Intelligent Automation and Soft Computing*, vol. 17, no. 3, pp. 343–354, 2011.

[126] D. Gorinevsky and G. Vukovich, "Nonlinear input shaping control of flexible spacecraft reorientation maneuver," *AIAA Journal of Guidance, Control, and Dynamics*, vol. 21, no. 2, pp. 264–270, 1998.

[127] J. Potter, W. Singhose, and M. Costello, "Reducing swing of model helicopter sling load using input shaping," in *9th IEEE International Conference on Control and Automation*, Santiago, Chile, 2011, pp. 348–353.

[128] C. Adams, J. Potter, and W. Singhose, "Modeling and input shaping control of a micro coaxial radio-controlled helicopter carrying a suspended load," in *12th International Conference on Control, Automation, and Systems*, Jeju, South Korea, 2012, pp. 645–650.

[129] J. Fortgang, W. Singhose, J. Marquez, and J. Perez, "Command shaping for micro-mills and CNC controllers," in *American Control Conference*, Portland, OR, 2006, pp. 4531–4536.

[130] W. Singhose, W. Seering, and N. Singer, "Time-optimal negative input shapers," *Journal of Dynamic Systems Measurement and Control*, vol. 119, no. 6, pp. 198–205, 1997.

[131] B. Rappole, N. Singer, and W. Seering, "Multiple-mode impulse shaping sequences for reducing residual vibrations," in *23rd Biennial Mechanisms Conference*, vol. DE-71, Minneapolis, MN, 1994, pp. 11–16.

[132] C. F. Cutforth and L. Y. Pao, "Control using equal length shaped commands to reduce vibration," *IEEE Transactions on Control Systems Technology*, vol. 11, no. 1, 2003.

[133] M. F. Daqaq, C. K. Reddy, and A. H. Nayfeh, "Input-shaping control of nonlinear MEMS," *Nonlinear Dynamics*, vol. 54, no. 1-2, pp. 167–179, 2008.

[134] W. Singhose, N. Singer, and W. Seering, "Improving repeatability of coordinate measuring machines with shaped command signals," *Precision Engineering*, vol. 18, pp. 138–146, 1996.

[135] S. Jones and A. G. Ulsoy, "An approach to control input shaping with application to coordinate measuring machines," *ASME Journal of Dynamic Systems, Measurement, and Control*, vol. 121, no. 2, pp. 242–247, 1999.

[136] J. Potter and W. Singhose, "Effects of input shaping on manual tracking with flexible and time-delayed system dynamics," in *10th IFAC Workshop on Time Delay Systems*, vol. 10, Boston, Massachusetts, 2012, pp. 79–84.

[137] ——, "Effects of input shaping on manual control of flexible and time-delayed systems," *The Journal of the Human Factors and Ergonomics Society*, vol. 56, no. 7, pp. 1284–95, 2014.

[138] J. Huey and W. Singhose, "Design of proportional-derivative feedback and input shaping for control of inertia plants," *IET Control Theory and Applications*, vol. 6, no. 3, pp. 357–364, 2012.

[139] M. Muenchhof and T. Singh, "Concurrent feed-forward/feed-back design for flexible structures," in *AIAA Guidance, Navigation and Control Conference*, Monterey, California, 2002.

[140] P. Chang and J. Park, "Use of input shaping technique with a robust feedback control and its application to the position control of surface mount machine," in *IEEE*

International Conference on Control Applications, Dearborn, MI, 1996, pp. 397–402.

[141] ——, "A concurrent design of input shaping technique and a robust control for high-speed/high-precision control of a chip mounter," *Control Engineering Practice*, vol. 9, pp. 1279–1285, 2001.

[142] I. M. Daz, E. Pereira, V. Feliu, and J. J. L. Cela, "Concurrent design of multimode input shapers and link dynamics for flexible manipulators," *IEEE/ASME Transactions on Mechatronics*, vol. 15, no. 4, pp. 646–651, 2010.

[143] M. Kenison and W. Singhose, "Concurrent design of input shaping and proportional plus derivative feedback control," *Journal of Dynamic Systems, Measurement and Control*, vol. 124, pp. 398–405, 2002.

[144] R. K. Gopalakrishnan J. and T. Singh, "Concurrent feedback/feedforward design for second order systems," in *AIAA Guidance, Navigation and Control Conference*, San Francisco, California, 2005.

[145] P. N. Banerjee A. and M. Gonzalez, "Simultaneous optimization of input shaping and feedback control for slewing flexible spacecraft," in *American Control Conference*, Denver, CO, 2003, pp. 4796–4798.

[146] L. Yu and T. N. Chang, "Model reference zero vibration balance control of dual solenoid position actuator," in *2008 International Symposium on Flexible Automation*, Atlanta, GA, 2008.

[147] ——, "Zero vibration on-off position control of dual solenoid actuator," *IEEE Transactions on Industrial Electronics*, vol. 57, no. 7, pp. 2519–2526, 2010.

[148] X.-Z. G. Q. Hu and G. Ma, "Reference model variable structure output feedback for attitude maneuvers control of flexible spacecrafts," *Intelligent Automation and Soft Computing*, vol. 15, no. 1, pp. 53–62, 2009.

[149] D. Yuan and T. Chang, "Trajectory control of robot with model reference zero vibration shaper," in *3rd International Conference on Mechatronics*, Budapest, Hungary, 2006, pp. 636–641.

[150] D. Yuan and T. N. Chang, "Model reference input shaper design with applications to a high-speed robotic workcell with variable loads," *IEEE Transactions on Industrial Electronics*, vol. 55, no. 2, pp. 842–851, 2008.

[151] T. Chang, D. Yuan, and H. Hanek, "Matched feedforward/model reference control of a high precision robot with dead-zone," *IEEE Transactions on Control Systems Technology*, vol. 16, pp. 94–102, 2007.

[152] W. Chatlatanagulchai and P. Kaveesoontornsanoh, "Improving robustness of input shaping technique with model reference iterative learning control," in *The 28th Conference of Mechanical Engineering Network of Thailand (MENETT 28)*, Khonkaen, Thailand, 2014, pp. 1–8.

[153] P.-N. Chatlatanagulchai W. and P. Poedaeng, "Model reference input shaping using quantitative feedback control," in *The 5th TSME International Conference on Mechanical Engineering*, Chiang Mai, Thailand, 2014, pp. 1–9.

[154] L. Yu and T. N. Chang, "Model reference zero vibration control of ultrahigh precision piezoelectric nanopositioner," in *American Control Conference*, Baltimore, MD, 2010, pp. 5856–5861.

[155] L. Yu and T. N. Chang, "Variable model reference high precision position control of dual solenoid actuator," in *34th Annual Conference of IEEE Industrial Electronics*, Orlando, FL, 2008, pp. 2609–2614.

[156] F. L. Mingxiao Dong Bo Pang and H. Liu, "Analysis on payload oscillation, actuator effort and energy usage of PD combined with input-shaping for bridge cranes," *Journal of Basic Science and Engineering*, vol. 18, no. 5, pp. 832–837, 2010.

[157] M. Dong, B. Pang, F. Li, and H. Liu, "Effect of input shaping on actuator effort of inertial plants," in *4th International Conference on Engineering Technologies and Ceeusro*, vol. 464, Zhenjiang, China, 2011, pp. 138–141.

[158] D. Fujioka and W. Singhose, "Control effort reduction analysis of zero-vibration model reference control for controlling a time-varying plant," in *American Control Conference*, Portland, OR, 2014, pp. 3110–3115.

[159] D. Fujioka, M. Shah, and W. Singhose, "Robustness analysis of input-shaped model reference control on a double-pendulum crane," in *American Control Conference*, Chicago, IL, 2015, pp. 2561–2566.

[160] D. Fujioka and W. Singhose, "Input-shaped model reference control of a nonlinear time-varying double-pendulum crane," in *10th Asian Control Conference*, Kota Kinabalu, Sabah, Malaysia, 2015, pp. 1–6.

[161] ——, "Performance comparison of input-shaped model reference control on an uncertain flexible system," in *International Federation of Automatic Control - Workshop on Time Delay Systems*, Ann Arbor, MI, 2015, pp. 129 –134.

[162] W. Chatlatanagulchai and P. H. Meckl, "Model-independent control of a flexible-joint robot manipulator," *Journal of Dynamic Systems, Measurement, and Control*, vol. 131, no. 4, pp. 1–10, 2009.

[163] K. Rintanen, "Modeling, instrumentation and control of a trolley crane," Control Engineering Laboratory at Helsinki University of Technology, Espoo, Finland, Tech. Rep., 1991.

[164] A. Karajgikar, J. Vaughan, and W. Singhose, "Double-pendulum crane operator performance comparing pd-feedback control and input shaping," in *Advances in Computational Multibody Dynamics - ECCOMAS Thematic Conference*, Brussels, Belgium, 2011, pp. 1–14.

[165] G. I. Bara, J. Daafouz, F. Kratz, and J. Ragot, "Parameter-dependent state observer design for affine LPV systems," *International Journal of Control*, vol. 16, pp. 1601–1611, 2001.

[166] M. Ehsani, "Adaptive control of servo motor by MRAC method," in *IEEE International Conference on Vehicle, Power and Propulsion*, Arlington, TX, 2007, pp. 78–83.

[167] K. J. Pankaj S. and N. R. K., "Application of model reference adaptive control scheme to second order system using MIT rule," in *International Conference on Electrical Power and Energy Systems*, Bhopal, India, 2010.

[168] ——, "Effect of adaptation gain on system performance for model reference adaptive control scheme using MIT rule," in *International Conference of World Academy of Science, Engineering and Technology*, Paris, France, 2010.

[169] ——, "Effect of adaptation gain in model reference adaptive controlled second order system," *International Journal of ETASR - Engineering, Technology Applied Science Research*, vol. 1, no. 3, 2011.

[170] W. J. Chen Y.R. and N. Cheung, "Lyapunov's stability theory-based model reference adaptive control for permanent magnet linear motor drives," in *IEEE International Conference on Power Electronics System and Applications*, pp. 260–266.

[171] C. Shyu Yang and Lin, "Model reference adaptive control design for a shunt active-power-filter system," *IEEE Transactions on Industrial Electronics*, vol. 55, no. 1, 2008.

[172] K. J.C. R. Stefanello M. and H. Grundling, "Design of a robust model reference adaptive control for a shunt active power filter," in *IEEE International Conference on Industrial Electronics*, Orlando, FL, 2008, pp. 158–163.

[173] K. J. Pankaj S. and N. R. K., "Comparative analysis of MIT rule and lyapunov rule in model reference adaptive control scheme," *Innovative Systems Design and Engineering*, vol. 2, no. 4, pp. 154–163, 2011.

[174] D. Fujioka and W. Singhose, "Input-shaped model reference control on a single-pendulum payload," *Control Engineering Practice*, Submitted.

[175] S. W. Kozak K. and I. Ebert-Uphoff, "Performance measures for input shaping and command generation," *Journal of Dynamic Systems, Measurement, and Control*, vol. 128, pp. 731–736, 2006.

[176] D. Fujioka and W. Singhose, "Input-shaped model reference control of double-pendulum systems," *IEEE Transactions on Control Systems Technology*, Submitted.

[177] W. Singhose, E. Crain, and W. Seering, "Convolved and simultaneous two-mode input shapers," *IEE Control Theory and Applications*, vol. 144, no. 6, pp. 515–520, 1997.

[178] J. M. Hyde and W. P. Seering, "Using input command pre-shaping to suppress multiple mode vibration," in *IEEE International Conference on Robotics and Automation*, vol. 3, Sacramento, CA, 1991, pp. 2604–2609.

[179] R. Blevins, *Formulas for natural frequency and mode shape*. New York, NY: Van Nostrand Reinhold Co., 1979.

[180] D. Fujioka and W. Singhose, "Development and analysis of optimized input-shaped model reference control," *Journal of Dynamic Systems, Measurement, and Control*, Submitted.

[181] B. C. Kuo, *Automatic control systems*, 7th ed. Prentice Hall, 1995, Section 7-5.

[182] D. Fujioka, Y. Yang, and W. Singhose, "Human operator performance testing on input-shaped model reference control," *IEEE Transactions on Human-Machine Systems*, Submitted.

VITA

Daichi D. Fujioka was born in Huston, Texas. He received his B.S. and M.S. degrees in Mechanical Engineering from Georgia Institute of Technology in 2007 and 2010, respectively. He earned his Ph.D. degree in the school of Mechanical Engineering at Georgia Institute of Technology. His research interest focuses on the vibration reduction and safe operation of flexible machines. He investigates the concurrent design of input shaping and model reference control method. He feels enthusiastic about teaching STEM education and is strongly motivated to pursue a career in academia.